Nagaoka University of Technology

長岡技術科学大学

Dissertation

博士論文

On the Behavior of Siliceous Minerals under Irradiation and Plant Life Management of Concrete Structure in Nuclear Facilities

(照射による鉱物の変化と原子力用コンクリート構築物の経年劣化管理の研究)

A dissertation submitted in partial fulfillment of the requirements for the degree of

Doctor of Engineering

in

Energy and Environment Science

-by-

LUU VU NHUT

(Student number: 16505183)

Academic advisor: Assoc. Professor **Murakami Kenta**

Nuclear Materials & Maintenance Research Laboratory

March 2021

ABSTRACT

Plant Life Management (PLM) is important to ensure the safe of long-term operation (LTO) of Light Water Reactors (LWRs), in which non-replaceable components, such as Concrete Biological Shield (CBS), must maintain their integrity during normal operation and transient conditions, e.g., locally exposure to high temperature and irradiation flux. Recent studies indicated that two processes could affect the integrity of CBS: (1) radiation-induced volume expansion (RIVE) in concrete's aggregates due to the amorphization transition, and (2) the radiation-induced drying in cement paste due to radiation heating and/or exposure to elevated temperature from hot RPV (~300^{o}C). Current attentions are related to the estimation of a reference level for concrete considering possible aging phenomena and establishing the inspection program for the existing concrete structure. Nevertheless, it is difficult to define the appropriate reference level due to several issues: unknown mechanism of RIVE, diversity of concrete aggregates, and diversity of neutron spectrum and energy cut-off. The purpose of this study is to clarify environmental degradation effects and resultant changes in properties of concrete and its components considering the long-term operation (i.e., up to 60- or 80-year operation).

Ion irradiation was used to extract the RIVE mechanism on three common siliceous minerals in rock-forming aggregates including quartz, albite, and microcline. The main findings are (1) though both ionization and collision was found to contribute to RIVE, ionization is insignificant under neutron irradiation, and RIVE is mainly indicated by knock-on displacements (i.e., displacement per atom, dpa); this suggests the use of the amount of knock-on displacements as an index of irradiation effects on concrete structures during long-term operation; (2) since the RIVE is currently correlated with the amorphization and RIVE is presumed to reach the saturation at amorphization, the present study showed the RIVE can continue even

after the amorphization; (3) correlating the change of RIVE and mechanical properties under irradiation in three minerals showed that fluence dependence of RIVE was similar, but the mechanism of RIVE in the minerals differed, which is found to be related to mineral structure and alkali ion content; and (4) irradiation temperature was found to enhance the structural relaxation of amorphized silica with an activation energy around 0.13eV, this is found to be related to the enhanced mobility of defects.

Based on the above results, the current literature data on neutron-irradiated concrete was re-evaluated to determine a threshold value considering the RIVE effect. The current value was initially regarding neutron fluence which remains high uncertainty due to the diversity of neutron spectrum, thus a correlation parameter was proposed, which can be used to normalize neutron fluence into the dpa. The RIVE is found to occur beyond 0.04dpa, but concrete decreases the strength at 0.02dpa. This could be related to radiation-induced drying effect.

The possibility of ultrasonic-based method has been examined on real concrete samples, which have been subjected to elevated temperatures to simulating the drying effects. The results showed a good correlation between ultrasonic parameters and Young's modulus. This suggests ultrasonic waves could be used to assess the condition of concrete structure during LTO.

ACKNOWLEDGEMENTS

First of all, I would like to express my deep gratitude to my supervisor A/ Prof. Murakami Kenta for his guidance and great support throughout my research. It has been a great honor to be one of his first Ph.D. students. He has spent a lot of time for discussion, finding the solution, and giving valuable ideas. I am very grateful for his generous and financial support to make my Ph.D. productive.

I would like to thank Prof. Suzuki Masahide for welcoming me to his laboratory and thoughtful guidance during my Master's course, as well as his continuous support during my Ph.D. course. I am grateful to Dr. Do Thi-Mai-Dung for her help with my experiments and for giving me valuable comments throughout my research.

I would like to thank Prof. Hisayuki Suematsu, Prof.Tatsuya Suzuki, Prof. Takumi Shimomura, and A/Prof. Tsuyoshi Honma for their insightful comments and questions for improving the clarity of this thesis.

I would like to thank Dr. Duong Thanh Tung, all members of the Nuclear Material and Maintenance Research Lab, and my friends for their support, advice, and friendship during my study and living in Nagaoka.

Many thanks to the staff at Analysis Centers at the Nagaoka University of Technology and at the HIT facilities at the University of Tokyo for their support and friendly help during carrying out the experiments and analysis.

Special thanks to my family. Thanks to my wife, my little daughter, and my newborn son for their love and encouragement.

Nagaoka, March 2021

Luu Vu Nhut

CONTENT

LIST OF FIGURES

LIST OF TABLES

CHAPTER 1: INTRODUCTION AND BACKGROUND

1.1. Overview of aging management and life extension program

As the end of 2019, there are 443 operational nuclear reactors in the world, mainly light water reactors (LWRs), which contributes to a total capacity of 392.1 GW(e) and accounts for around 10% of global electric generation; 13 reactors have permanently shut down including 5 reactors in Japan related to Fukushima Daiichi nuclear accident (FDNA), according to IAEA in 2019 [1]. Among that, contributing 65% of total capacity is over 30-years-reactors, and 17% of the total capacity for over 40-years-reactors, that is the initial operational limit [1]. However, the construction of a new reactor is difficult, especially in the US and Japan, only 54 reactors are under construction in the world, with 11 and 7 reactors in China and India, respectively. This picture tells us the importance of aging management for ensuring the safety of long-term operation (LTO) of LWRs, as well as securing energy security and reducing greenhouse gases. To achieve these goals, a comprehensive evaluation of materials and components used in aging plants is critical. Thus, some countries have set the national program, called plant life management (PLM), in which, components and structures should maintain their functions during LTO as well as during several years of decommissioning.

In LWR's condition, radiation degradation is the main issue of property changes of components and structures which are located close to the reactor pressure vessel (RPV). Under exposure of irradiation field, the initial properties such as the resistance of brittle fracture in RPV, the load-bearing capacity and seismic resistance in concrete structure gradually decrease over time and the lifetime of a component is determined when its properties decrease to the acceptable limit, as seen in Fig.1-1.). This consideration is more preferred during normal operation. However, the

existence of "hot spot" (i.e., local high temperature and high radiation flux), as well as the occurrence of accident, can accelerate the degradation process or cause a sudden failure of components. Therefore, for PLM, ***aging of structure and components should be considered both during normal operation, and transients due to accidents.***

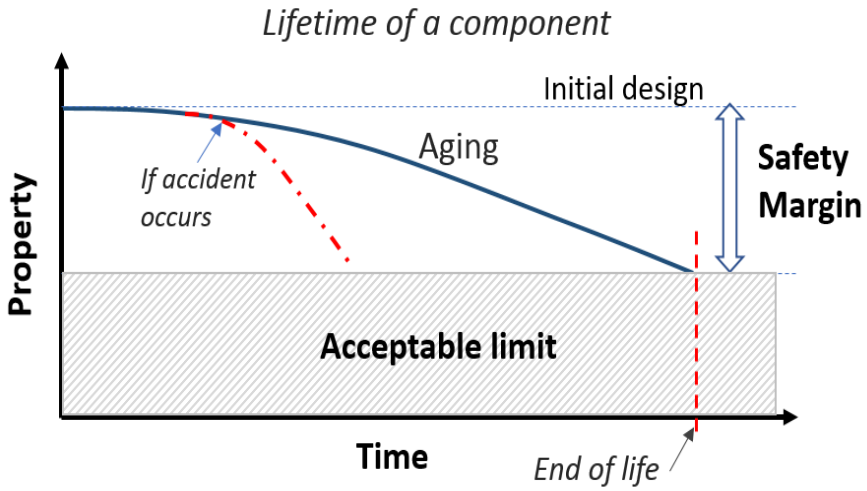

Fig.1- 1. The lifetime of a component as a function of time

In the US, the lifetime extension of up to 60 years of operation has been approved [2] and is considered up to 80 years [3,4]. According to Rosseel et al (2016), the PLM program focuses on the evaluation of aging of structure and components under the effects of exposure time, temperature, stress, coolant and irradiation fields [5]. The focus is mainly on non-replaceable components such as RPV and concrete structures (e.g., concrete biological shield (CBS)) because they are large structures and directly affects the safety and lifetime of a plant. For concrete structures, the main task of the PLM program are [5]:

(i) *to assess the environment in CBS and estimating the expected level of radiation*

(ii) *to harvest the real data from decommissioning reactors*

(iii) *to establish upper bounds of radiation damage in prototypical concrete and components using the accelerated test of irradiation ions, neutron, and gamma rays*

(iv) *to develop the model to understand the degradation mechanism*

(v) *to establishing international collaborations for knowledge exchange*

In Japan, more than 20 reactors have been operated for over 30 years and 3 of that are after 40 years. A program called Aging Management Technical Evaluation (AMTE) every 10 years for 30 years-reactors has been launched before FDNA [6]. The PLM program is led by the Japan Nuclear Energy Safety Organization. The purpose of PLM is to identify the impacts of environmental degradation conditions such as elevated temperature and radiation on long-term performance and changes in compressive strength. For assessing the soundness of concrete structures, three measures of degradation are considered:

(i) reduction in compressive strength

(ii) reduction in shielding performance.

(iii) reduction in seismic resistance

Generally, the 40 years-aged-plants in Japan can only be extended to maximum 20 years after passing a special evaluation [5].

1.2. Concrete Biological Shield (CBS)

CBS structure is a circular wall bounding the reactor pressure vessel. CBS is working under the harsh environment of radiation fields and thermal radiation from the reactor, which could affect the concrete's longevity. CBS has the following main functions:

(i) to attenuate radiation from neutron and gamma rays

(ii) to support the heavy nuclear reactor vessel.

(iii) to transfer the seismic load of the reactor to the foundation, in some design.

In boiling water reactors, the atmosphere inside CBS is filled with N_2 gas to generate negative pressure for preventing radioactive materials from releasing as well as preventing hydrogen explosion. The pressure, temperature and humidity are monitored and maintained within the limits specified regarding safety regulation.

1.2.1. Concrete used in CBS

Concrete used in LWRs is not much different from that used in other structures such as buildings and bridges, except for some special applications utilizing heavy concrete to reduce the thickness. Concrete is made by mixing aggregates, cement powder, and water with an appropriate water-to-cement ratio (w/c), varying from 0.4 to 0.6.

Cement paste

Ordinary Portland cement (OPC) is used in the construction of CBS, though there are other types of cement such as Pozzolana cement and alumina cement. The mixture of OPC cement and water will form a cement paste, which consists of hydration products (i.e., water-phases) and pore structure. The pore structure contains air voids, capillary pores and gel pores and plays a vital role because it affects the concrete properties and as a basic factor controlling the strength of concrete [7]. It is known that the less porous concrete will exhibit higher strength.

The main phases in cement paste are calcium–silicate–hydrate (C-S-H structure) occupied 50–60%, calcium hydroxide ($Ca(OH)_2$) about 20%, and other compounds such as clinker (C_3S and C_2S) and ettringite [8]. With complex multi-constituent and multiscale structure, the concrete structure can be divided into four scales (Fig.1-2.):

- Scale 4: Concrete (mortar + aggregates)
- Scale 3: mortar (a mixture of fine aggregates (sands) and cement paste)
- Scale 2: hydration products (a mixture of water and cement), $>10^{-6}$m
- Scale 1: C-S-H solid and gel pores, $>10^{-9}$ - 10^{-10}m.

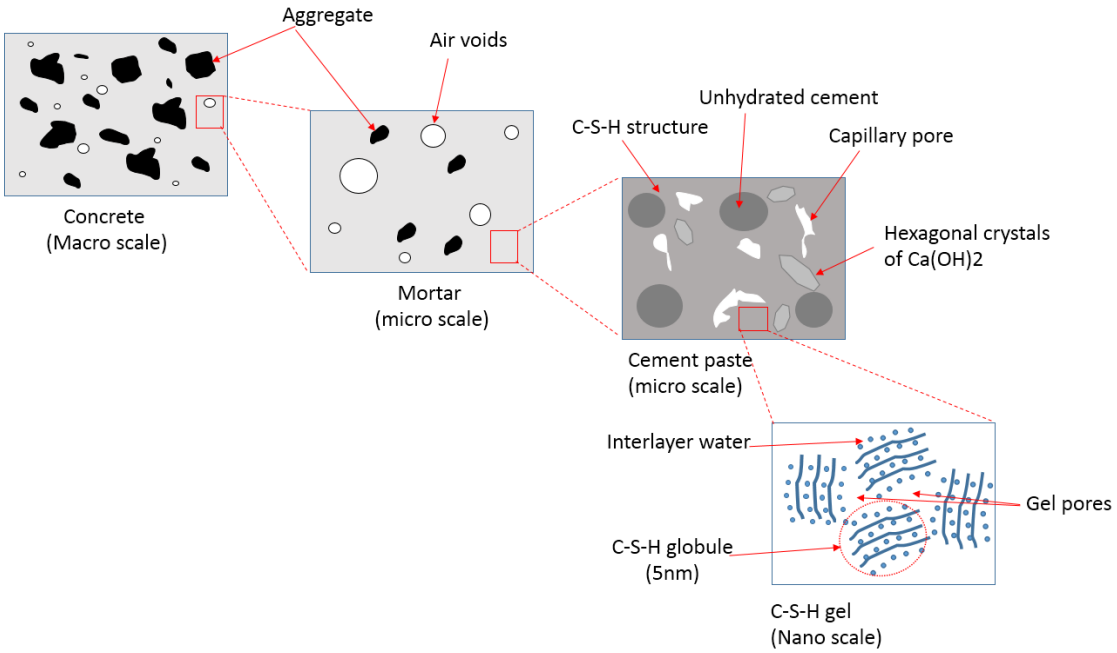

Fig.1- 2. The multi-scale structure of concrete (schematic)

Aggregate

In concrete, aggregates are categorized by fine aggregates (<5mm in particle size, such as natural sand or crushed stone) and coarse aggregates (around 5mm - 40mm in diameter). Because aggregates make up around 70-80% of total concrete volume [9], the properties of aggregates could strongly affect the mechanical properties of concrete. For shielding and attenuating the neutron, concrete must maintain enough amount of water or boron because neutron can be effectively shielded by light elements like hydrogen or can be absorbed by boron. For this purpose, boron-

containing aggregates (such as colemanite $Ca_2B_2O_{11}.5H_2O$, ulexite) and hydrous aggregates such as serpentine, limonite can be used [10].

Based on the origin, rock-forming aggregates can be categorized as [11]:

(i) **Igneous rocks** *(formed by cooling and solidification of magma)*: granite, albitite, gabbro, basalt, pyroxenite, hornblendite, olivinite; dunite, …

(ii) **Sedimentary rocks** *(formed by accumulation or deposition mineral or organic particles)***:** sandstone, calcium-bearing limestone, dolomite, magnesite, …

(iii) **Metamorphic rocks** *(formed from existing rocks through recrystallization)***:** hornstone, serpentinite, …

(iv) Ores

However, the above categorization is failed to describe the susceptibility to the Radiation-Induced Volume Expansion (RIVE), which will be described more detail in Section 1.3.2. The aggregates can be categorized into three groups as [12,13]:

(i) Silicate-bearing aggregates (i.e., high susceptibility to RIVE): sandstone, serpentine, flint, dolerite, …

(ii) Carbonate-bearing aggregates (i.e., low susceptibility to RIVE): calcite, dolomite, siderite, magnesite, ...

(iii) Oxides

It is difficult to determine the mineral composition in aggregates because there are more than 4500 different minerals in nature. Silicate minerals are most common in rock-forming aggregates because it is composed of 90% on the Earth's crust. Feldspar minerals are most abundant among silicate minerals, which contain about 40% plagioclase (a series of minerals from albite $NaAlSi_3O_8$ to anorthite $CaAl_2Si_2O_8$) and 10% alkali felspars ($KAlSi_3O_8$) [14]. In silicate minerals, the basic

structure $[SiO_4]^{4-}$ (Si tetrahedron) is the building block to form the mineral structure, thus mineral properties are commonly associated with the topology of the network that is built by basic structures [12].

Since aggregates are polycrystalline of different minerals (as an example in Fig.1-3), the mineral composition is diverse, even in the same type of rock. Igarashi et al, (2015) have collected siliceous rock samples at several locations in Japan and showed that SiO_2 content varies from 50% - 90% by mass, followed by Al_2O_3 from 2-17%, and the remaining are related to alkali oxides such as Na_2O and K_2O [15], as seen in Fig.1- 4.

It has been shown that concrete aggregate plays important role in shielding performance; however, there is a consequence caused by the exposure to radiation fields which significantly affects their mechanical properties. This will be reviewed in the following sections.

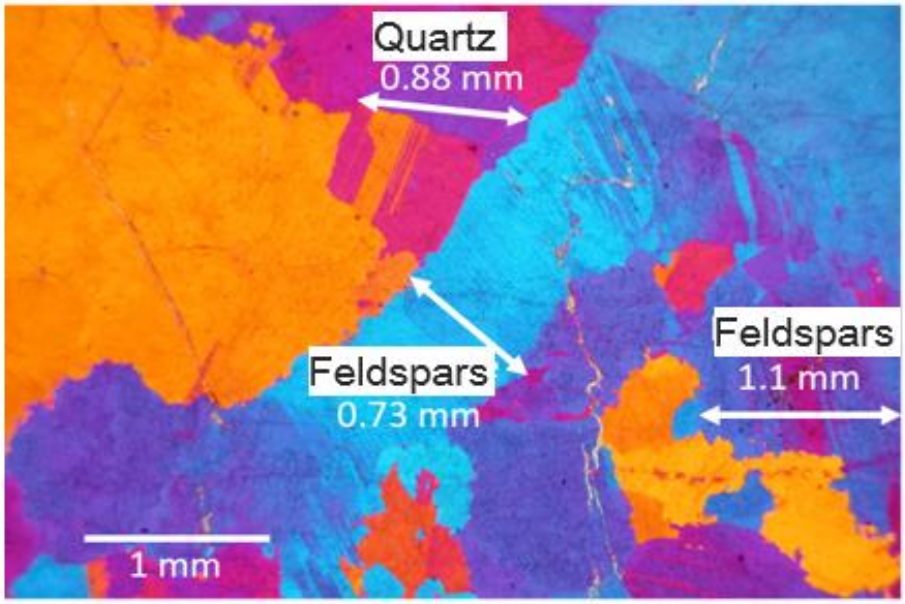

Fig.1- 3. Structure of a silicate-bearing aggregate including quartz and feldspars [16]

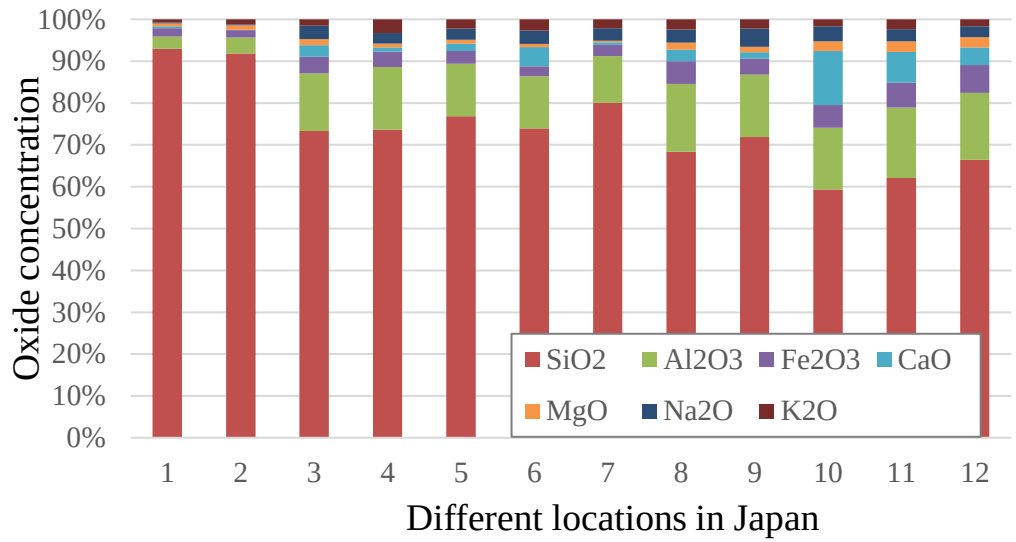

Fig.1- 4. Diversity of chemical composition of siliceous rocks in different locations in Japan [15]

1.2.2. Working environment in CBS

In normal operation, CBS is subjected to long-term thermal radiation directly from the hot reactor (~300^{o}C) and radiation field of neutron and gamma-rays, as illustrated in Fig 1- 5. However, the regulation limits the exposing temperature of inner CBS surface less than 65^{o}C [17], thus thermal radiation is not significant if monitoring functions are well maintained. Nevertheless, the temperature inside CBS can be increased by the interaction between radiation and concrete materials through the ionization process. This is due to the irradiation particles transfer their kinetic energy to the target atoms as thermal vibration along the depth of penetration. In a special case, radiation could lead to increase the temperature up to 250^{o}C [18]. This temperature could cause capillary water loss and can lead to a decrease in compressive strength up to 20% [19]. Thus, it has been recommended an irradiation flux of less than 10^{10}MeV/cm^{2}.s during operation to prevent radiation heating [20]. Furthermore, radiation can cause drying (or water loss) through the radiolysis process since concrete contains a high amount of water, this could be an important

issue related to irradiation for long-term operation, particularly during extended period. The expected conditions of inner CBS in a US reactor up to 80 years of operation are as summarized in Table 1- 1 [5]. It shows that the accumulated radiation dose can reach up to 6 x 10^{19} (n/cm^2) for neutron and 2 x 10^8 Gy for gamma-rays, and a strong gradient in humidity will occur inside the CBS wall.

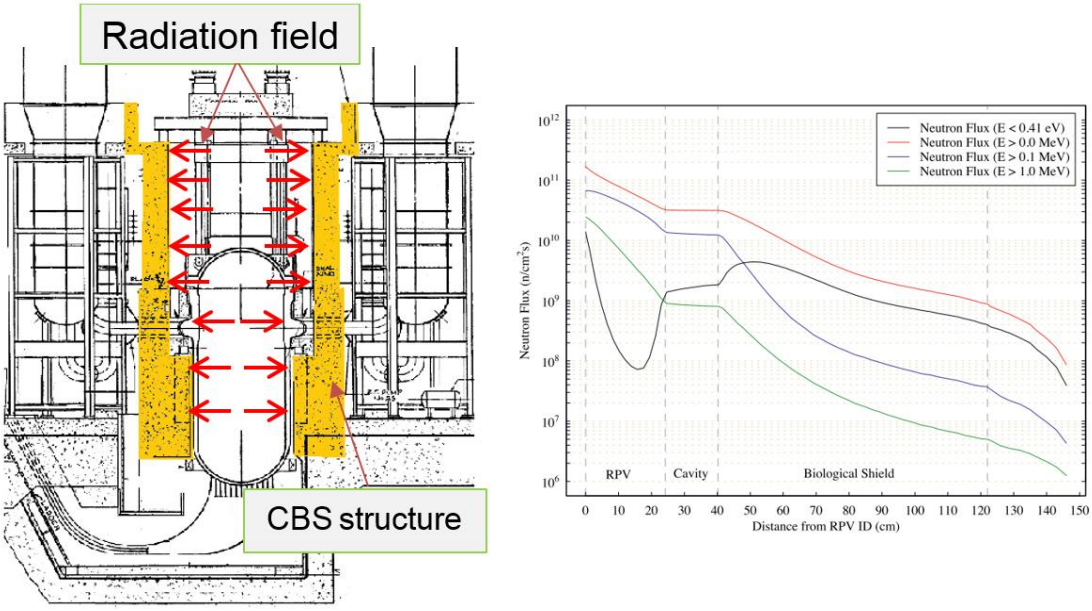

A typical PWR biological shield

Fig.1- 5. Distribution of neutron fluence in the three-loop PWR from the reactor core to CBS structure [13]

Table 1- 1.Working condition during normal operation and expected conditions after 80 years of operation [5]

Parameters	PWR (inner CBS)	Test reactors
Fast neutron flux (n/cm^2/s)	1 to 2 × 10^{10}	5 × 10^{11} to 2 × 10^{14}
Fast neutron fluence (n/cm^2)	<6 × 10^{19} at 80 years	<10^{20}
Gamma flux (kGy/h)	5 to 20	0.02 to 200
Gamma dose (MGy)	50 to 200 at 80 years	0.04 to 1.3
Temperature (°C)	<65 (design)	40 to >250
Relative Humidity (-)	Strong gradient *~0.5 at 50 mm, ~0.7 at 150 mm,* *>0.9 at 400 mm,* at 30 years	

1.3. Environmental impacts on CBS

Concrete is known to be aging over time due to continuous hydration, but it does not have a significant impact on the performance. However, environmental influences, such as physical and chemical attacks, may cause undesirable changes over time. The long-time use of concrete provides a solid understanding of concrete degradation under ambient temperature applications such as building, bridge as well as special applications such as chemical plant and seawater, but not for high temperature and radiation due to less occurrence. In general, the performance of concrete in LWRs is very good because of well controlling of material selection and safety measures to prevent exposure to chemical attack; however, extending lifetime leads to high accumulated irradiation dose which would change concrete properties i.e., reduction in compressive strength and elastic modulus due to RIVE in aggregates and/or radiation heating in cement paste, which has received large attention recently. Several authors have reviewed the degradation issues in concrete used in NPPs, such as [5,10,17,18,21–23], however, some contents seem to be overlapped due to limited new experimental data. For the sake of completeness, the effects of high temperatures are also reviewed to identify the upper bounds of damage caused by temperature and drying, but it is also considered to occur due to existing of "hotspot" or unexpected accidents.

1.3.1. Temperature effects on concrete and its components

Microstructure changes

Several researchers have reviewed the impact of temperature on concrete, such as [9,19,24,25]. Exposed to high temperatures, free water and bound water in cement paste gradually evaporate up to 400°C, and then the decomposition and phase transformations occur beyond 400°C, as summarised bellow:

(1) **Water loss stage**: up to 105°C, evaporation of free water from capillary and cavity takes place. Between 80 to 150°C, the decomposition of ettringite occurs [9]. The loss of bound waters in hydration products is expected up to 500°C [26]. The physical-bound water (in capillary pores) evaporates at 180°C. Interlayer and bonded water in C-S-H structures evaporate at 350°C and 400°C, respectively [27]; they are the chemical-bound water.

(2) **Phase transformation and decomposition stage**: Between 400°C and 500°C, the calcium hydroxide $Ca(OH)_2$ decomposes into CaO and H_2O [9,26]. Between 600°C and 800°C, the C-S-H decomposed into anhydrous calcium aluminum silicate and <β-C_2S and C_3S> [9,28]. At 573°C, quartz mineral transforms from α to β phase accompanying volume change [28].

These changes in microstructure lead the cement paste to shrink, while aggregate expands, thus cracks could be formed in concrete. This could be the source of reduction in mechanical properties at high temperatures.

Changes in mechanical properties

At ambient temperature (<40°C), loss of strength is not significant; however, it can reduce by 10% up to 90°C. Chan et al (1999) reported that the significant loss of strength of concrete is in the range of 400 and 800°C from 15% to 80% of its initial strength [29]. Peng et al (2008) proposed that the strength loss of concrete below 600°C mainly caused by the pore-structure coarsening regarding the formation of microcracks [30]. Handoo et al (2009) found that the physical state of concrete degraded significantly at a temperature higher than 300°C, and the loss of strength became significant beyond 500°C [31]. The loss of strength with temperature is well documented by Kodur 2014 [19], as shown in Fig.1- 6.

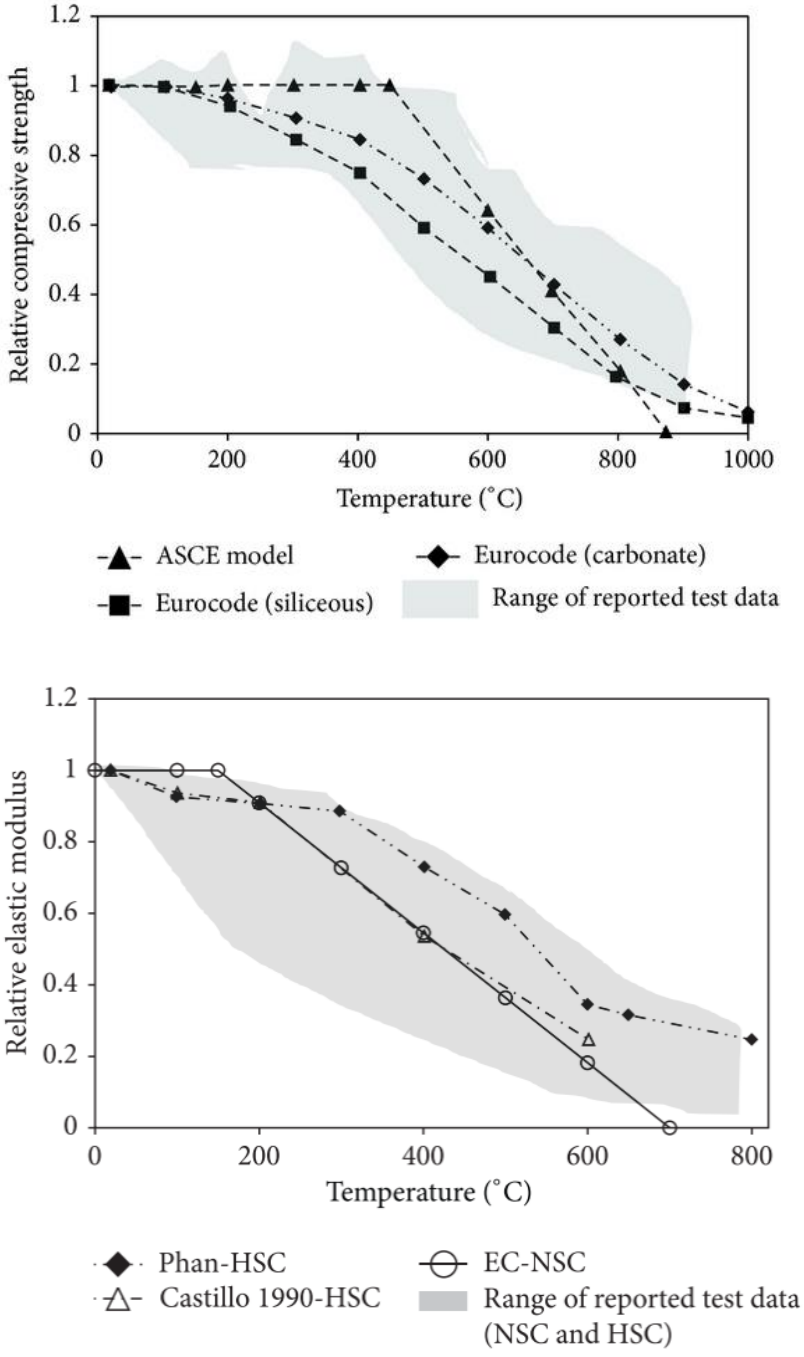

Fig.1- 6. The relative change of mechanical properties due to high temperature [19]

The response of concrete at elevated temperature depends on several parameters such as heating rate, type of aggregates, humidity, and water-to-cement ratio. For

example, the fast-heating rate can cause surface spalling; siliceous aggregates may cause a larger reduction in strength due to their higher thermal expansion than that of carbonate aggregates. Such difference in thermal behavior is analog to that of RIVE (i.e., RIVE in siliceous aggregate concrete is more significant than that in carbonate aggregate concrete). According to Hager (2013) [9] and Grattan-Bellew (1996) [28], the thermal properties of aggregates are stable up to 300°C; however, as the temperature rises to 500 - 600°C, the quartz-bearing aggregate undergoes crystal transformation and associated thermal expansion, leading to increasing the aggregate's volume about 5% [28]. This may result in cracking and spalling of the concrete.

1.3.2. Radiation effects on concrete and its components

Neutron is categorized into three types: thermal neutron (E <1eV), epithermal neutron (1eV < E < 0.1MeV), and fast neutron (E>0.1MeV). Neutron is generated directly from nuclear fission of uranium-235 when it absorbs a thermal neutron and releasing two or three high kinetic energy neutrons, which is called fission reaction. Gamma-rays are generated directly from the interaction of neutrons with nuclei or from the emission of radioactive materials generated from fission and other processes. Though neutron and gamma rays have no charge, they interact differently with concrete:

- Gamma-rays are ionizing radiation and have energy higher than 0.1MeV. The ionization is quantified as the absorbed dose which has the unit of Gy (gray): joule/kg (1 Gy = 10 rad). The interaction of gamma-ray with an atom mainly in three different ways: photoelectric effect, Compton scattering, and pair production [32], as illustrated in Fig.1- 7.
- Due to neutral change, neutron can penetrate deeper into the matter and mainly interacts with the nucleus of the atom through elastic and inelastic collision.

When a fast neutron collides with a nucleus, it transfers some kinetic energy to the target atom and changes its direction. The first collision is called a primary knock-on atom (PKA). The process can generate scattered gamma-rays, so-called inelastic scattering, and without generating gamma-ray is called elastic scattering. The knock-on process may repeat several times until fast neutrons become epithermal neutrons and thermal neutrons. When a thermal neutron interacts with a nucleus, it's all energy is absorbed, and no further reaction occurs. In covalent materials, the PKA can also cause ionization due to having a charge, as illustrated in Fig.1- 8.

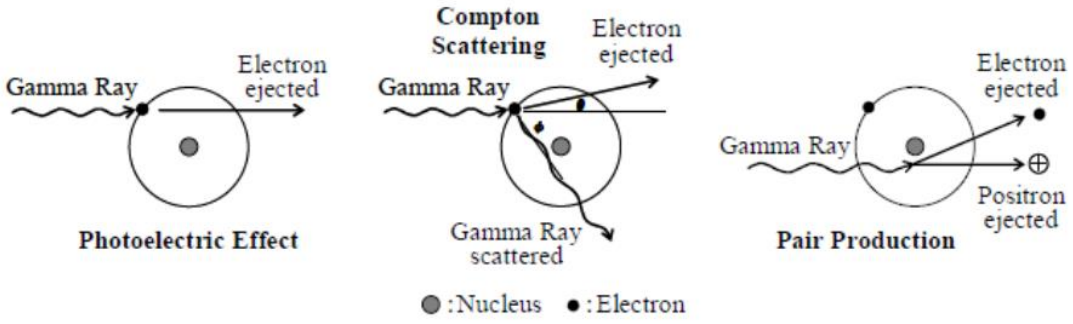

Fig.1- 7. The photoelectric effect, Compton scattering, and pair production by gamma-rays [32]

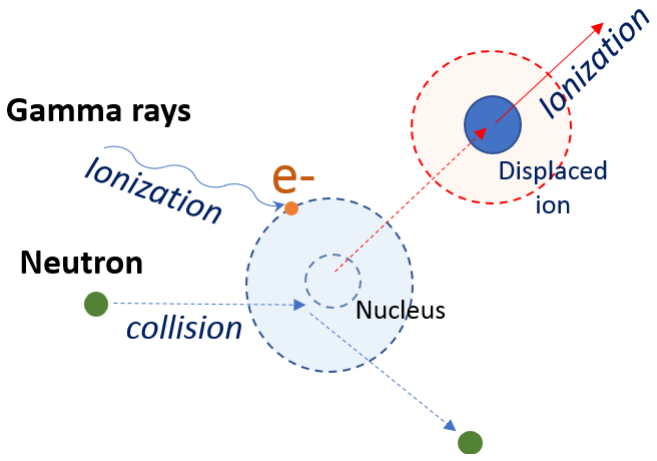

Fig.1- 8. Schematic interaction of neutron and gamma-rays with an atom

Due to different interactions, neutron and gamma-rays cause different effects on concrete's components:

- The impact of gamma is significant on the hydration products (i.e., water-phases) of cement paste because ionization can decompose both physical- and chemical-bound water through the radiolysis process, and results in shrinkage. In aggregate, gamma rays affect covalent bonds (i.e., Si-O bonds) rather than ionic bonds. Once the interatomic bond (Si-O) in aggregate is broken, it distorts local topology and gradually leads to crystal-to-amorphous transformation i.e., amorphization when a high level of distortion in the network is reached.
- On the other hand, neutron does not cause a significant impact in cement paste due to the poorly crystalline phase of C-S-H and pore structures, thus irradiation defects can be healed by alkali ions [32]. That is opposite to well-crystalline aggregates, in which neutron can cause knock-on displacements and progressive amorphization will occur. Because amorphous solid is less dense compared with its crystalline state, volume expansion will occur during amorphization (i.e., RIVE).

In general, both neutron and gamma rays could cause amorphization, but neutron requires less deposited energy to render amorphization than gamma rays, which is about three order difference in deposited energy [33]. A good summary has been compiled by Maruyama et al, 2017 [16] regarding the effect of gamma and neutron on cement paste and aggregates, as shown in Table 1- 2. In addition to that, amorphous transformation in aggregate can assist chemical degradation such as carbonation [34] and alkali-silica reaction [35,36]. Thus, along with RIVE issue, chemical degradation has also attracted several researchers recently.

Table 1- 2.The summary of possible effects of irradiation on concrete component [16]

		Gamma-rays	Neutrons
Cement paste	Water	-Gamma ray irradiation enhance the drying of cement paste.	- Neutron irradiation enhance the drying of cement paste
	Solid	- Impact of gamma-ray on cement paste is same as that of heating or drying.	- Impact of neutron on cement paste is comparable to that of heating or drying.
Aggregate	Water		
	Solid	- Impact of gamma-ray on aggregate is same as that of heating and drying in the realistic dose range, while the metamictization should occur due to irradiation theoretically.	- Aggregate expands due to metamictization. - α-quartz is the most sensitive to neutrons and α-quartz content of aggregate is the major factor of expansion rate and ratio of aggregate in the realistic fluence range.
Concrete		- Strength and Young's modulus change due to gamma-ray irradiation are almost comparable to those due to heating or drying.	- Concrete expands due to expansion of aggregate. - Compressive strength and Young's modulus of concrete decreases due to crack opening caused by expansion of aggregates.

Radiation effect on mechanical properties of concrete

It is important to find the critical irradiation level for gamma and neutron irradiation in concrete, beyond which concrete starts to degrade the properties, such as compressive strength and Young's modulus. Several accelerated tests were conducted during the 1960s and 1970s to support a new type of reactor for high-temperature gas-cooled reactors, and the data were summarized by Hisdorf et al, (1978) [22]. Based on this study, a reference level of $1x10^{19}$ (n/cm^2) for fast neutron and 2×10^8 Gy by gamma-rays has been recommended for concrete structures by some regulation bodies [21,37]. However, Kontani et al, (2013) re-analyzed the data collected by Hisdorf et al and found that the data at high neutron fluence conditions were not typical for concrete used in LWRs because of the irradiation temperature beyond 100°C, as well as different types of tested concretes (as Fig.1- 9). Therefore, this requires further study to re-define the critical values.

Recently, K. Field et al, (2015) compiled several neutron-irradiated data confirmed that concrete strength started to decrease after $1x\ 10^{19}$ n/cm^2 [13], as shown in Fig 1- 10. This was consistent with new neutron-irradiated data obtained by Maruyama

et al (2017) [16]. However, there are remaining large scattering due to various unknown factors related to the diversity of aggregates, variation of neutron spectrum and neutron energy cut-off for counting neutron fluence among researchers.

Based on the current review, the main causes of reduction in mechanical properties were considered to be related to the RIVE effect in aggregates caused by neutron irradiation, and the drying of cement paste due to gamma-irradiation.

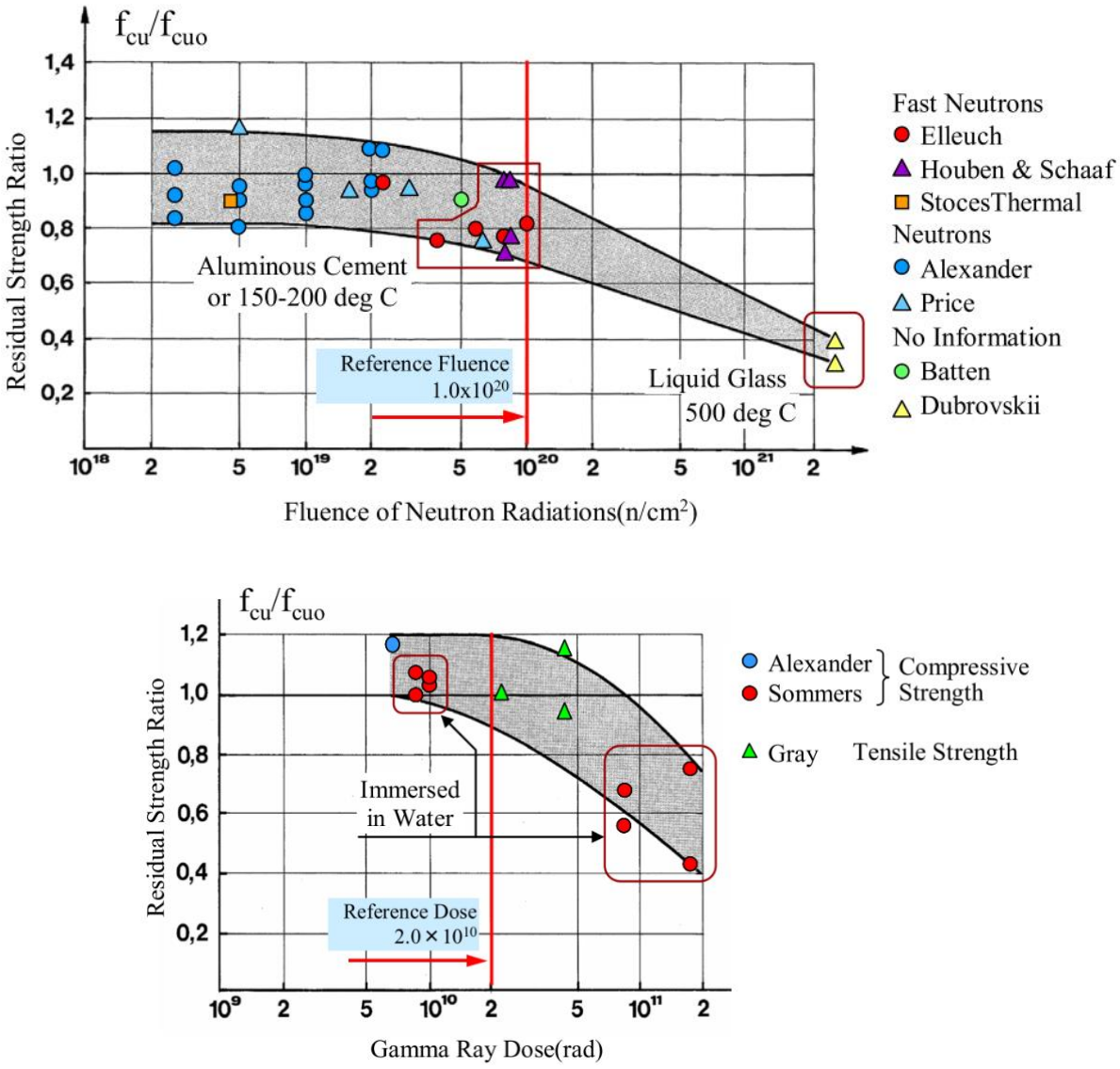

Fig.1- 9. Relative change of compressive strength with neutron and gamma-ray, interpreted by Kontani [32]

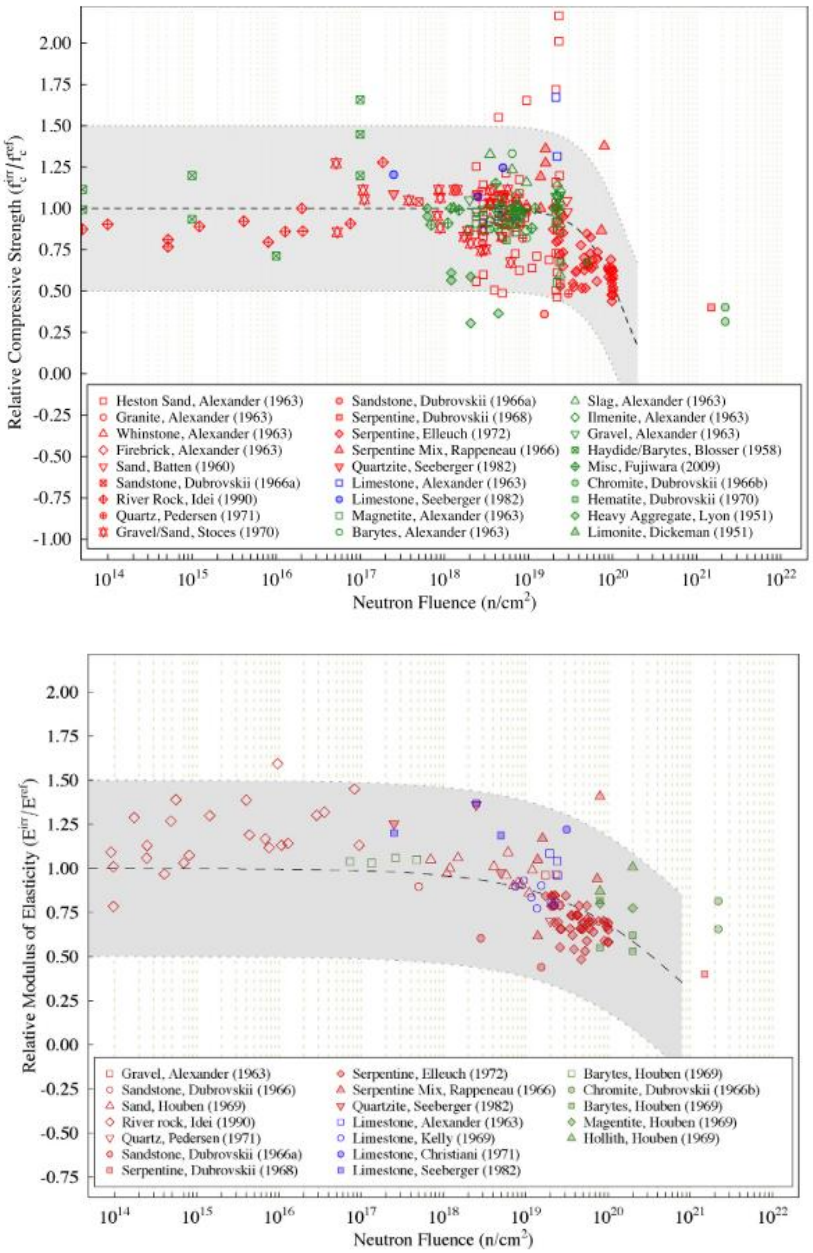

Fig.1- 10. Relative change of compressive strength and Young's modulus with neutron fluence. Noted that the data were obtained by different neutron spectrum and energy cut-off [13]

Radiation effect in cement paste

Bouniol and Aspart (1988) showed that radiolysis (due to ionization) of water can produce hydrogen and hydrogen peroxide (H_2O_2). Since hydrogen peroxide can react

with portlandite ($Ca(OH)_2$) in cement paste, it can cause the decomposition of cement phases. The product of this reaction is peroxide (O-O) and then carbonation with CO_2 occurs. Note that, natural carbonation is a chemical reaction between portlandite and CO_2 to form calcite ($CaCO_3$), this reaction causes a reduction in pH in concrete from 12 - 13 to lower than 9 [38]. Vodak et al (2005) reported the effect of gamma rays on the decomposition of cement paste and showed an increasing amount of calcite with increasing dose. In addition to that, the compressive strength was reduced by about 15% at $4x10^5$ Gy (as seen in Fig.1- 11.) [39]. This result raises a concern on structure safety because the current threshold dose for gamma is in order of 10^8 Gy, this change was considered due to an excessive amount of calcite formed, this causes microcracks near the pores and may contribute to strength reduction. Furthermore, Vodak et al (2011) carried out another experiment of gamma irradiation in cement paste up to $1.6x10^6$ Gy and showed that the radiation-induced carbonation increased the pore space and it occurred in the whole sample [40], this is different from that natural carbonation that mainly takes place at the surface layer of concrete.

However, a comprehensive study conducted by Maruyama et al, [16,41] recently has found gamma irradiation increased the concrete strength (as Fig.1- 12**)**. They carried out the carbonation test by injecting CO_2 with and without irradiation. Under irradiation, the aragonite and vaterite were formed on C-S-H structure, whereas the calcite was produced without irradiation condition. The increase of strength is related to the vaterite which is formed by the rapid drying of hydration products due to gamma-ray heating and radiolysis of water, and it filled the pores around C-S-H [36]. Therefore, authors [36] concluded that "*concrete structures exposed to gamma-ray irradiation do not require special treatment from the viewpoint of the physical properties of the concrete, but instead only the impacts of heating and drying should*

be taken into account". It means the concerns raised by Vodak should be considered as drying effect by gamma heating.

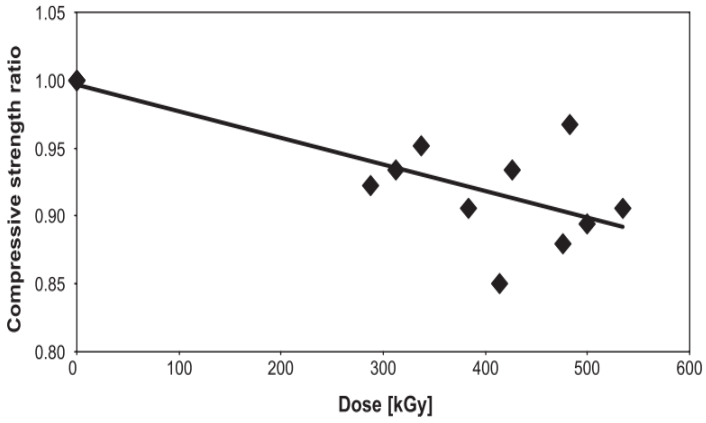

Fig.1- 11. Relative change of concrete due to gamma irradiation (0 - 5 x 10^5 Gy) [39]

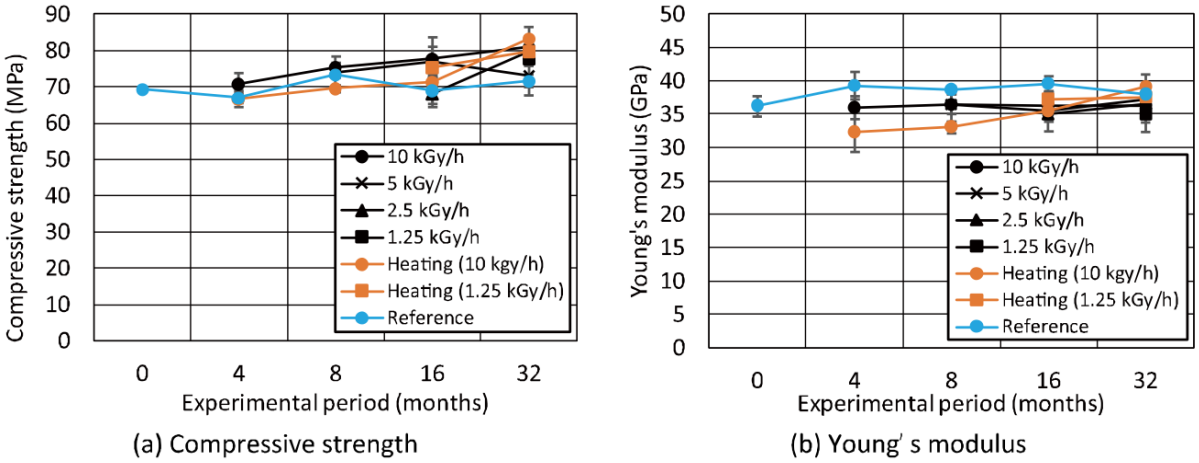

Fig.1- 12. The relative change of mechanical properties with gamma irradiation [16]

Radiation-induced volume expansion (RIVE) in aggregate

Based on the review, both neutron and gamma irradiation can cause the disordering of lattice structure and leading amorphization with volume expansion due to the reduction in density; however, there are no reported data regarding the volume

change caused by gamma irradiation. This can be due to the very high deposited energy (i.e., beyond 100GGy [42], which is much beyond LTO for LWR condition) to render amorphization. By neutron irradiation, Field et al (2015) collected several data of dimension change in unembedded aggregates and concrete, as presented in Fig.1- 13 [13], showed that volume expansion in concrete occurred beyond 1 x 10^{18} (n/cm^2) and significantly after 1 x 10^{19} (n/cm^2). Furthermore, siliceous aggregates expand larger than carbonate or heavy aggregates, thus it leads to a larger expansion in silicate-bearing concrete than that carbonate and heavy-weight concrete [13]. Based on this data, the ***expansion of aggregate can be used as an indicator of the expansion of concrete***, ***and the reduction of mechanical properties is likely related to the RIVE of aggregates***. This also indicates that understanding the behavior of RIVE of minerals containing in aggregate is important to understand the irradiation degradation in concrete.

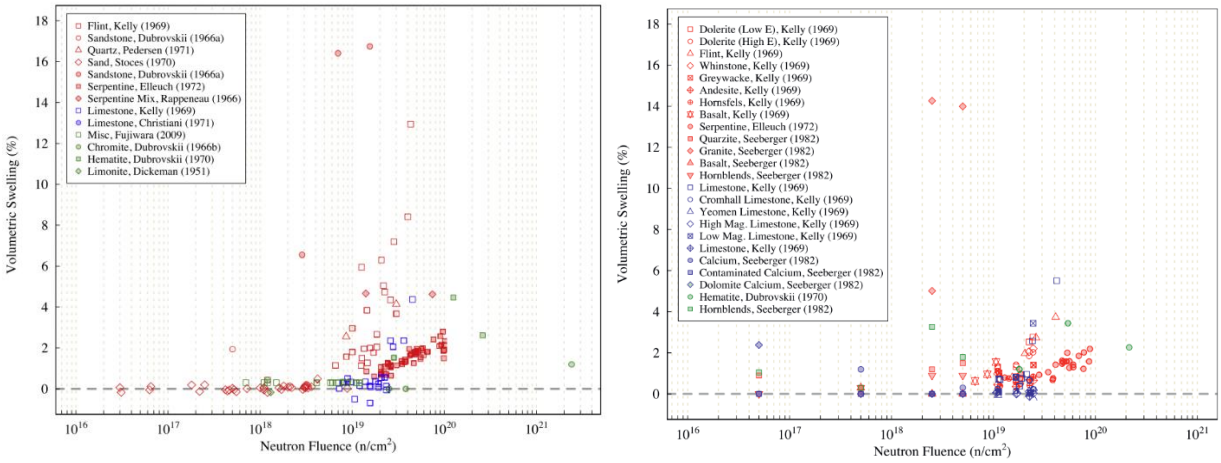

Fig.1- 13. The volume change in neutron-irradiated concrete (left) and in unembedded aggregates (right)

RIVE in irradiated minerals

The expansion of aggregate is an integrated swelling of each mineral since aggregate is polycrystalline of different minerals and oxides. It is believed that the RIVE is due

to amorphization. The amorphization of some silicate minerals has been studied by experiment [43–45] or using molecular dynamic (MD) simulation [46]. It is known that ionic bonds are more resistant to radiation, whereas covalent bonds poorly resist [47]. Le Pape et al, (2018) have shown that silicate minerals exhibited high expansion, and the highest RIVE in the case of quartz up to 18 %, followed by feldspars 8% under neutron irradiation, while carbonate minerals have very low expansion <1%. The RIVE is dependent on three parameters [12]: (1) **network topology** *(the dimensionality of SiO_4 polymerization),* (2) **bond type** *(the number of covalent bonds (Si-O)),* and (3) **bond energy** *(the relative bonding energy (RBE) of the unit cell).*

Amorphization and RIVE in quartz

Alpha-quartz is the most common silicate mineral with 100% covalent bonds, thus the resistance to amorphization in silicate minerals could be related to SiO_4 content [12,43]. As an important mineral in industry, the radiation effects on alpha-quartz has been intensively studied by several researchers using neutron [48–53], ions [54–60], and electron [61–64] as well as MD simulation [65–68], due to its wide range application, such as electronic devices and sensors. Though the basic structure has been well-known, the determination of the structure of amorphization is difficult [66,69]. Due to high susceptibility, highest RIVE, and high purity in nature, ***the behavior of quartz under irradiation has been utilized to simulate the RIVE behavior of concrete aggregate in the current mesoscale modeling code to predict concrete property change during LTO*** [13,16]. However, the basic understanding of the RIVE mechanism, the correlation between amorphization and RIVE, and environmental effects on RIVE in quartz are still limited due to different purposes of previous studies and mainly focusing on the amorphization.

Both ionization and elastic collision process can cause amorphization [58,70]. The critical dose of amorphization in quartz was reported by several units in the literature, such as deposited energy (eV/cm^3) or (eV/atom), as well as dpa. However, different techniques for identifying the amorphization dose lead to the variation of the threshold dose between researchers [43,58,66]. For example, the deposited energy required for transformation by the collision process varied from 0.04dpa by Rutherford Backscattering spectroscopy-channelling [60] to 0.21dpa using in-situ 1.5 MeV Xe^+ irradiation monitored by transmission electron microscopy (TEM) [45]. By electronic excitation, continuous amorphous tracks may be formed by individual ions when electronic stopping power is beyond a threshold value of 1.4 ~ 1.8 keV/nm by swift heavy ions [71,72] and the deposited excitation energy of about 2 x 10^{26} eV/cm^3 [33]. In the case of neutron irradiation, the critical dose in quartz has been considered as order of 10^{20} n/cm^2 (E>0.1MeV) [13].

The amorphization in quartz has shown directly related to density decrease [73]. Bolse (1998) suggested that the amorphization follows the *nucleation-growth model* introduced by Avrami, 1941 [74]. Based on experimental data, Field et al (2015) expressed volume change in quartz, $\chi(\%)$ as a function of neutron fluence, n as:

$$\boldsymbol{\chi(n) = 1 - \exp\left(-(n * K)^d\right)} \quad \textit{Eq.1- 1}$$

where, K and d are the temperature-dependent parameters, which is found to be 1.6×10^{-21} and 2.38, respectively in [13].

Regarding temperature effect, Bykov et al (1981) showed the rate of RIVE reduced at higher temperatures [48] and indicated the swelling starts at ~3×10^{19} (n/cm^2) for (energy cutoff, E_0>0.1MeV) and reached a full amorphization at ~1×10^{20} (n/cm^2) at 25-30^{o}C condition (Fig.1- 14). The reduction in RIVE rate is interpreted due to the recovery of point defects which tend to be enhanced at higher irradiation

temperatures. However, the recovery at such low temperatures is questionable and needs to be clarified.

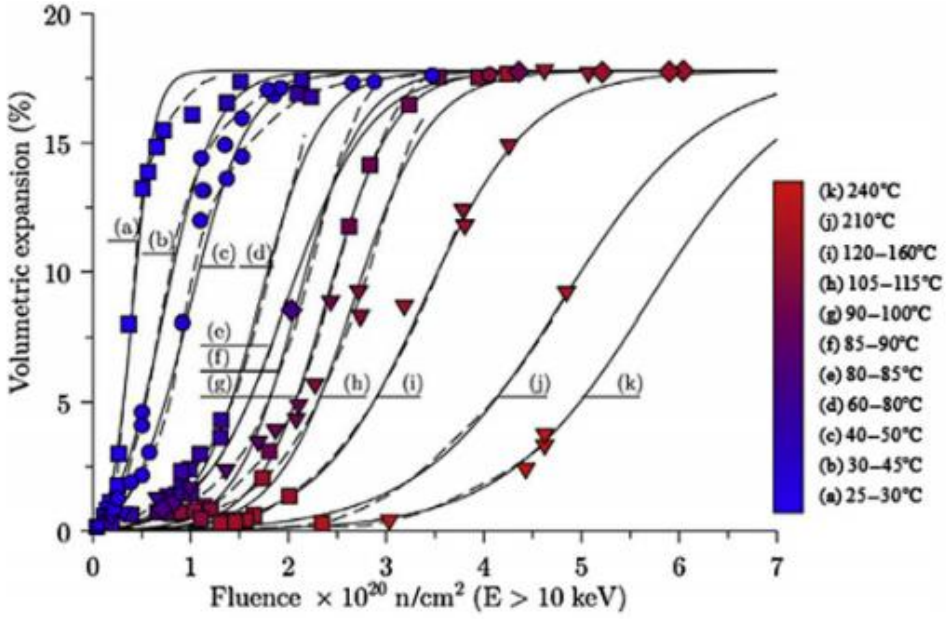

Fig.1- 14. The volume expansion in quartz under neutron irradiation at different temperatures [75] *(interpreted from* [48]*)*

Difference between vitrification and amorphization

Vitrification or glass formation is defined as a thermal process in which a melted compound has been cooled to a rigid condition without crystallizing [76]. Fig.1- 15 describes the process during glass formation. The start of this process is that the melting occurs at a high temperature. When the melt cools, its volume decreases. The crystallization starts at the melting point, T_m, where the volume significantly reduces. As the temperature decrease further, volume change is small. In the case when the cooling rate is very high, so-called *supercool*, a metastable-thermo-dynamic equilibrium state is formed at T_g ($T_g < T_m$), refers as *transformation temperature.*

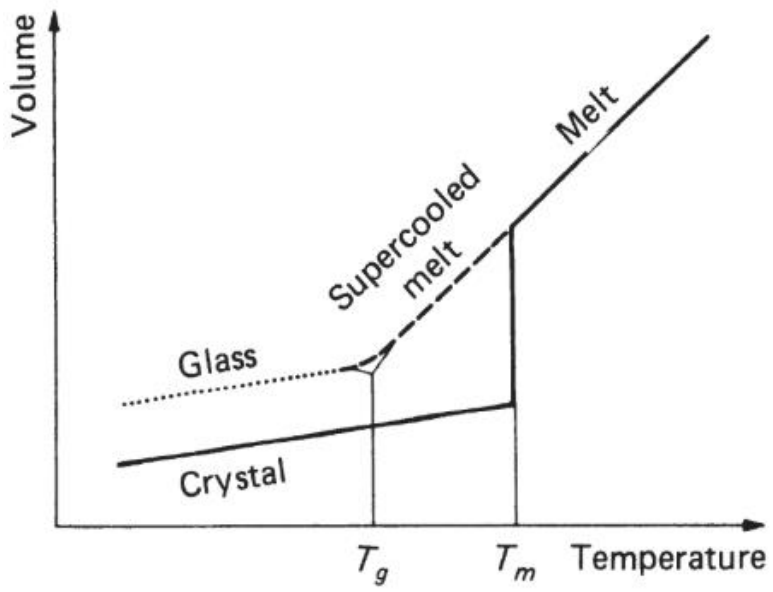

Fig.1- 15. Schematic diagram of temperature dependence of volume [76]

According to Zachariasen [77], the energy differences between glass and crystal of the same composition is very small, suggests the same bond types or basic structures (i.e., SiO_4 tetrahedron) as in its crystal. Nevertheless, the arrangement of basic structures is not in a well order (or random network), as shown in Fig.1- 16. Base on this basis, Zachariasen proposed four conditions of glass structure:

(a) The coordination number of the cation must be small.

(b) An oxygen ion may not be linked to more than two cations.

(c) The oxygen polyhedrons may share only corners, not edges or faces.

(d) At least three corners of every oxygen polyhedron must be shared by other polyhedrons.

Based on this model, the basic structure of glass is similar to that of crystal but there is an aperiodic topology (Fig.1- 16).

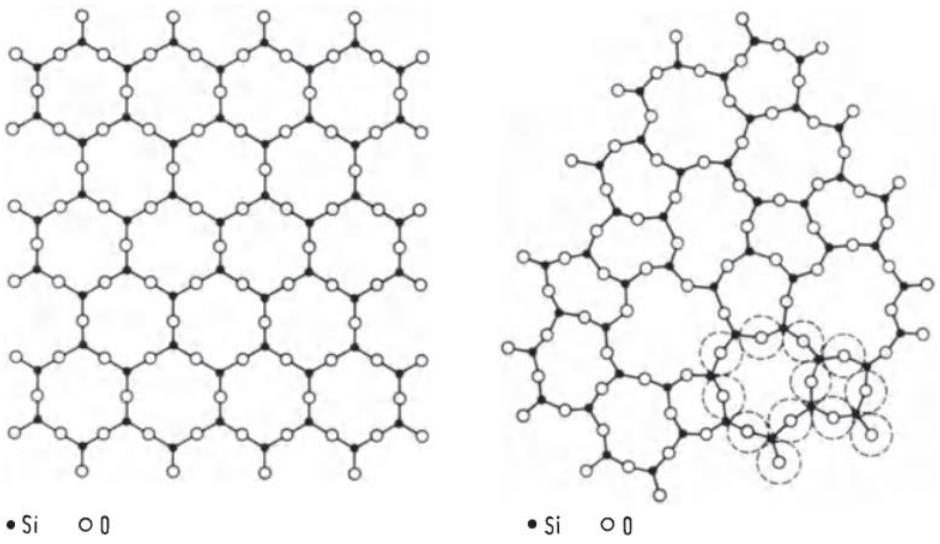

Fig.1- 16. Two-dimensional diagram of order SiO2 (left) and random SiO_2 (right).

Though the structure of vitrification and amorphization is difficult to be distinguished by diffraction techniques (X-ray diffraction, electron diffraction) due to aperiodic topology, there are some differences in short-range and long-range structure analyzed by molecular dynamic simulation. Krishnan et al (2017) showed that under and over coordinated defects are formed and the distribution of rings (number of Si-tetrahedra that are connected and form a close ring) is broader as illustrated in Fig.1- 17, this suggests that long-range structures such as cavity could be formed in the amorphized structure. However, the under/over-coordinated defects and large ring sizes are absent in the case of glass [78].

Fig.1- 18 summarizes the important aspects of radiation-induced amorphization and associated RIVE caused by neutron irradiation and/or gamma-ray in quartz without considering impurities. The amorphization caused by gamma-ray is considered due to the generation of electron-hole pairs and associated formation of point defects. Radiation damage by neutron is mainly through the knock-on process. Neutron firstly transfers its kinetic energy to the target atom and this atom will be displaced from its original position if it received energy higher than the displacement energy

threshold (E_d). The displaced atom collides with another atom and so on, these collisions generate damage cascade regions (or local damage regions) with a few nanometers in diameter and isolated point defects. In some cases, the displaced atom can cause ionization (this process may not occur in metal) and produces electron-hole pairs. The damage cascade regions are supposed to directly become micro-amorphous regions. Point defects could be free carriers (neutral charge), under/over coordinated defects (such as Si^{III}/Si^{V} and O^{I}/ O^{III}), and unpair defects (paramagnetic defect centers: oxygen vacancies (or E' centers), nonbridging oxygen hole center (NBOHC) and peroxy radical (POR)), these defects gradually accumulate during irradiation, eventually the amorphization occurs at a high concentration of defects. However, some defects are also recovered at a certain condition and/or at high temperatures, thus suppressing the RIVE. The RIVE could result from a combination of two processes, i.e., amorphization due to the reduction in density and relaxation of the local structure due to the existence of point defects. In current modeling codes, the maximum of RIVE occurs when the amorphization takes place and the RIVE is correlated to amorphization.

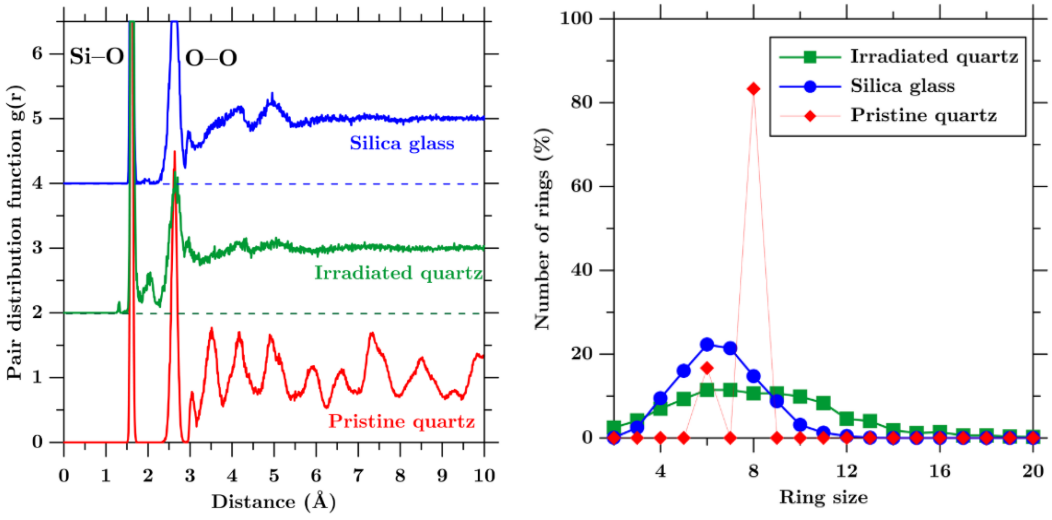

Fig.1- 17. Pair distribution function of pristine quartz (red), irradiated quartz (green), and glassy silica (blue) (left); and ring size distribution (right) [78]

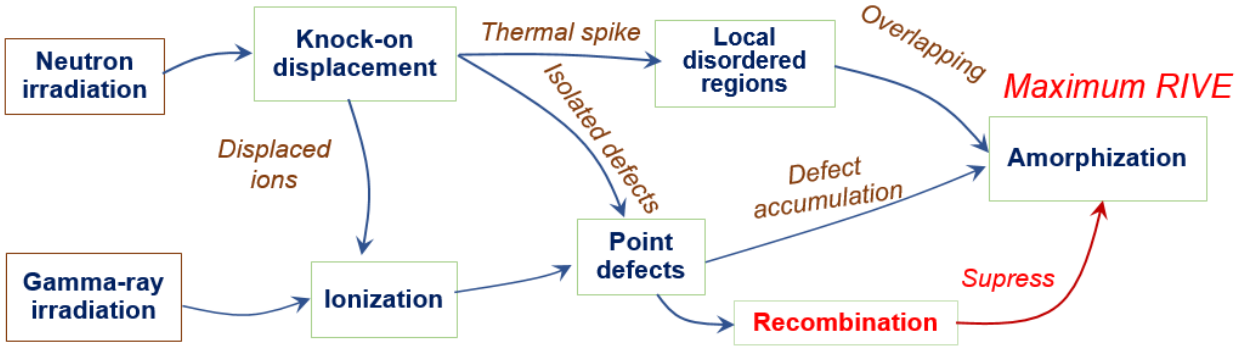

Fig.1- 18. Schematic radiation-induced amorphization and associated volume change

Changes in properties due to amorphization

Under irradiation, silicate minerals have indicated significant changes in physical properties, such as density, modulus, and hardness [46,79]. The reduction in hardness and modulus with irradiation fluence is related to amorphization [80]. Changes in physical properties have also been observed in silicate glasses. For instance, ion bombardment reduced the hardness of materials [81]. Electron irradiation first induced volume compaction at low doses; subsequently, expansion occurred at higher electron doses [82,83]. The volume compaction observed from electron irradiation is mainly related to the relaxation of the network and/or the release of alkali ions (or network modifiers: Na^+, K^+), which causes relaxation around empty spaces [83]. Continued irradiation can result in the formation of new atomic bonds, and the optimization of their structure will occur repeatedly; hence, the amorphous structure can be expanded because of the rearrangement of nonbridging oxygens–NBOs (Si-$O^{\cdot}$) to larger rings [78] or interconnects (Si-O-O-Si [82]). The release of alkali ions in the silicate network during irradiation, which results in the formation of NBOs [84], has been experimentally observed in some studies [85,86]. Furthermore, MD simulations showed the potential formation of large ring sizes up to 19 in amorphized quartz (i.e., a ring is a closed path connecting

the network of $[SiO_4]^{4-}$ tetrahedra, and its size is defined as the number of Si atoms in a given ring; in crystalline, two types of rings are 6 and 8) [65] or the formation of nanocavities after melt quenching [87]. In general, the RIVE of some amorphized minerals can continue after amorphization through the formation of large rings, and the extent of RIVE after amorphization may depend on the concentration of alkali ions in silicate minerals.

Because Young's modulus is directly dependent on interatomic bonding, whereas hardness characterizes the resistance of permanent deformations under an external load, which depends on the rigidity of the silicate network, that is controlled by coordination numbers [88] and the polymerization degree, represented by a network of $[SiO_4]^{4-}$ tetrahedra. Radiation gradually reduces the network rigidity [89], resulting in degraded physical properties. Therefore, density, stiffness, and hardness are important parameters for characterizing radiation-induced changes in amorphized silicate minerals. Although the values of some of these parameters in the amorphous state have been calculated [46] and measured [50,62,90] previously, the change after amorphization has not been reported. Therefore, it is important to demonstrate the changes in the properties of amorphized silicate minerals as a function of radiation dose for a better understanding of the relationship between RIVE and the mineral structure.

1.3.3. Current concerns on the degradation management in CBS

Degradation of CBS structure

The expected conditions at 80 years of operation in the US reactors have been evaluated [91]. The maximum irradiation of the inner CBS wall is expected to be $6.1x10^{19}$ (n/cm^2) for fast neutron and 2×10^8 Gy for gamma rays and the estimated damage layer is <20 cm from the CBS surface [5]. For Japanese PWR reactors, it

would reach to 4.7 x 10^{19} (n/cm^2) and 2.5 x 10^8 (Gy) after 60 years operation [92]. These expected neutron fluences are much higher than a recommended threshold value of 1.0 x 10^{19} (n/cm^2) for concrete degradation, which was confirmed recently [13,16]. However, the main data of neutron-irradiated concrete is limited up to 2.3x10^{19} (n/cm^2), only some data recently obtained by Maruyama et al, (2017) up to 9.2 x10^{19} (n/cm^2) for fast neutron at which strength reduction is around 50%. Therefore, it is important to clarify the main degradation during LTO. This requires solving the following issues:

(i) Though the research on the radiation-induced amorphization in silicate minerals has been intensively studied for the application of the immobilization of high-level radioactive materials [47,80,93–95], the changes in properties due to amorphization and the relationship between amorphization and RIVE are not clearly understood. There is a diversity of mineral composition of aggregates, thus it is important to identify the RIVE mechanism in model materials.

(ii) The irradiation temperature effects, which can have both positive (slowing expansion) and negative (drying) impacts on properties, are not well established. Thus, the healing effects due to temperature is needed for further studies.

(iii) Since the current neutron-irradiated data remains high uncertainty due to varying neutron spectrum and different energy cutoff, it is important to develop a correlation parameter to normalize the different neutron data.

(iv) The test samples were conducted with the free-to-expanse condition, while volume change is constrained in the matrix that could not allow an isotropic expansion. Maruyama et al, (2017) have shown an increase in strength under physical constraint. Giorla et al (2017) found RIVE under constraint is

subject to anisotropic expansion [96], thus the deformation behavior during RIVE needs to be clarified.

(v) The gradients of irradiation and temperature cause a high gradient of humidity, it can build up high internal stress and may lead to surface cracking or spalling. The gradient of irradiation field within CBS can also cause a non-uniform RIVE. It is important to estimate the damaged thickness of concrete for extended period.

Monitoring the degradation in existing concrete structure

The primary purpose of periodic inspection is to ensure that the structure still maintains enough safety margins to continue the operation of LWRs. It also aims to identify the potential environmental stressors before they cause a significant impact on the structure's integrity. Thus, non-destructive testing methods such as ultrasonic-based method (ultrasonic pulse velocity, impact-echo, laser ultrasonics), infrared thermography, electrical resistivity, resonance frequency, and others are applied to detect the average changes in properties and integrity in concrete [97]. In LWRs, the most susceptible to environmental effects is the structure for biological shielding and support for nuclear reactors, thus it should be surviving during the earthquake. if there is any degradation in the structure, it should be noticed during periodic inspection. Therefore, it is important to examine the sensitivity of non-destructive testing methods on detecting the structural change caused by the change in microstructure owing to water-loss and RIVE before they have a significant impact on concrete properties, especially when the service lifetimes are being extended. Because CBS has limited accessibility, the inspection methods utilizing ultrasonic waves could have some advantages. Though it just detects an average change in the concrete structure, it demonstrated to be feasible on the change of water content in concrete [98,99] and it seems to be related to its compressive strength [100,101].

1.4. Research objective

Based on the issues identified above, the objective of this study is to simulate and evaluate the environmental degradation effects and resultant changes in physical properties in concrete and its components considering the long-term operation. Three tasks have been set:

Task 1: Elucidate the radiation-induced volume expansion in aggregate

- To evaluate the RIVE due to ion irradiation in model materials of aggregates
- To evaluate the change in mechanical properties during RIVE, this information can be used to correlate with RIVE and as input data in the modeling code.
- To elucidate the mechanism of RIVE in different types of minerals

Task 2: Re-evaluate literature data to redefine reference level

- To develop a correlation parameter to normalize different neutron spectrums
- To propose a new reference level

Task 3: Clarify the effect of water-loss on concrete properties and examine the possibility of ultrasonic waves to monitor the existing concrete structure.

- To characterize the physicochemical change in concrete due to long-time heating
- To evaluate the sensitivity of the UPV method to detect the changes in concrete caused by water-loss and correlate UPV parameters with mechanical properties of concrete

In this thesis, **Chapter 2** briefly describes the materials and research methodology. The acceleration tests of RIVE are carried out by ion irradiation using He and Si ions at different temperatures. Acceleration test of water-loss is carried out by heat treatment (from 105^{o}C - 800^{o}C) considering capillary and bound water loss (up to 400^{o}C), and decomposition of hydration products (>400^{o}C). The methodology for

investigating the changes in microstructure using micro-scale characterization techniques, as well as for measuring physicochemical changes in concrete and its components, are briefly described.

Chapter 3 presents the results of changes in irradiated volume and associated changes in mechanical properties of quartz, albite, and microcline mineral, due to ion irradiations. This chapter clarifies and discusses the main cause of RIVE and the different mechanisms of three studied minerals. The role of mineral structure on RIVE and effects of temperature on amorphization and RIVE are also discussed.

In **chapter 4**, based on the above results, the current literature data on neutron-irradiated concrete was re-evaluated in order to determine a threshold value of maximum irradiation dose based on the RIVE effect. The current data was initially presented with neutron fluence which remains high uncertainty due to diversity of neutron spectrum and different energy cutoff, thus a correlation parameter was proposed, by which data of different neutron spectrum can be normalized into the number of knock-on displacements.

Chapter 5 presents the results of changes in concrete due to long-time heating and the possibility of ultrasonic waves to detect integrity changes due to water loss. A good correlation between ultrasonic parameters and Young's modulus is obtained, suggesting ultrasonic waves can be used to monitor concrete degradation.

The **last chapter** summarizes the principal findings and suggestions for future works for concrete degradation issues.

CHAPTER 2: MATERIALS AND METHODOLOGY

It has been identified that the degradation in concrete evolve from micro-scale change due to RIVE and drying (i.e., water loss) to structural change such as dimension change due to formation of cracks and volume expansion of aggregates. This chapter describes the research methodology, which is composed of two parts:

(1) describing the selection of model materials for studying RIVE mechanism; detail experimental setup using ion irradiation as well as well-controlling irradiation parameters, and utilization of advanced microstructure characterization techniques using FIB/TEM and in-situ TEM; and

(2) measurement of physicochemical changes and structural changes using ultrasonic waves for studying the effect of water loss; and establishment of a correlation between ultrasonic velocity and mechanical properties for the application on the inspection of the existing concrete structure.

2.1. Acceleration test and characterization of radiation-induced amorphization related degradation

2.1.1. Utilization of ion irradiation to simulate neutron

To elucidate the deterioration mechanism that contributes to the aging countermeasure against concrete irradiation deterioration due to neutron, ion irradiation was performed to identify the amorphization process and extract the RIVE mechanism.

Compared with neutron, irradiation using high energy ions emphasizes several advantages such as low cost, high dose rate, and negligible sample activation, and easy to control conditions, as a summary in Table 2- 1. In addition to that, the benefits of using ion irradiation are:

- The interaction energy between charged particles and target material can be controlled.
- The shape of the beam can be controlled by a magnetic lens system or a scanning system using an electromagnetic field. This makes it possible to easily control the irradiation area and dose rate.
- Since there are few restrictions on the irradiation chamber, it is possible to precisely control the temperature and atmosphere of the sample.

As neutron interaction is mainly caused by nuclear collision, about half of the energy of incident ions is consumed by electronic excitation, and the rest is nuclear collision (e.g., in case using 3MeV Si irradiation). The effect of electron excitation has a maximum value on the outermost surface of the sample and gradually decreases along the depth direction. In contrast, the effect of nuclear collision is small near the surface of the sample and shows a steep peak near the maximum ion penetration depth. As a result, the amount and nature of the irradiation effect change depending on the depth, so it is necessary to devise an index of the cumulative dose.

Table 2- 1. Advantage and disadvantage of neutron and charged particle irradiation

Neutrons	Charged particles (ions, electron)
Advantage	
• Homogenous damage distribution • Actual irradiation damage • Bulk properties (compressive and tensile test, fracture test)	• Not radioactive • Easy to control irradiation parameter • Possible to simulate the individual mechanism • High dose in a short time
Disadvantage	
• Long irradiation time • Expensive • Difficult to control irradiation parameters • Radioactive sample	• Inhomogeneous damage profile • Very small penetration (few μm), thus small size samples • The issue to correlate with bulk properties

2.1.2. Selection of model materials of aggregate

Since silicate minerals have the highest RIVE, the main minerals containing in the silicate-bearing aggregate are chosen as a surrogate model for RIVE behavior. Three tectosilicate minerals (i.e., the three-dimensional framework of silicate tetrahedra $[SiO_4]^{4-}$) including a Z-cut quartz crystal (SiO_2 (0001) oriented) and two feldspars, i.e., natural albite ($NaAlSi_3O_8$) and natural microcline ($KAlSi_3O_8$) were studied. The mineral structure of these minerals is obtained from [62] and visualized by VESTA software [102] as seen in Fig.2- 1. The sample size is approximately 5 mm × 10 mm × 0.5 mm. Natural feldspar minerals are polycrystalline, and the size of grains is approximately 10^{-5}~10^{-4} m in diameter. The presence of SiO_2 grains in feldspars was confirmed by X-ray diffraction (XRD) and characteristic X-ray spectroscopy with a scanning electron microscope (SEM-EPMA).

Preliminary experiments revealed that the feldspar samples were easily cleaved, thus

the sample has adhered to the aluminum substrate with a heat-resistant adhesive and the aluminum substrate was handled. The thickness of the aluminum plate was about 0.5 mm, and both sides were polished in advance to improve smoothness and improve heat conduction. The substrate thickness was changed according to the thickness of the test material body to be bonded, and the total thickness of the sample body was adjusted to be almost the same in all experiments.

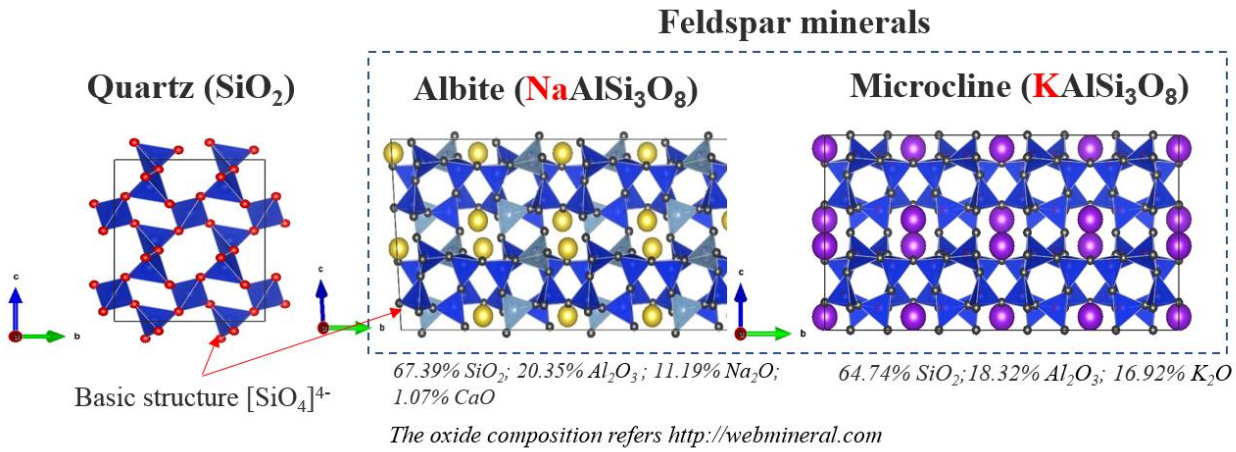

Fig.2- 1. Crystal structure of three tectosilicate minerals as visualized by VESTA

2.1.3. Irradiation conditions

The minerals were collected, cut, and polished at Nagoya University, then irradiated with 2 MeV He^{2+} ion at the Nagaoka University of Technology and 3 MeV Si^{2+} ion at the High Fluence Irradiation Facility (HIT) at the University of Tokyo (Fig.2- 2). The detail of the irradiation condition is shown in Table 2- 2.

In the 3 MeV Si^{2+} ion irradiation condition, the electron excitation is not evident so that the RIVE was ruled by the knocking-on reaction. The ion range and displacement damage were estimated using SRIM-2013 [103], as shown in Fig.2- 3. The range of 3 MeV Si ions in quartz, albite, and microcline was estimated to be 2.24, 2.25, and 2.38 micrometers, respectively. Though the “displacement damage” for amorphizing and expanding material cannot be defined easily, the displacement

damage in three materials is in the similar level. The average dose rates at irradiated regions were estimated to be 3.15×10^{-4}, 3.12×10^{-4}, and 3.23×10^{-4} dpa/s for the quartz, albite, and microcline, respectively, assuming the displacement threshold energy E_d of all the atoms to be 25 eV. It should be noted that there are various reported values for the E_d of silicon and oxygen in silicate tetrahedra [104],[67], and it is known that there is some anisotropy [67]. In addition to the poorly information of E_d of alkali metals in feldspars (Na^+ and K^+), the formation of secondary defect structures due to the displaced alkali metals should be considered. For this reason, we compared the RIVE behavior between three different minerals as a function of fluence.

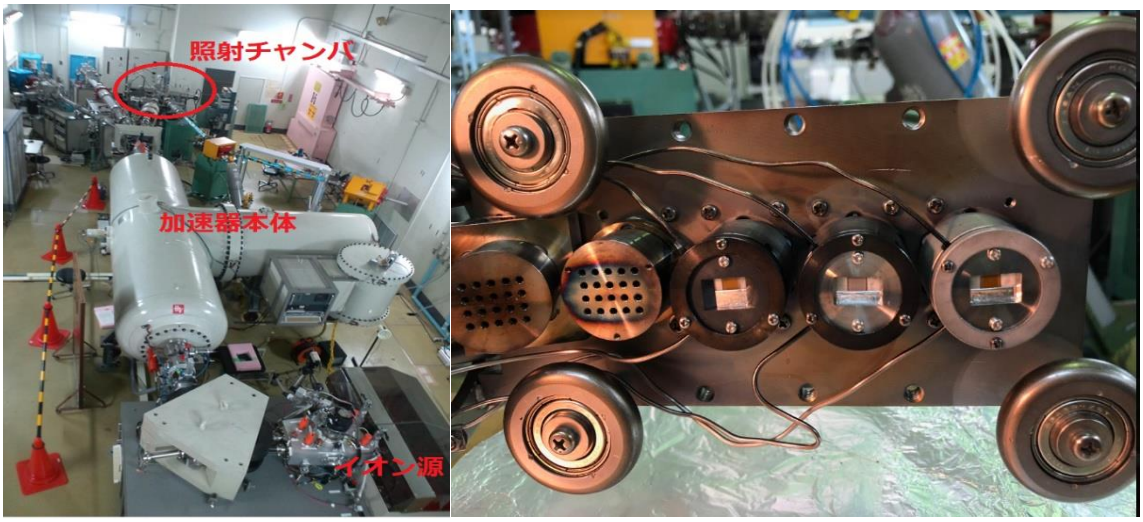

Fig.2- 2. Ion irradiation on Tandem accelerator (left) and sample holder for high-temperature irradiation (right)

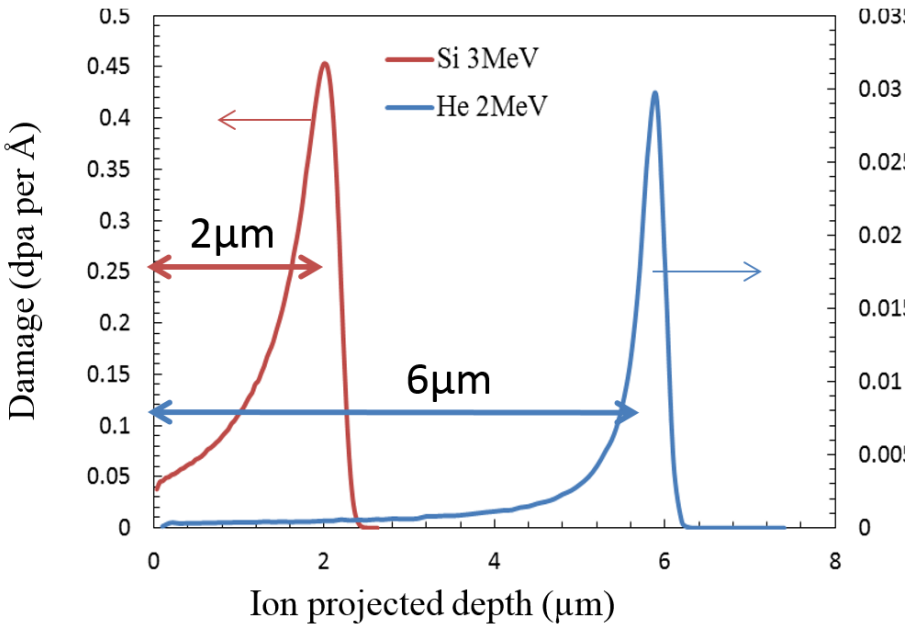

Fig.2- 3. The representative damage profile due to ion irradiation in quartz by SRIM 2013 simulation

2.1.4. Controlling the substrate temperature during ion irradiation

The irradiation temperature is controlled by thermocouples inserted in the heating block (Fig.2- 4). However, the temperature of the sample surface is different from the set temperature because of heat radiation from the surface and heat input by the ion beam. For this reason, the sample surface temperature is measured with an infrared camera, and the emissivity and transmittance are calibrated before irradiation. The measured value with the infrared camera is used as the sample temperature. A preliminary test showed the irradiation with 3 MeV Si^{2+} ions increased surface temperature by about 6°C, 9°C, and 14°C from the initial setting of 25°C, 100°C, and 150°C in the heating block, respectively. Therefore, the setting of temperature of the heating block was adjusted from 10 to 20°C lower than the set temperature, except in the case of room temperature irradiation, and starting the ion irradiation. During irradiation, the surface temperature was frequently monitored by the infrared camera. Fig.2- 5 shows the monitor of sample surface temperature using

an infrared camera during irradiation. The temperature of the sample surface during 3 MeV Si^{2+} ions was 44 ± 4 °C, 92 ± 5 °C, and 142 ± 3 °C.

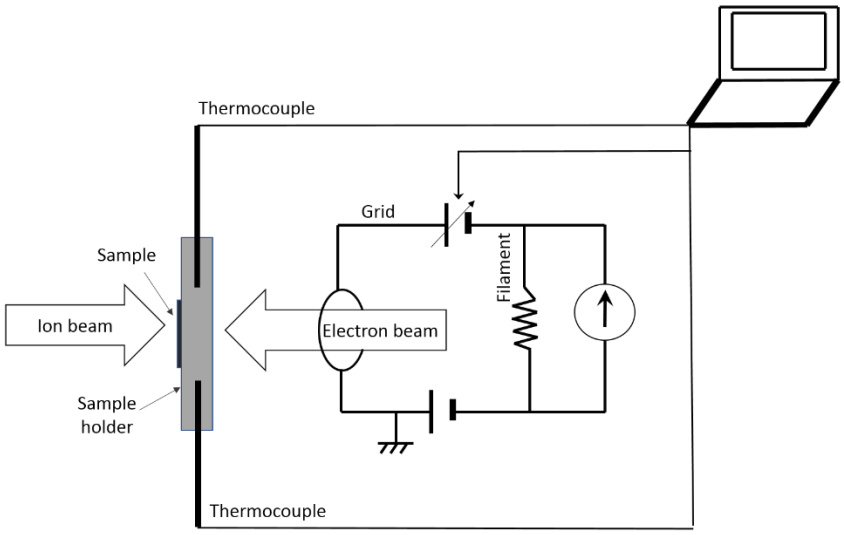

Fig.2- 4. Schematic diagram of heating block

Fig.2- 5. The irradiation temperature is monitored using an infrared camera

Table 2- 2. Irradiation conditions in Tandem Accelerators

Ions	Energy (keV)	Nuclear energy loss dE/dx (keV/nm)	Range R (nm)	Flux (ions/cm^2.s)	dpa per ion	Ave. damage rate (dpa/s)	Temp. (^{o}C)
He	2000	0.3	6028	6.5×10^{11} ~ 6.4×10^{12}	180	3.8×10^{-6}	RT
Si	3000	1.3	2236	1.5×10^{12}	4137	3.5×10^{-4}	44, 92, 142

2.1.5. Post irradiation measurement and analysis

Step height measurement

For evaluating the RIVE, about half of the polished surfaces were covered by aluminum foil during irradiation to create the irradiated and unirradiated regions. Step heights of irradiated part were measured using both laser microscopy (Fig.2-6.) and profilometer (Dektak 6M) at intervals of about 50 μm along the border, with accuracies of about 1nm and 5nm, respectively. Out-of-plane swelling is the integral strain induced by irradiation damages along with ion range including in-plane strain in the lattice due to the accumulation of defects and out-of-plane strain as a result of the relaxation of amorphous regions. In this study, step height measurement techniques can only measure the out-of-plane swelling with a step height of several nanometres, as illustrated in Fig.2- 7.

Because the irradiated region was extremely small in comparison with the sample thickness (~0.5 mm), it was difficult to directly measure the density change using traditional techniques. Alternatively, several researchers have estimated the density

change induced by ions (ρ/ρ_0) based on step height measurements between unirradiated and irradiated regions [105–108]. This method was applied in this study using both laser microscopy (Keyence - VK9100) and profilometry (Dektak 6M). The density change can be calculated as

$$\boldsymbol{\rho/\rho_0 \approx \frac{1/(R+\Delta H)}{1/R}} \quad \text{Eq.2- 1}$$

where ΔH is the step height, and R is the ion range determined by an SRIM code.

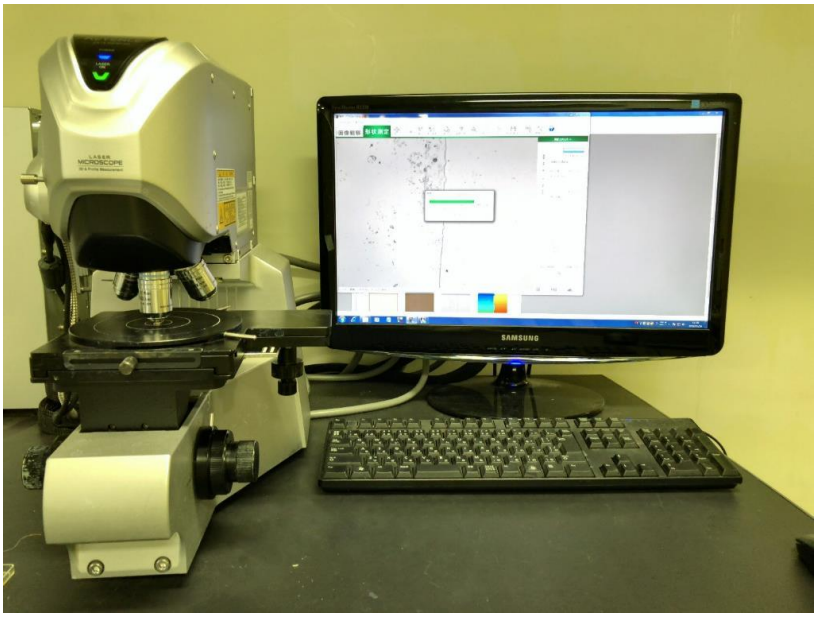

Fig.2- 6. Step measurement using Laser Microscope

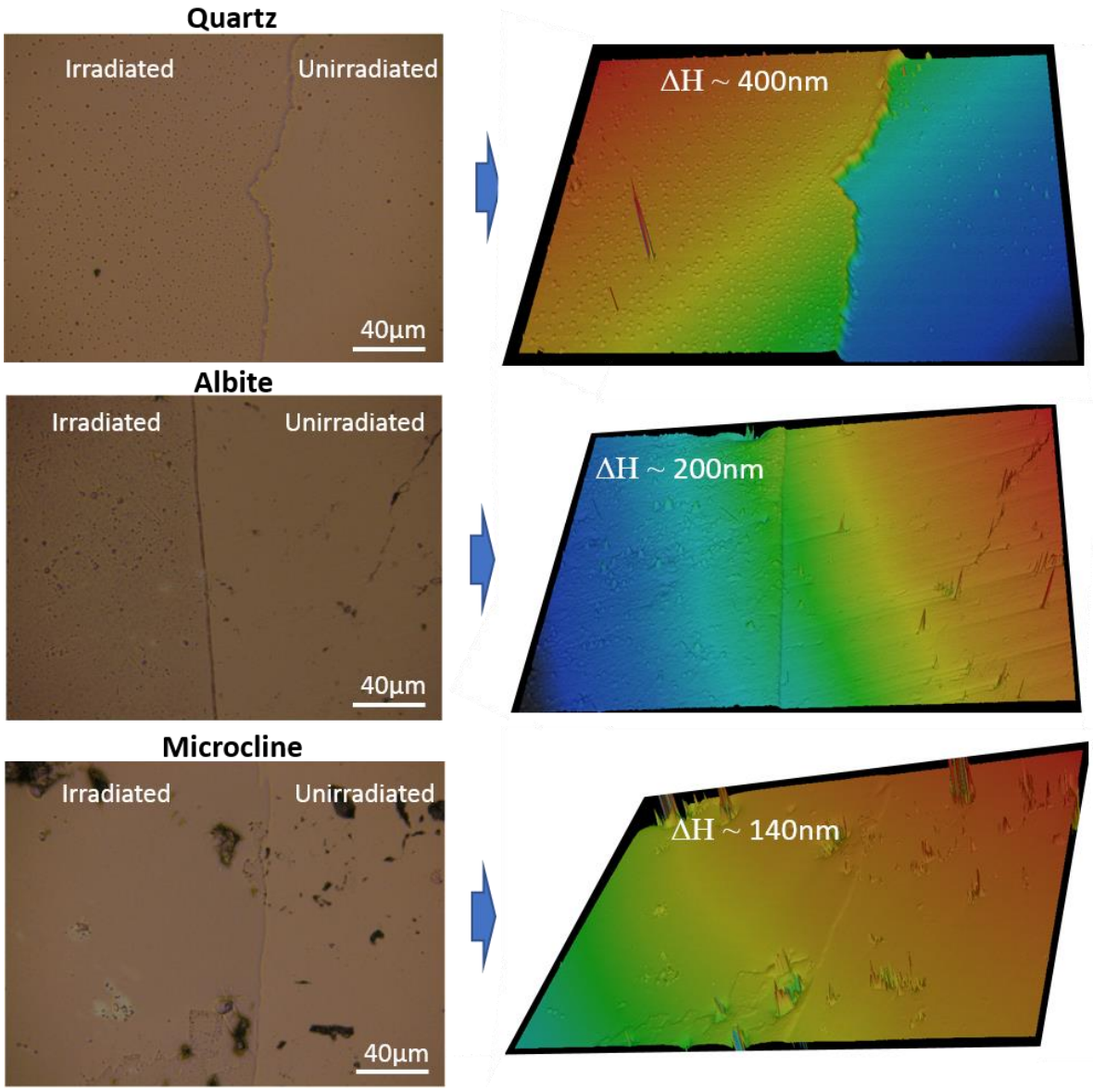

Fig.2- 7. The representative of step height measurements using Laser Microscopy

Microstructure observation by TEM

TEM observation was performed using 200 kV transmission electron microscope (TEM) in JEOL JEM-2000FX and 100 kV in Hitachi HT7700 to confirm the amorphized region and detail microstructure. Since the damaged area due to ion irradiation is limited to the sample surface (few micrometers), the samples of 3 x 10 x 20 µm are lifted out to a TEM mesh on a semicircle with a focused ion beam (FIB),

and then polishing using 40keV Argon beam down to approximately 100 nanometers in thickness, as seen in Fig.2- 8. Since the irradiation damage also occurs due to the processing by FIB, the optimization of the processing conditions was performed. The FIB used in this project was the Hitachi High-Tech FB2200.

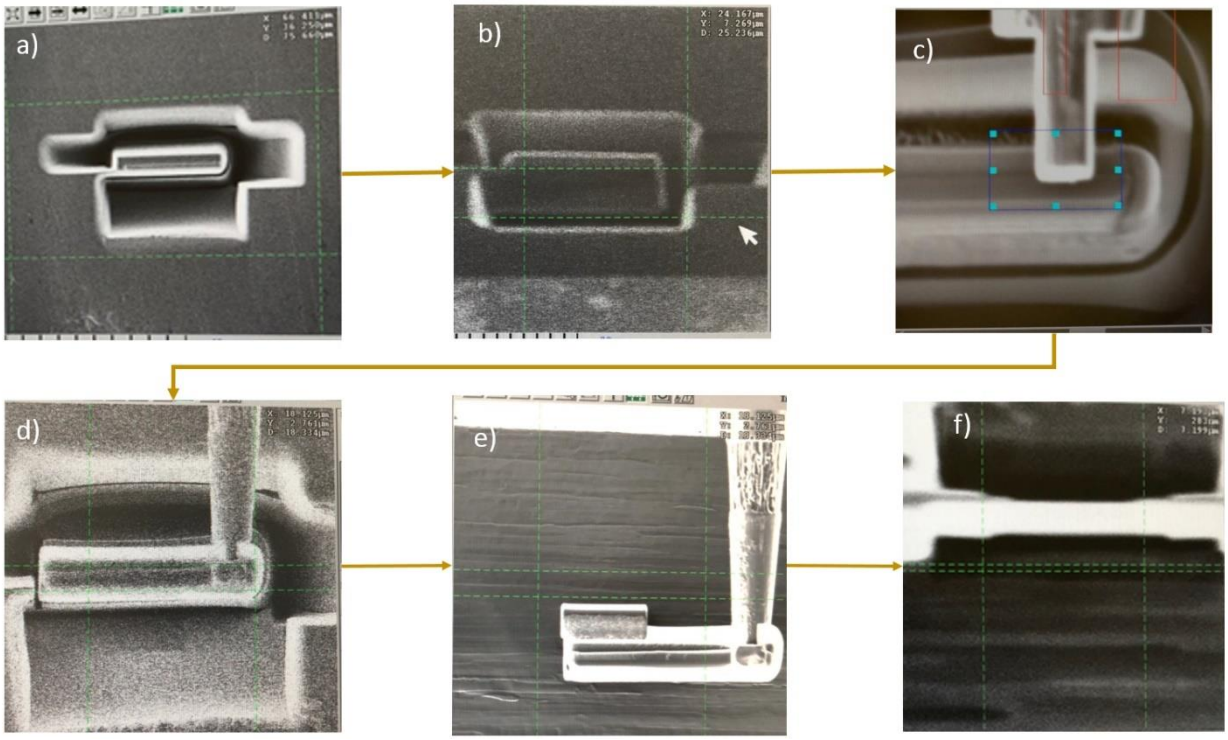

Fig.2- 8. Thin sample preparation by FIB: a) Sputtering around the coated sample surface; b) title 60^{o} and cut the bottom of sample; c) Insert the probe and weld the probe with sample; d) Lifting out the sample; e) lift-out and weld the sample to the TEM mesh; f) two steps: rough polishing using 40keV Argon down to approximately 100 - 150nm in thickness, and then final cleaning using 5keV Argon to remove the damaged layer from rough polishing.

Nano-indentation test

Instrumented indentation test was performed in a nanoindentation machine (Shimadzu, DUH-211) using a Berkovich tip, which can control the minimum load and displacement increment to 0.196 μN and 0.1 nm, respectively. The hardness and Young's modulus were calculated according to the Oliver and Pharr methods [109]

with a corrected indentation tip roundness. To determine Young's modulus, the Poisson's ratio of the irradiated specimens must be determined. However, this information is not available in the literature. Le Pape et al. [75] suggested that the Poisson's ratio of irradiated quartz changes as a function of RIVE, as follows:

$$\boldsymbol{\nu^* = \min(\nu_0 + \exp(0.0063(\varepsilon^*)^{1.938}) - 1; \nu_s^*)}, \quad \textit{Eq.2- 2}$$

where ν^* and ε^* are the irradiated states of the respective Poisson's ratio and quartz expansion (%); $\nu_0 = 0.08$ and $\nu_s^* = 0.21$ for the crystal and amorphized states, respectively. The function was applied in this study to determine the "irradiated" Young's modulus of quartz. For albite and microcline, ν was assumed constant (ν = 0.28) during irradiation based on a previous MD study for albite [46]. By estimating the range of error for ν to be from 0.08 to 0.3, the calculated Young's modulus was scattered by less than 7%; hence, the change in the Poisson's ratio was insensitive to the determination of the elastic properties.

For most cases, 20 mN was applied in both the irradiated and unirradiated parts. The indentation depths were distributed around 0.4 micrometers and the results reflected the characteristics of a single irradiated grain. When a large number of random measurements were made on natural minerals, the results showed a clear binomial distribution, reflecting the characteristics of feldspar grains and silica grains. The indentation properties and microstructure of feldspars presented in this study were obtained from the feldspar region, based on the results of surface observations. The test was conducted in a load-control mode, with a loading rate of 13 mN/s; it was maintained for 5 s and then unloaded at the same speed. The average value from at least 20 points was obtained. Fig.2- 9 shows a typical measurement of indentation test at unirradiated and irradiated regions.

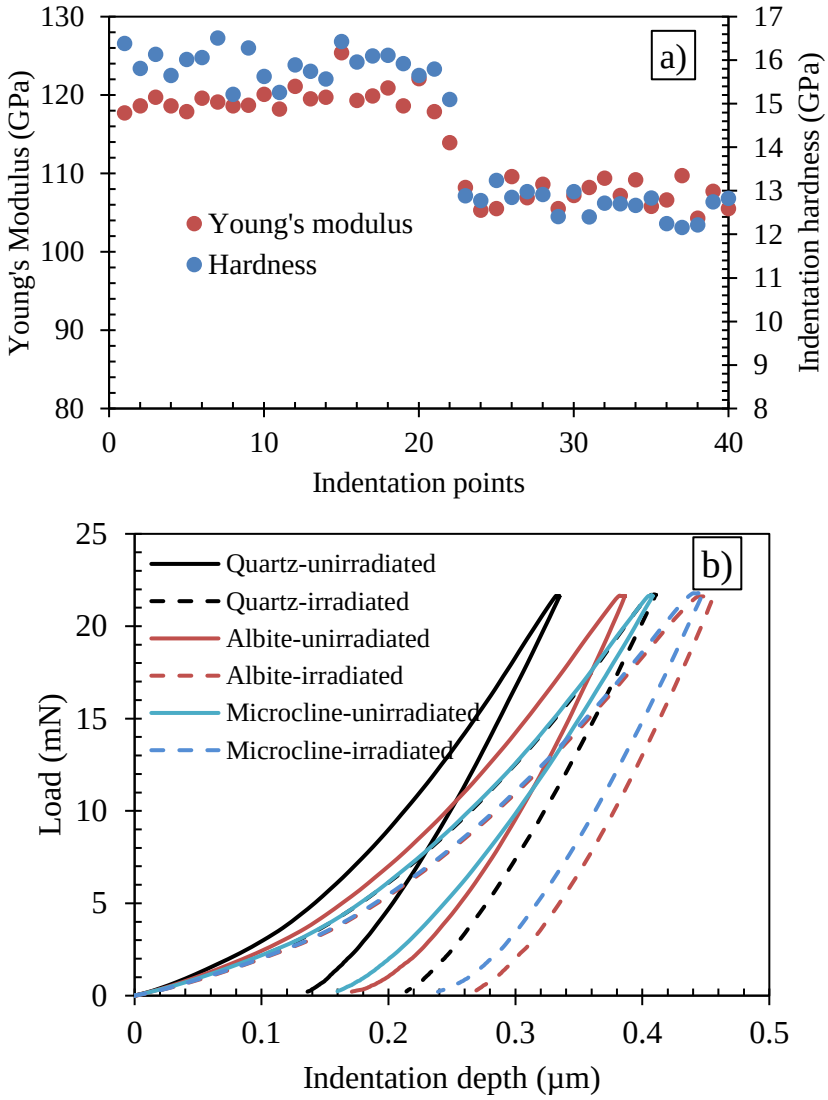

Fig.2- 9. Representative nanoindentation test at the boundary between irradiated and unirradiated quartz (a) and representative load-displacement curves for felspar mineral at 20mN (b)

Electron spin resonance (ESR) after annealing test

ESR method is used to quantify the paramagnetic defect centers (i.e., the existence of unpair electrons) in irradiated quartz and silica samples. The ESR measurements were performed on a commercial ESR spectrometer (JEOL JES-RE2X), where the field modulation was 0.32mT with a frequency of 100kHz and a microwave power of 5mW at room temperature for all measurements. The other setting parameters

were also kept the same including a microwave frequency of 9.09 GHz, the gain of 63dB, the time constant of 0.1seconds, sweep time of 1min, and spectral resolution (i.e., 0.007326mT/point). At least three measurements were conducted for each condition. For accurate determining the Lande vector (i.e., g factor used to index the defect centers, g = 2.0023 for electron), a reference sample of Mn^{2+} is inserted inside the sample cavity. Table 2-3 provides the information of samples (only irradiated quartz) and annealing conditions. The annealing tests were conducted in vacuum heating and ESR signals were recorded after each heating step.

Table 2- 3. The irradiated samples and annealing test for ESR measurement

Sample name (only quartz)	**Irradiation history**		**Annealing test**		
	Ion fluence (ion/cm^2)	Temperature	Type	Temperature (^{o}C)	Duration (mins)
Si-irradiated sample	2.0x10^{16}	RT	Isochronal	100 - 500	60
He-irradiated sample 2	2.2 x10^{15}	RT	Isochronal	100 - 500	60
He-irradiated sample 4	3.2 x10^{16}	RT	Isochronal	100 - 500	60
He-irradiated glass	3.6 x10^{15}	RT	Isochronal	100 - 500	60
He-irradiated sample 1	3.1 x10^{15}	RT	Isothermal	150 and 200	
He-irradiated sample 3	5.8 x10^{15}	RT	Isothermal	150 and 300	

2.2. Acceleration test and characterization of water-loss related degradation

2.2.1. Preparation of concrete

The cylindrical concrete samples with a size of φ100mm x 200mm were prepared. The concrete mixture proportions per cubic meter were 157kg of water, 285 kg of

sand, 838kg of coarse aggregate with a water/cement ratio of 0.55. The admixture of 1% was also added to increase the homogeneity of concrete microstructure. The concrete was cured for 28 days before subjected to the heat-treatment process.

2.2.2. Heat treatment

Total of 18 specimens (each temperature three samples) was heated. In order to simulate the water loss due to high-temperature conditions, the specimens were heated with different durations with slow heating and cooling rate to generally make a uniform change in the concrete and prevent large thermal gradients. Heating and cooling of the heated samples were carried out in the electric furnace. The temperature of sample was controlled by measuring the temperature of furnace and the temperature of the sample core. The detail of heat treatment conditions is given in Table 2- 4.

Table 2- 4. Summary of heat treatment process

Target temp. (°C)	Monitoring location	Heating rate (°C /min)	Cooling rate (°C /min)	Holding time (hours)
105	Furnace temp.	0.9	0.11	504 (21 days)
	Sample core	0.48	0.12	
200	Furnace temp.	0.92	0.31	336 (14days)
	Sample core	0.48	0.28	
400	Furnace temp.	0.65	0.68	24 (1days)
	Sample core	0.64	0.71	
600	Furnace temp.	0.64	0.69	16
	Sample core	0.63	0.69	
700	Furnace temp.	0.71	0.77	16
	Sample core	0.68	0.72	
800	Furnace temp.	0.73	0.80	6
	Sample core	0.73	0.79	

After the heat treatment and cooling process (Fig.2- 10), the specimens were taken to ultrasonic pulse velocity test to measure the changes of pulse velocity with exposure temperature. Subsequently, the specimens were taken to the compressive test to measure the residual compressive strength and static elastic modulus. After mechanical test, the broken pieces from concrete samples were collected and stored in desiccator for further tests (XRD, TG/DTA, and SEM). For evaluating the changes in pore structures, Mercury porosimetry tests were conducted in samples cut from the center of concrete cylinders. The following paragraphs give the details of measurement and analysis.

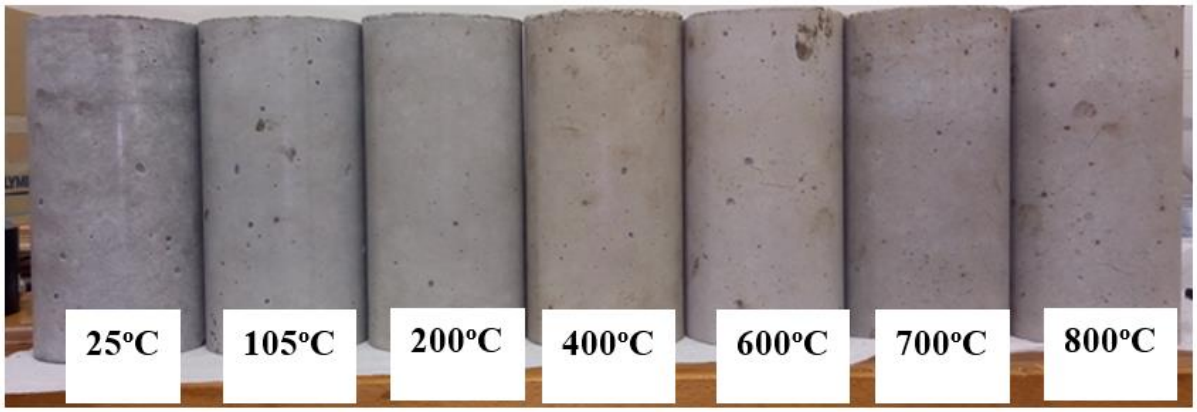

Fig.2- 10. The appearance of concrete after heat treatment

2.2.3. Mechanical test

The mechanical test is commonly used to measure the compressive strength and static elastic modulus. The tests were carried out on a hydraulic universal testing machine according to Japanese Standard JIS A 1149-2001 "*Method of Test for Static Modulus of Elasticity of Concrete*". When the stress-strain curve is obtained, Young's modulus, E_s can be calculated as:

$$\boldsymbol{E_s = \frac{S_1 - S_2}{\varepsilon_1 - \varepsilon_2} 10^{-3}} \quad \text{.....Eq.2- 3}$$

where S_1 = 1/3S_{max}, is the compressive stress; ε_1 is the strain which estimated at S_1

S_2 is estimated at strain $50x10^{-6}$; ε_2 = $50x10^{-6}$

2.2.4. Ultrasonic pulse velocity test (UPV)

The experimental setup is a simple through-transmission ultrasonic configuration. It consists of a waveform generator (OLYMPUS 5077PR), two transducers, a pre-amp, and a data acquisition system (TEKTRONIX DPO2022B). UPV measurements carried out on the heated concrete using both longitudinal P-wave transducer with a diameter 50mm and shear S-wave transducer with a diameter 25mm. Both transducers have a center frequency of 100 kHz. The arrangement of both transducers and the specimens in the experiment is shown in Fig.2- 11.

When the transmission time between sending and receiving transducers are estimated (Fig.2- 12), the pulse velocity will be calculated as:

$$\boldsymbol{V_p} = \frac{\boldsymbol{L}}{\boldsymbol{\Delta t}} \quad \text{.....Eq.2- 4}$$

where L is the length of the sample (200mm) and Δt is the transmission time or the time delay between sending transducer and receiving transducer.

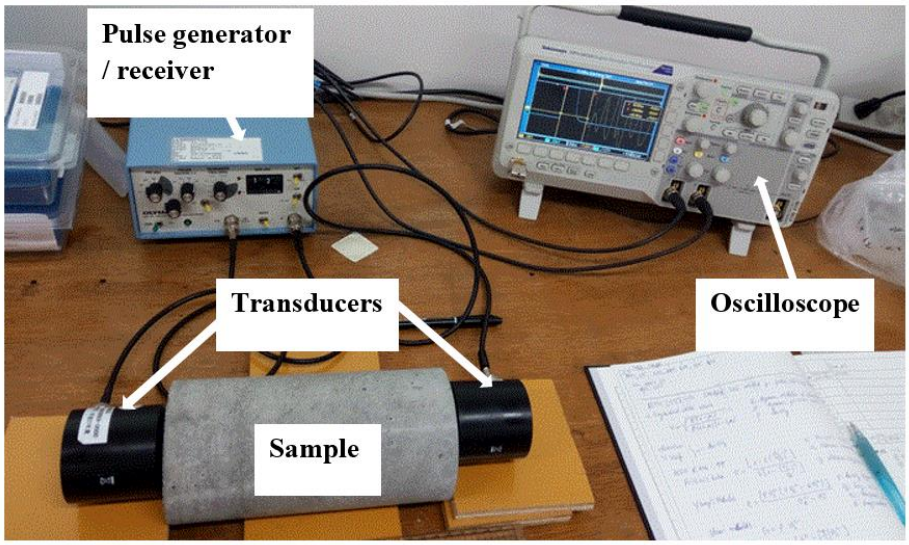

Fig.2- 11. Experimental setup for ultrasonic pulse velocity test

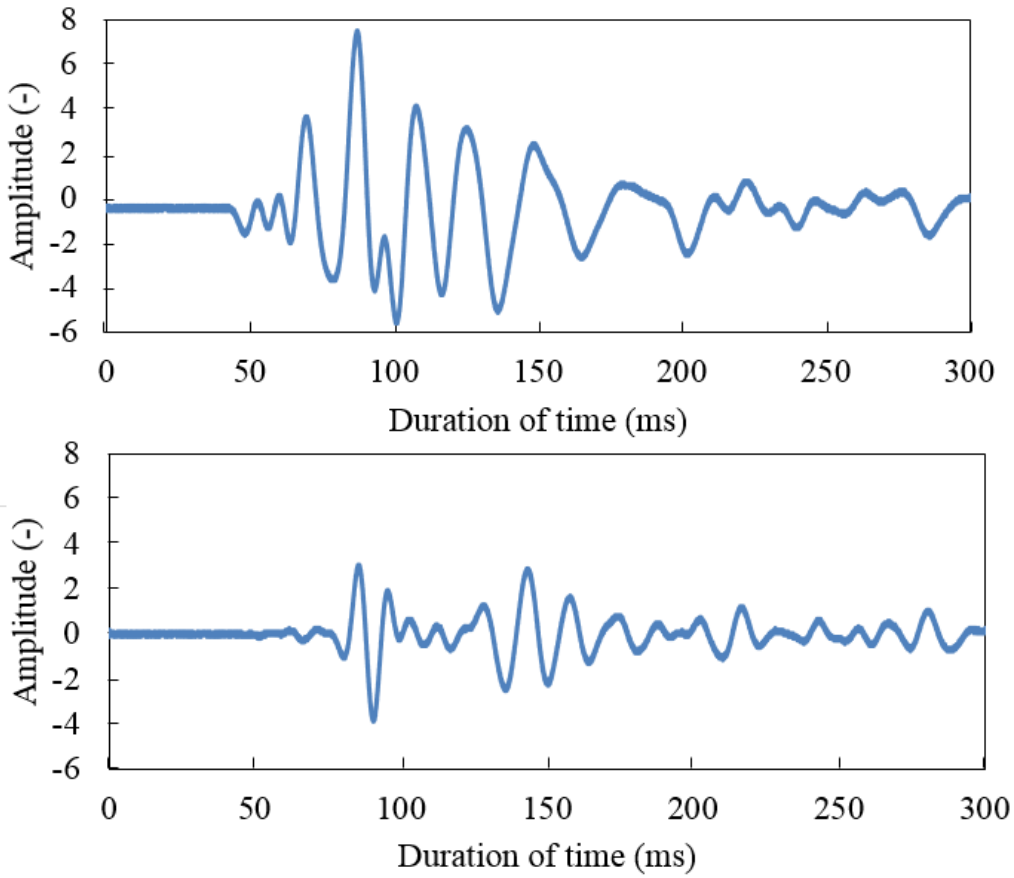

Fig.2- 12. Estimating the transmission time between sending and receiving transducers (upper signal is P-wave, lower signal is S-wave)

2.2.5. Characterization of microstructure changes

X-ray diffraction (XRD)

The samples to be analyzed were collected from the crushed specimens from mechanical test. The materials were ground into powder to make a homogeneous composition. XRD tests were conducted on Rigaku's X-ray diffractometer Miniflex 600 with CuKα radiation (λ=1.54056Å), data were collected in the range 17 to 80° in 2θ, operating in 40KV and 15mA.

Thermogravimetric analysis (TG/DTA)

Thermogravimetric analysis was performed using SETSYS Evolution TG/DTA/8/W. The initial mass of about 57.6 mg used for the tests was weighted using a balance with ±0.1 mg of accuracy. The tests were performed under an argon flow of 100 $mL.min^{-1}$. The heating rate was set at 10°C/min until reaching 800°C.

Mercury porosimetry (MIP)

The MIP test (Fig.2- 13) was conducted using the AutoPoreIV 9520. The maximum pressure of the porosimeter is 210 MPa, covering the pore diameter range from about 0.003 to 360 μm. For the sample preparation, disked pieces of about 10mm thickness were cut out from the center of cylindrical concrete φ100-200mm using a diamond cutter and then being immersed in acetone for 1 day to stop the hydration. After that, the mortar part of about 5mm square was removed from the pieces and dried for one week in a freeze dryer until MIP test. The pore diameter was determined by Washburn's equation [110]:

$$\mathbf{d} = \frac{-4\gamma cos\theta}{P} \quad \text{.....Eq.2- 5}$$

where, d is the pore diameter, γ is the surface tension = 0.484 N/m, θ is intruded contact angle = 130° (cos θ = -0.643), P is the pressure of mercury (MPa).

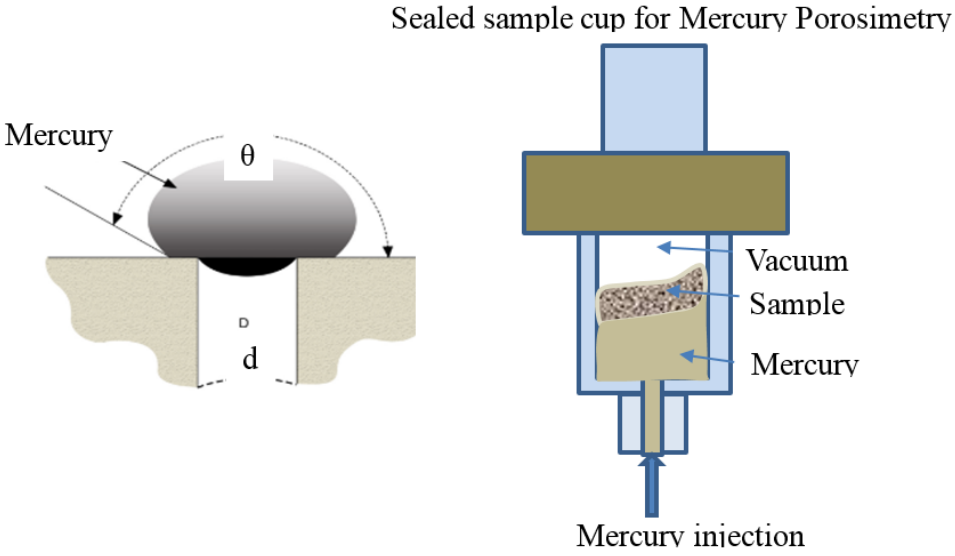

Fig.2- 13. Device for MIP test

Scanning Electron Microscopy (SEM)

The samples for SEM analysis were collected from crushed pieces from mechanical tests. To maintain the microstructure during sample preparation, the samples were impregnated in fresh epoxy resin. Afterward, the samples were finely ground on the lap wheel with various sandpapers. The polishing was done with 3, 1, and 0.25µm diamond paste.

Before SEM, the polished surfaces were coated with a thin gold layer to dissipate excess charge from the specimen. The images of SEM were captured on EPMA 7600 using a backscattering detector at magnification 500x with a low acceleration voltage of 15kV and 10nA.

CHAPTER 3: RADIATION-INDUCED VOLUME EXPANSION (RIVE) IN MODEL MATERIALS OF AGGREGATE

3.1. Introduction

Amorphization and radiation damage in silicate minerals are important research topics in many areas, such as electronic devices, optical applications [44,111], and nuclear waste immobilization [80,94,112]. Recently, many studies have been performed regarding the plant life management and long-term performance of nonreplaceable components in aging nuclear power plants, such as concrete structures [5,12,16]. The RIVE of aggregate minerals is considered the primary cause of long-term degradation in concrete structures, and it is controlled by the amorphization*;* however, the RIVE mechanism is not fully understood because the correlation between amorphization and RIVE was not established. Recently, Krishnan et al. [78] published a comprehensive study based on molecular dynamic (MD) simulations, which showed that the change in density and stiffness during irradiation-induced amorphization (amorphized) in many types of silicate minerals was similar to that of thermally induced vitrification, and suggested the use of isochemical glasses to predict upper limit changes in density and elastic modulus under irradiation [78]; nevertheless, the amorphized structure is difficult to be estimated and the mineral structure may affect the RIVE behavior.

Since it is impossible to test in advance for all environmental conditions, this chapter discusses the effects of environmental factors (temperature and flux) on the RIVE behavior and clarifies the RIVE mechanism caused by both ionization and knock-on displacement in the LWR's conditions, as well as mineral structure effects on the RIVE of rock-forming minerals. The research methodology for extracting the RIVE mechanism is described in Fig.3- 1.

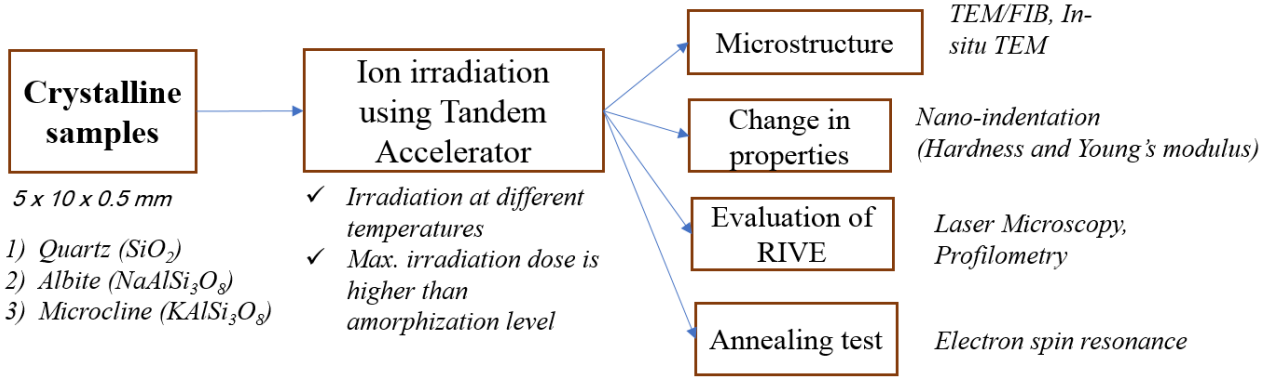

Fig.3- 1. Research methodology to extract RIVE behavior

3.2. Results

3.2.1. Step measurement

He irradiation

By 2 MeV He^{2+} irradiation, the damage profile is steep and concentrated near the end of range at around 6μm depth based on SRIM simulation, at which the end-of-range amorphization occurs. Fig.3- 2 shows the ion fluence dependence of step height with different ion fluxes. Results indicated no significant ion flux effect on the onset of swelling was observed. This may be due to small flux variation. The different fluxes caused some scatters of step height values at an early stage of swelling. The out-of-plane swelling initiated at the ion fluence $1x10^{15}$ (ions/cm^2) and it did not approach saturation at around $3.2x10^{16}$ (ions/cm^2).

Si irradiation

Irradiated quartz

In the case of 3 MeV Si^{2+} irradiation, the maximum step height was about 450 nm, as presented in Fig.3- 3. The shape of irradiated and unirradiated parts was almost flat and clear steps appeared at the boundary between the irradiated and the unirradiated part after irradiation. The results indicated the characteristic of step height showed different behavior at elevated temperatures. In other words, temperature enhanced out-of-plane swelling. In the case of 2 x 10^{14} cm^{-2}, the rate of swelling was lower and step height did not reach saturation at 142°C. In contrast, the sample with dose 1 x 10^{15} cm^{-2} nearly reached saturation with approximately 400 nm at 142°C. Beyond 6 x 10^{15} cm^{-2}, the step height was almost unchanged. It noted that the temperature had an insignificant effect on the value of swelling saturation. This confirmed the previous results in neutron-irradiated quartz [48,113]. Comparing at all temperatures, the step heights at 2 x 10^{16} cm^{-2} were slightly reduced compared with the case of 6 x 10^{15} cm^{-2}. In other words, the structural relaxation continued to change even after saturation of swelling.

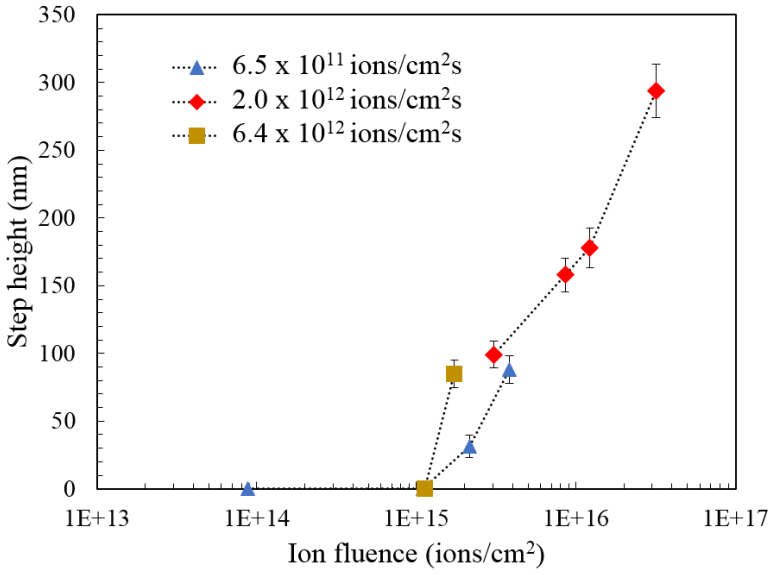

Fig.3- 2. The ion fluence dependence of step height with different ion fluxes at room temperature induced by 2 MeV He^{2+} irradiation.

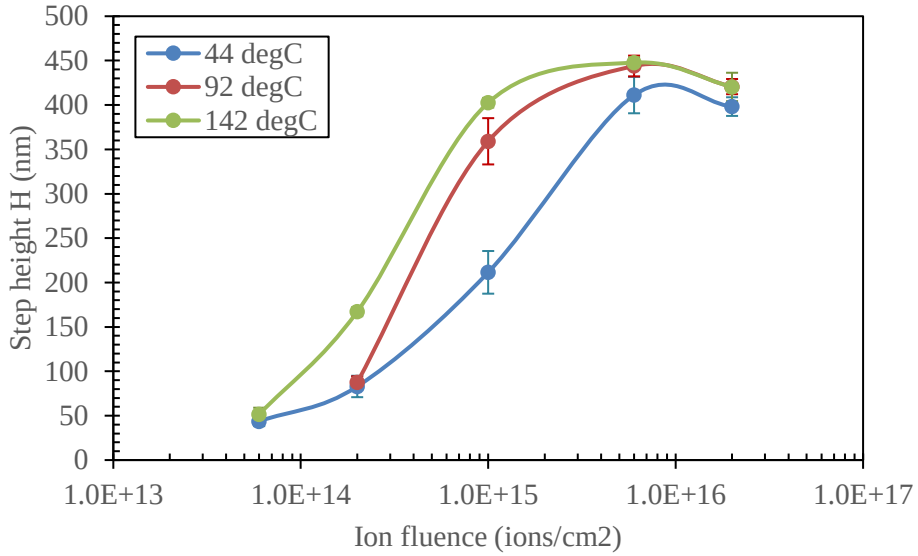

Fig.3- 3. The effects of temperature on out-of-plane swelling in quartz induced by 3 MeV Si^{2+} irradiation with ion flux 1.5 x 10^{12} ions/cm^2.s.

It is known that quartz undergoes anisotropy expansion under neutron irradiation, i.e., the lattice change along the a-axis is about twice as important as lattice change along c-axis [53,73,114]. However, our results appear to be in contradiction with previous neutron-irradiated data. In ion irradiation, the irradiated layer is thin (a few µm) and the region is constrained by the surrounding crystalline matrix, thus the volume change may occur primarily perpendicular to the surface. Given the step height of 300 nm in helium irradiation, it is about 5% swelling of the irradiated layer, while in the case of silicon irradiation, that is about 18%! Thus, swelling towards the open volume, that is along the c-axis in this study, was found to be more severe than the swelling along the favorable orientation when the irradiation region has been constrained by surrounding undamaged substrate.

Irradiated feldspar

At room temperature: The changes in step height and ion fluence exhibited similar tendencies with the case of quartz. The steps also saturated at approximately 6 × 10^{15}

cm^{-2} in three minerals. The maximum steps were ~206 nm in albite and ~ 138 nm in microcline. The shapes of the irradiated and unirradiated parts were flat and appeared as clear steps; this suggests that swelling almost occurred in one direction toward the surface. It is noteworthy that the expansion behavior of quartz crystals in natural minerals (mainly albite and microcline) was broadly consistent with a Z-cut quartz crystal. Thus, the difference in crystal orientation may not significantly affect the open-space swelling.

At 92ºC and 142ºC: A higher temperature generally enhances the rate of RIVE. Nevertheless, at 92ºC the RIVE in feldspars seems to be lower than RIVE at RT (Fig.3- 4 and Fig.3- 5.), this shows a different behavior of RIVE between quartz and feldspars at elevated temperature. In addition to that, temperature changes the saturation value of RIVE, while it does not affect the case of quartz. This suggests a different mechanism of structural relaxation and RIVE between quartz and feldspar. This point will be discussed in Section 3.3.3.

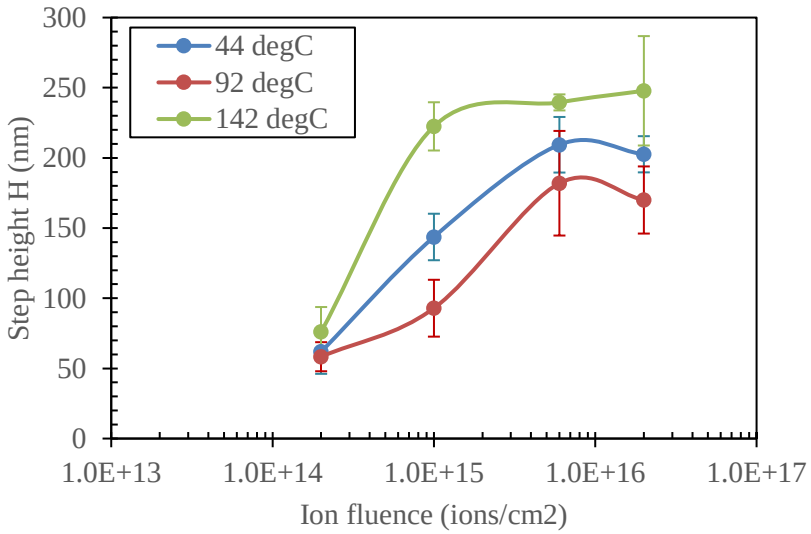

Fig.3- 4. The effects of temperature on out-of-plane swelling in albite induced by 3 MeV Si^{2+} irradiation with ion flux 1.5 x 10^{12} ions/cm^2.s .

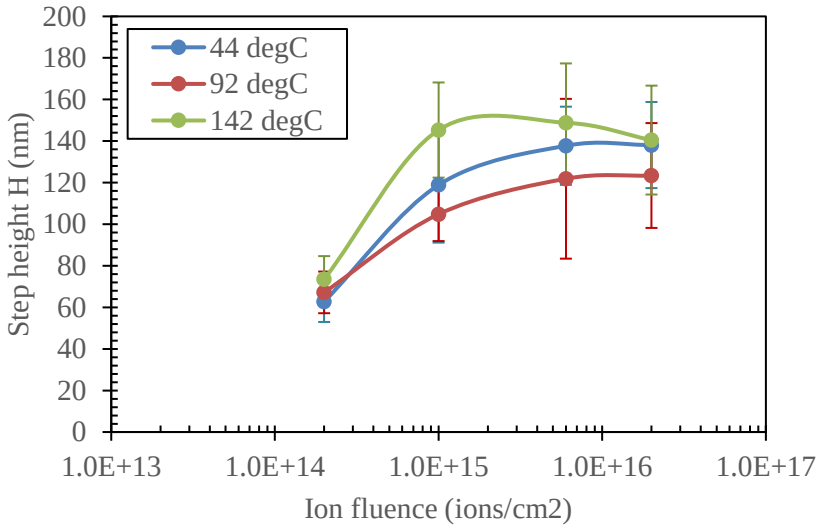

Fig.3- 5. The effects of temperature on out-of-plane swelling in microcline induced by 3 MeV Si^{2+} irradiation with ion flux 1.5 x 10^{12} ions/cm^2.s

Maximum volume change in three minerals at room temperature

Obtaining the step heights at saturation, the maximum volume change can be estimated by the step heights normalized by ion ranges of 18.1%, 9.1%, and 5.8% for quartz, albite, and microcline, respectively. In a previous study, the maximum RIVE of quartz and feldspars induced by neutrons was approximately 18% and 7%–8%, respectively, as evaluated in [12]. Compared with neutron-irradiated data, the obtained value was similar to that for the case of quartz; however, our data indicated different expansions in albite and microcline, i.e., approximately 20% higher and lower, respectively. This discrepancy may be because ion irradiation caused an expansion in one direction toward the open surface, and swelling data were collected at several positions of the target minerals. Meanwhile, in the case of neutron, the total volume change is an integrated expansion of each grain, which may be confined by other grains or other structures. Besides, natural minerals may contain silica, which can increase the total expansion in microcline because of neutrons.

3.2.2. TEM observation

The cross-section of irradiated minerals observed via TEM showed the different amorphization behavior between quartz and feldspars (as Fig.3- 6.). In quartz, the diffraction spots were fully disappeared, and diffraction rings appeared at the fluence of 2×10^{14} cm^{-2}, which was lower fluence than the saturation of amorphization. In contrast, the saturation of amorphization was confirmed at the fluence of 1×10^{15} cm^{-2} in feldspars, which was well agreed with the saturation of step height increment. The TEM results indicated that the fluence dependences of the RIVE were similar for the three minerals but their mechanism differed. In feldspars, the RIVE was fairly correlated with amorphization. Meanwhile, the RIVE in SiO_2 continued even though amorphization was completed at a lower fluence. This means the amorphization does not require maximum volume expansion under constraint. Furthermore, the structure relaxation during irradiation of crystalline silica and vitreous silica (glass) behaved differently, thus there would be different types of irradiation-induced amorphous silica. The results indicated the potential constraining effects on the structural relaxation of neutron-irradiated aggregate when embedded in concrete structures.

A higher magnification TEM analysis was performed for the amorphized quartz and confirmed the potential existence of nanocavities using the through-focus technique. Circular contrasts were observed, in which black and white reversals were identified, as shown in quartz at 1×10^{15} cm^{-2} (see Fig.3- 7.). A similar feature was observed with almost the same sizes for the quartz sample irradiated at 6×10^{15} cm^{-2}. They measured approximately 4 nm and tended to disappear gradually after long exposure to the electron beam. Since it is difficult to identify the thickness of amorphized specimens, it is not easy to quantitatively determine the cavities. A rough estimation gives the density of cavities at around 10^{23} (m^{-3}), thus the direct contribution of the cavity formation on the swelling is less than 1%. This result suggests both further

relaxation of network and formation of cavities can contribute to additional swelling in SiO_2.

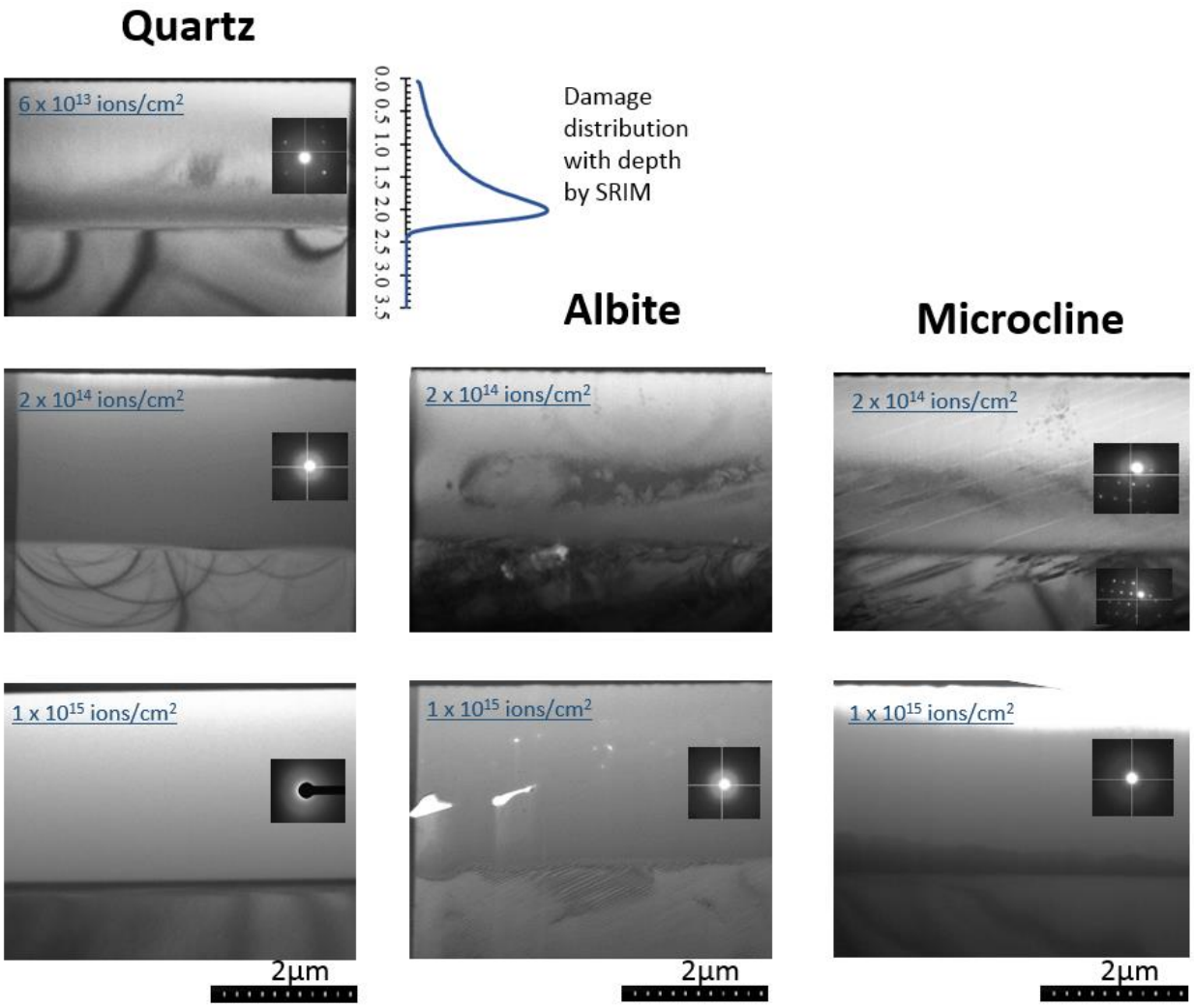

Fig.3- 6. Bright-field TEM image of sample irradiated by 3 MeV Si^{2+} irradiation to fluence 2 x 10^{14} ions/cm^2 at 44°C. The amorphization was confirmed by selected area diffraction technique.

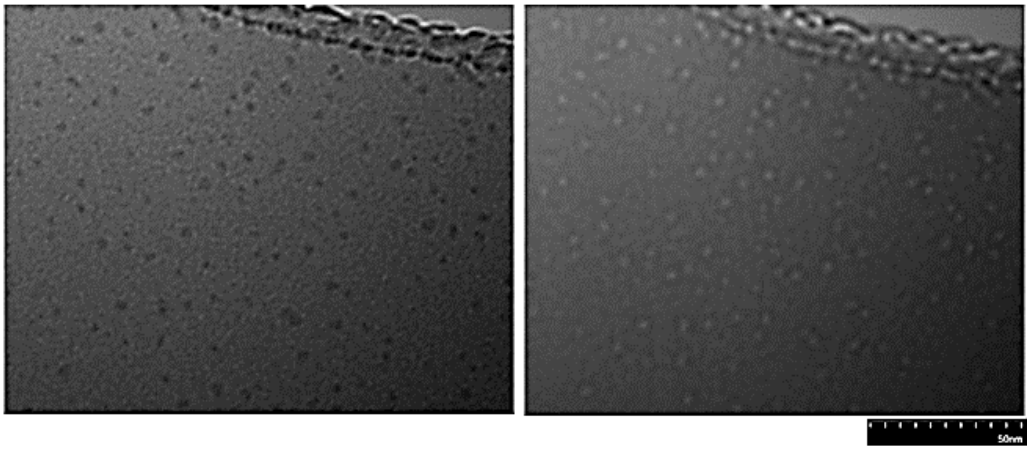

Fig.3- 7. Cavity formation in quartz Si-irradiated at 1 × 10^{15} ions/cm^2 (the left image is overfocused and the right image is underfocused). This suggests that cavity formation contributes to further volume expansion

3.2.3. Amorphization under electron-ion irradiation

In order to observe the temperature effect in the amorphization process, 1MeV Fe-ion irradiation was introduced into 200keV TEM chamber with an angle of 30 degrees from the TEM column, so-called in-situ TEM. The experiment was carried out at the heavy ion irradiation facility at the University of Tokyo. By SRIM simulation, 1MeV Fe ion could produce a homogenous knock-on displacement within the TEM sample. A bright-field images were observed using a 200 keV electron beam while irradiating 1 MeV Fe ion at 6 × 10^{10} $cm^{-2}s^{-1}$. For high-magnification, the flux of the electron beam is estimated to be about 3 × 10^{18} $cm^{-2}s^{-1}$ using a Faraday cup.

Fig.3- 8 (a) to d)) shows the evolution in the cases of room temperature (RT) irradiation, while Fig.3- 8 (e) to h)) are irradiated at 150°C, which seems to progress faster amorphization than that at RT irradiation. In the high-magnification observation, the regions surrounded by the red circle show a different contrast and faster amorphization to other regions. However, the amorphization behavior is

different between the thinned region (thickness is 200 nm or less) in the center of the sample and the region next to it (thickness is 200 to 400 nm).

Fig.3- 9 shows the results of high-magnification observation which was obtained in the same experiment as Fig.3- 8. It noted that when electron irradiation is concentrated on the TEM sample, the amorphization is quite quick and the sample is bent under irradiation due to expansion, thus it is difficult to adjust the beam condition to have a good diffraction condition. To obtain some insights, the bright-field image is represented. In the case of RT and 150^{o}C irradiation, the black dots appeared at the beginning of irradiation. The black dots can be lattice defects. However, for longer irradiation, the number of black dots increased, and its size was almost not changed in the case of RT, in contrast to 150^{o}C irradiation, in which the number density of black dots was unchanged and its size increased, as shown in Fig.3- 10. Because it showed the same feature under different diffraction orientations, the black dots in the case of 150^{o}C could be lattice strain regions caused by amorphous region formation. The ring-shaped contrast can be regarded as representing the outer edge of the amorphous region.

The results indicated that at RT irradiation, radiation defects will be accumulated at the position of formation; however, at higher temperatures, the mobility of defects is much higher, so that the amorphous regions are nucleated and grown. The enhanced mobility of defects may explain the increasing rate of RIVE or structural relaxation at higher temperatures (in Fig.3- 3).

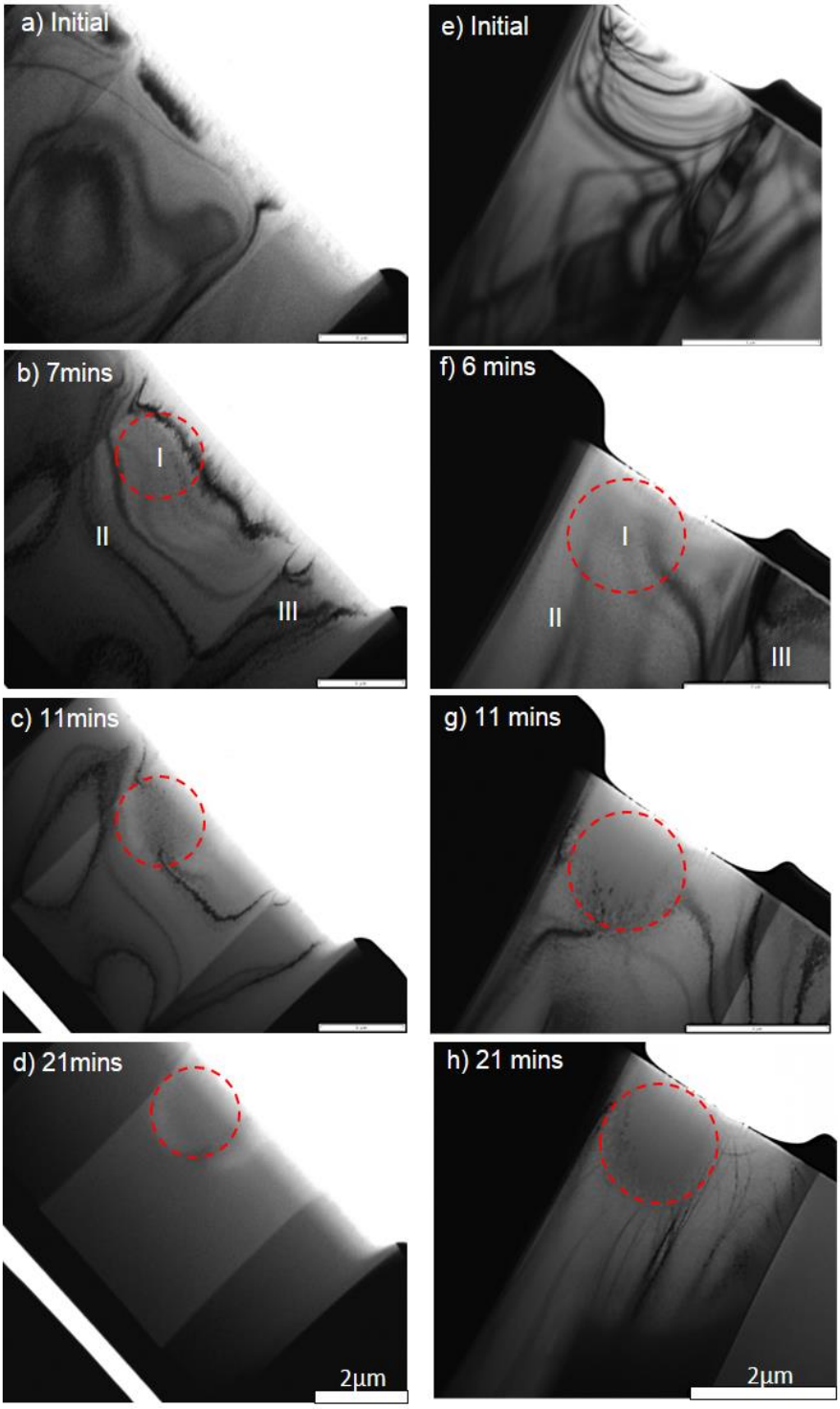

Fig.3- 8. Low-magnification image of quartz irradiated with Fe ions at ion flux 6×10^{10} $cm^{-2}s^{-1}$ *and observed under electron beam in TEM. (a-d images are irradiated RT; e-h images are at 150°C)*

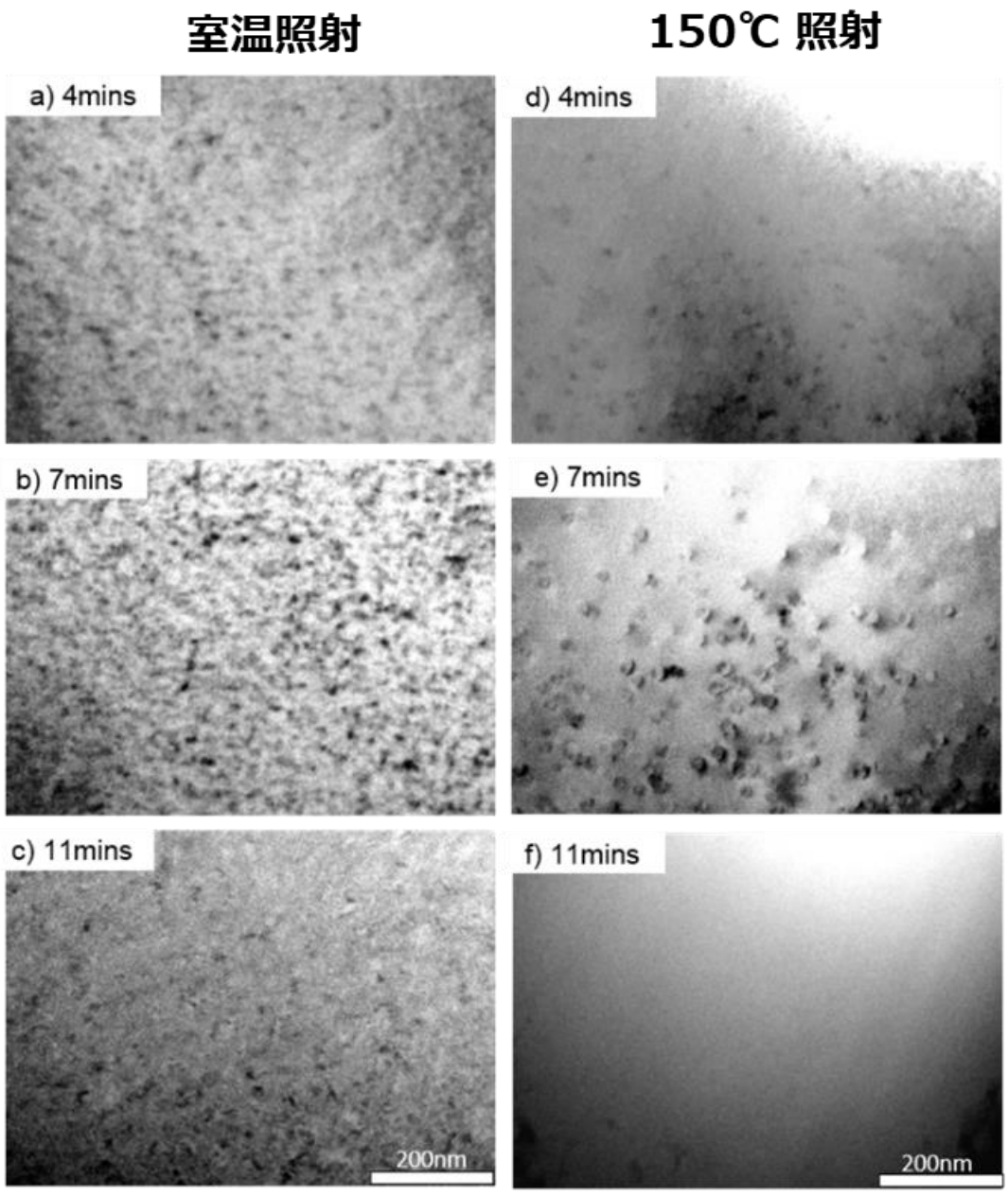

Fig.3- 9. High-magnification image of quartz irradiated with Fe ions at a flux of 6×10^{10} $cm^{-2}s^{-1}$ *and electron beam with a flux of about* 3×10^{18} $cm^{-2}s^{-1}$

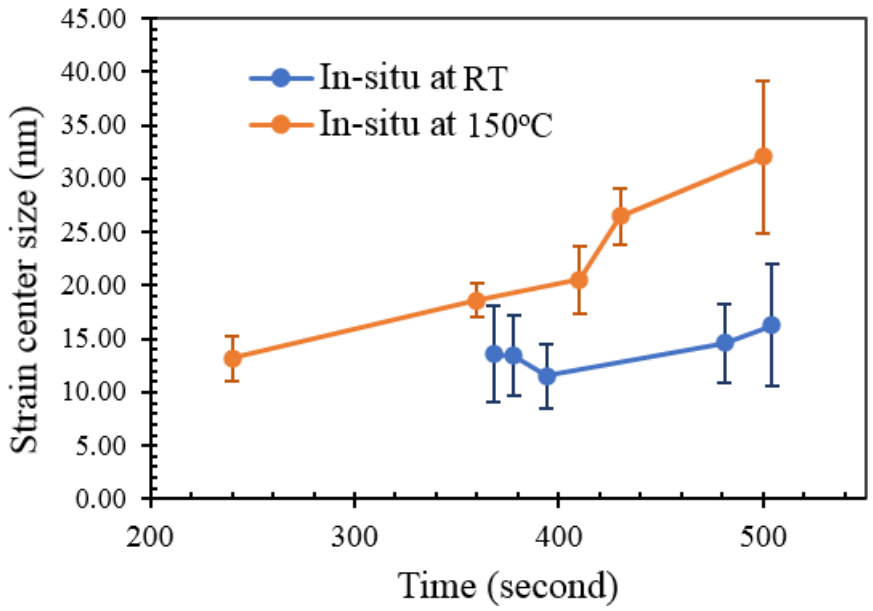

Fig.3- 10. Changes of strain center size during In-situ TEM at RT and 150°C

3.2.4. Nanoindentation

Considering the indentation size effect, several indentation-depth tests were conducted on amorphized minerals. The values of hardness and Young's modulus of amorphized quartz at different loads (2 mN – 80 mN) with a maximum depth ratio, $h_{max}/R = 0.36$ showed a variation of less than 4% (as illustrated Fig.3- 11).

The results of nanoindentation are summarized in Table 3- 1 and Fig.3- 12 The obtained values of the unirradiated state are similar to or between the range reported previously. It is noteworthy that the hardness data of amorphized minerals are rare in the literature, particularly for albite and microcline. The results showed that:

- In microcline, the hardness value first reduced from 10 GPa to approximately 6 GPa and then remained almost constant after 2×10^{14} cm^{-2}. Meanwhile, the change in Young's modulus was not apparent before and after irradiation.
- In the case of albite, the hardness change was similar to that of microcline, whereas Young's modulus decreased gradually with increasing ion fluence.

Furthermore, previous MD simulations showed a decreasing trend from 111.2 to 91.0 GPa [46], which is the same reduction magnitude as that of the present study, although the absolute values were higher by approximately 20%.

- In quartz, the hardness gradually decreased from 14.8 GPa to approximately 9.4 GPa at a fluence of 2×10^{14} cm^{-2} and then remained almost unchanged. The hardness obtained at 2×10^{14} cm^{-2} (corresponding to an amorphous fluence) was similar to that of fused silica (9.19±0.27 GPa). Interestingly, Young's modulus of pristine and amorphized SiO_2 was 112.4 and 95.5 GPa, respectively. This contradicts with MD simulations, which showed an *increase* from 104.8 to 126 GPa in the final amorphized state, in contrast to the density, which decreased gradually with deposited energy [46]. However, the MD results appear inconsistent with the well-known 30% lower elastic modulus in fused silica (approximately 70 GPa [109]) compared with crystal quartz.

The different trends obtained from MD simulations for quartz are possible owing to the difference in the measurement scale. The MD simulations may be able to show the change in Young's modulus in local structures, such as changes by a few nanometers [46]; however, the cell size of the MD simulation is small, and/or the time scale is short to represent the formation of nanocavities. Additionally, the estimation of the elastic properties of amorphous silicates may be affected by the strain rate [115].

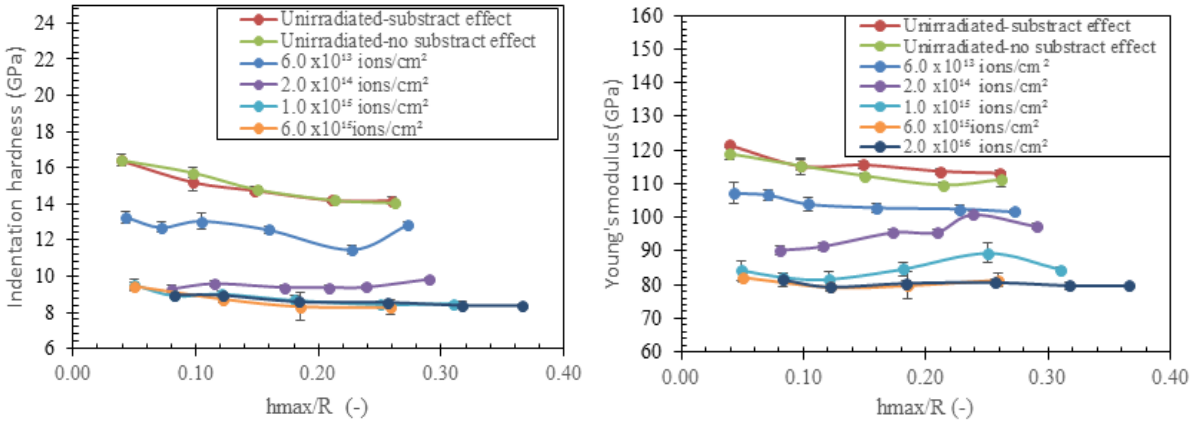

Fig.3- 11. Substrate and indentation size effect on hardness and Young's modulus in quartz sample

Table 3- 1. Mechanical properties of irradiated tectosilicates

	Quartz		**Albite**		**Microcline**	
	This work	Previous studies	This work	Previous studies	This work	Previous studies
E_0 (GPa)	112.40±0.74	105 for c-axis [109]; 99.45[116]	85.28±5.40	70.65[43]; 101.98[117]	69.41±3.76	77.7[118]
H_0 (GPa)	14.80±0.20	13.28 [b] [109]	9.59±0.81		10.04±0.69	9 [119]
ν_0	0.08 [a]	0.06[116], 0.08[109]	0.28 [c]	0.28[43]	0.28 [c]	0.28[118]
E_r [d] (GPa)	80.42±0.68		70.50±8.09		66.24±6.76	
H_r [d] (GPa)	8.59±0.11		5.84±0.89		6.10±0.85	
ν_r	0.21 [a]		0.28 [c]		0.28[c]	

[a] *obtained from* [75], [b] *The value was obtained by digitizing figure in* [109], [c] *Poisson's ratio is assumed constant based on comparison of ν calculated from compliance tensor* [46], [d] *the* E_r, H_r *are taken at the maximum ion fluence 2 x* 10^{16} *ions/cm*^{2}

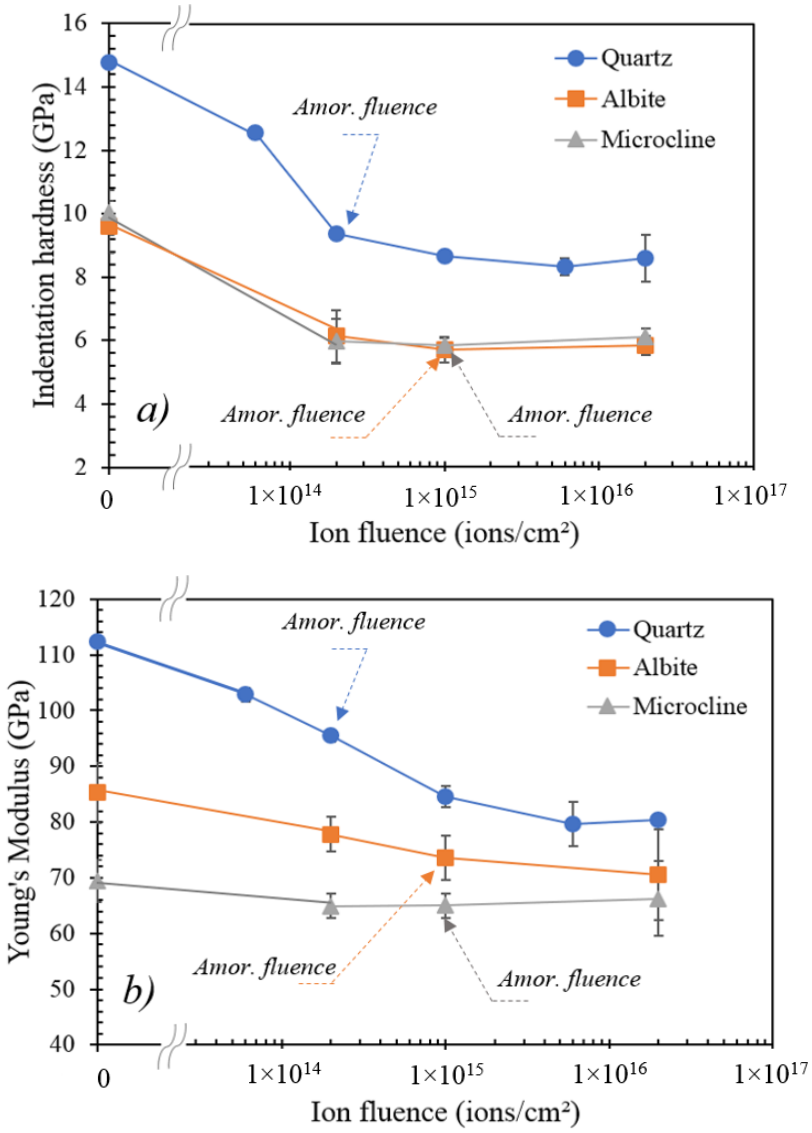

Fig.3- 12. Hardness (a) and Young's modulus (b) of ion-irradiated minerals (quartz, albite, and microcline) at different ion fluences

3.2.5. Electron spin resonance

E' center

In silica, the most important defects are E' centers, which are holes trapped at the oxygen vacancies ((≡Si-O-Si≡) => (≡Si·)). Other defects can also be detected by ESR are the nonbridging oxygen hole center (NBOHC) and peroxy radical (POR). They are three fundamental defects that are generated under irradiation, though other

defect structures may be produced, they are difficult to be detected by ESR. Fig.3-13 illustrates the representative ESR signals of He irradiated sample to 3.2 $x10^{16}$ (ion/cm^2) and 60min-isochronal annealing test with the reference peaks of Mn^{2+} marker. The ESR signals between Mn marker peaks were induced by irradiation since the spectrum of the unirradiated sample is flat. The g values of irradiated samples were determined to be around g = 2.00032, g = 2.00153, and g = 2.00232, which are almost similar for all samples listed in Table 2-3, regardless of different irradiation types and samples (Fig.3- 13 and Fig.3- 14). This indicates that the defect structure formed in heavily damaged quartz and silica glass under irradiation has a similar characteristic. Since the g vector of E' centers in crystalline quartz has orthorhombic symmetry, it has three principal values of g_1 = 2.0003, g_2 = 2.00053, and g_3 = 2.00179, in which the g_1 and g_2 are close to each other [120].

It can be seen that the resonance line of the sample is located at g = 2.00153, which is close to the g_3 of E' center. The E' center was also determined at the resonance line at around g_1,g_2 = 2.0005 [121,122] or g = 2.0008[123]. It should be noted that the peak intensity at g = 2.00232 is shorter than the peak at g = 2.00032. This could be due to the overlapping of other components such as NBOHC and/or POR that causes the subtraction of peak intensity; this has been identified by Moritani et al [124].

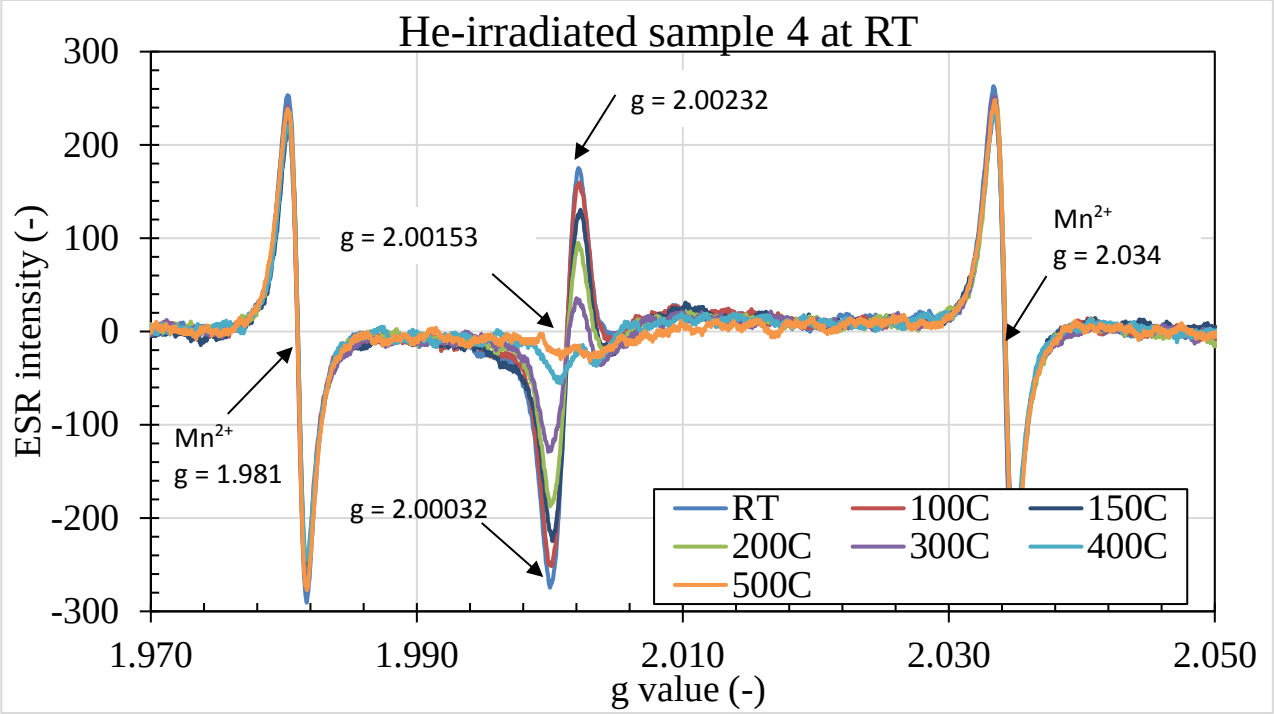

Fig.3- 13. The ESR spectra of He-irradiated SiO_2 to 3.2 x10^{16} (ion/cm^2) following isochronal annealing up to 500^{o}C for one hour.

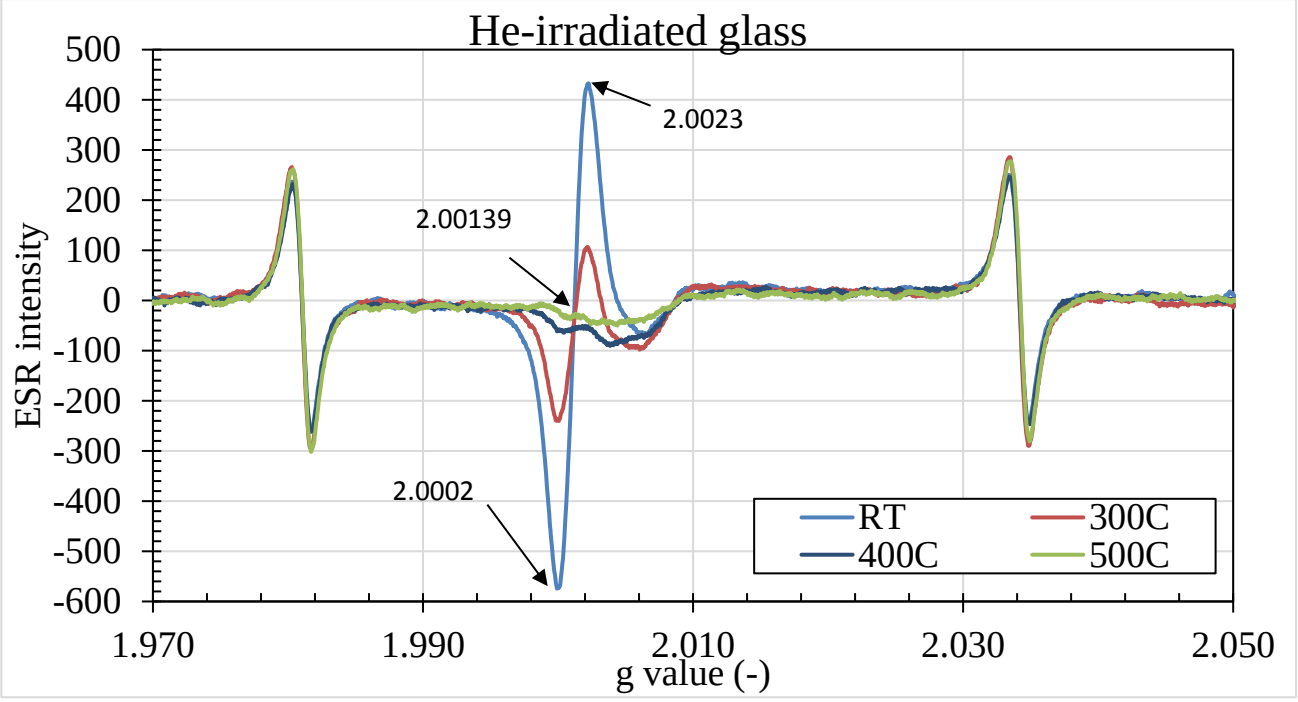

Fig.3- 14. The ESR spectra of He-irradiated glass to 3.6 x10^{15} (ion/cm^2) following isochronal annealing up to 500^{o}C for one hour.

Isochronal annealing

Fig.3- 15 shows the results of 60mins-isochronal anneal of He-irradiated and Si-irradiated samples. The ESR intensity is determined at g = 2.00032, as shown in Fig.3- 13 and the relative intensity was calculated by the intensity of annealed sample divided by the initial intensity and plotted against the temperature. As seen in Fig.3- 15, the spin intensities rapidly decrease beyond 100^{o}C and fully annealed at 500^{o}C. This behavior is quite similar to that of E' centers produced in quartz by He-irradiation [125] and that produced in vitreous silica by neutrons [126]. However, under gamma and neutron irradiation, whose irradiation dose is much lower than amorphization fluence, E' centers and other centers were found to recover after 300^{o}C [51,120,127]. This implies that the recovery of E' centers in heavily damaged (or in amorphous structure) occurs at a lower temperature than that in crystalline quartz. As seen in Fig.3- 15, no clear recovery stage was observed, this is probably due to the short annealing time so that isothermal annealing tests were performed.

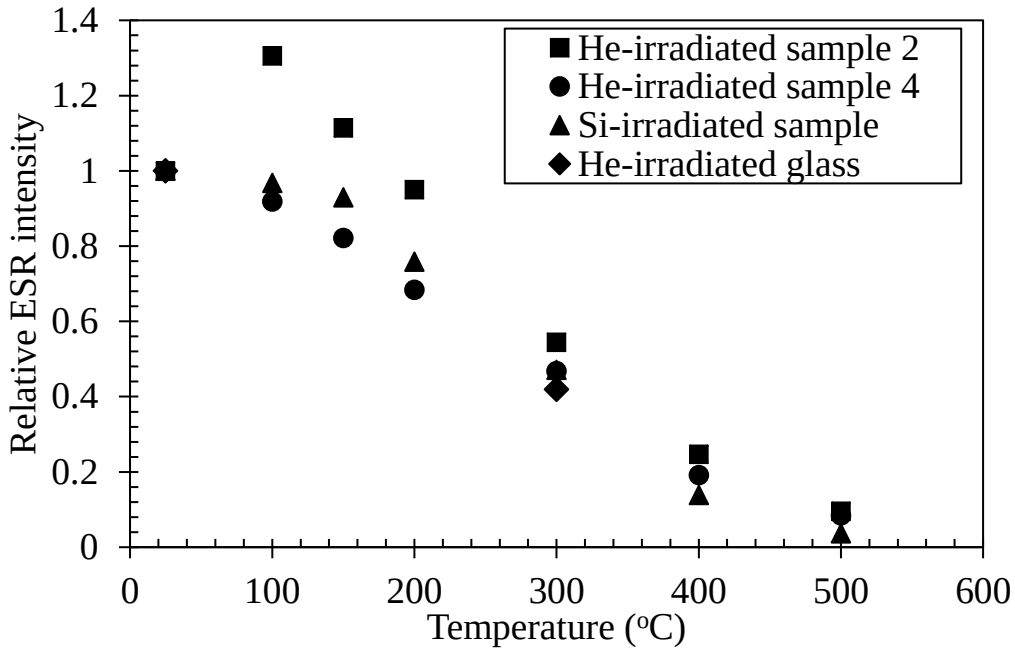

Fig.3- 15. The 60mins isochronal annealing experiments of different irradiated samples

Isothermal annealing

Fig.3- 16 shows the results of changes in relative intensities against annealing time. As seen in the cases of 150ºC that the recovery process is very slow and reaches almost saturation after three hours; however, the recovery continues after heated to higher temperatures. This implies that different recovery reactions may occur at different temperatures.

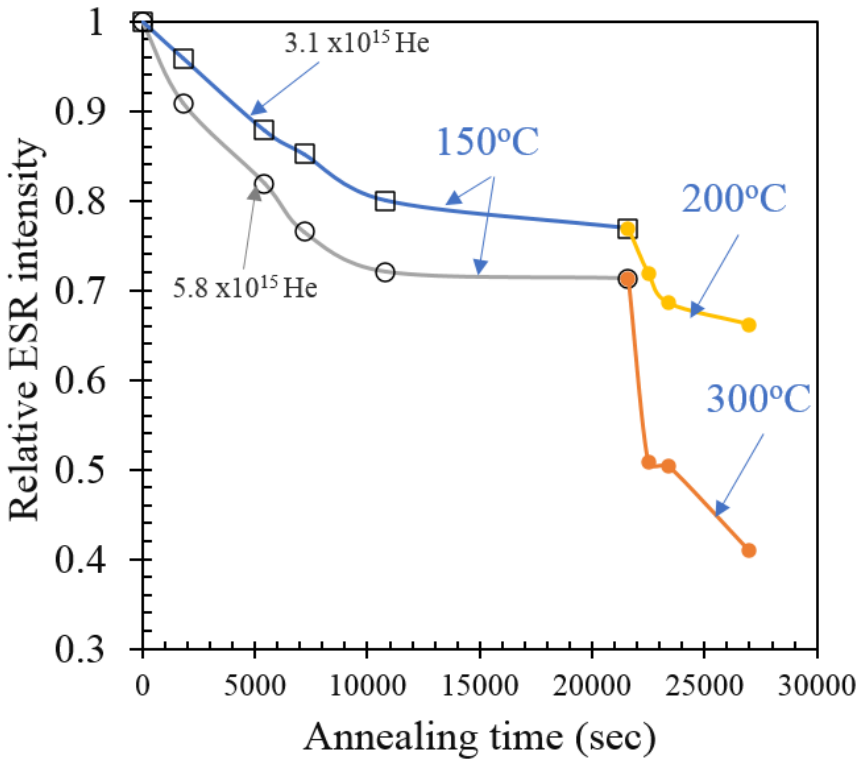

Fig.3- 16. Isothermal annealing of He irradiated samples

3.3. Discussion

3.3.1. Swelling cross-section

Since neutron irradiation has a broad spectrum of primary knock-on atom (PKA) energy, to capture the tendency of expansion induced by different PKA energies, we compared our results with others with different ion energies as shown in Fig.3- 17.

The swelling occurred at certain ion fluence depending on the ion type and energy, followed a rapid increase within one order of fluence value, and then become saturated. The swelling data can be separated into two groups:

(1) for sufficiently high electronic energy loss (≥1.6 keV/nm), continuous amorphous tracks may be formed by a single hit process due to electronic excitation; and

(2) collision process, in which the small disordered regions may be produced due to the damage cascades and subsequent rapid cooling that does not allow to restore the ordered structure within the cascades.

Noted that most of the PKA energies in neutron irradiation are less than the excitation energy threshold, but for sake of completeness, some excitation process data are also included. In the case of excitation, the expansion of irradiated samples can be fitted with the Poisson equation considering the formation and overlapping of amorphous ion tracks, as examples given by [55,57,128]. For the collision process, Avrami model [74] has been commonly used to describe the amorphization process based on nucleation and growth of disordered phases [60,129,130]. However, this model may not be suitable because we found that even after the amorphization has fully occurred, the volume expansion continued at a higher dose. Therefore, in this case, we simply assume that *dimension change after amorphization* can also be described by Poisson's law:

$$\boldsymbol{H = H_{\infty}[1 - exp(-\sigma_s \phi)]} \quad \textit{Eq.3- 1}$$

where H is the step height, H_{∞} is the maximum step height at saturation of swelling, σ_s is the swelling cross-section $((\Delta H/\Delta \Phi)/ H_{\infty})$, which is assumed to be a temperature-dependent parameter (σ_s *is the magnitude of the volume expansion due to single radiation*). The equation is based on the following four assumptions:

(1) the expansion is directly induced by single ion injection;

(2) volume change occurs along with surface direction;

(3) the swelling rate increases with increasing temperature;

(4) once it becomes amorphous, it is irreversible.

These assumptions ignore the radiation defect recovery, and this equation could not distinguish the different types of amorphous silica. It is interesting that many experimental data are well-fitted with Poisson's curve, as shown in Fig.3- 17. The reason is that it is natural that many amorphous solids undergo plastic flow under ion irradiation [131–133]. The flow phenomenon is a radiation-induced process because irradiation temperature is far below the glass temperature and it occurs to relieve in-plane stress. The plastic flow has been explained based on thermal spike [134] when the electronic excitation dominates the stopping with dE/dx > 1keV/nm, and "flow defects" when recoil energy is small (below 0.5keV) [135]. Since the relaxation time was estimated at the order of ps [134,136], it is considered the volume change of amorphized silica is induced by a direct ion injection.

As seen in Fig.3- 17, the ion fluence for swelling is dependent on irradiation parameters, i.e. ion energy and ion mass. The threshold ion fluences required for light ions (He and H) are higher than that for heavier ones (Au, Fe, Si, and Na). In comparison between 140 keV He and 2 MeV He, the lower ion energy cause swelling with less ion fluence. This may be due to the higher possibility of an ion causing an elastic collision with a target atom comparing with those higher energies. Except for the case of light ions (2MeV He and 140 keV H), the data are fairly well fitted with the equation (1). The given errors in light ions irradiation may be due to that the damage is not surpassed along with the entire ion range and the deeply

formed amorphous layer may be subjected to large compression stress, which would delay the structural relaxation process.

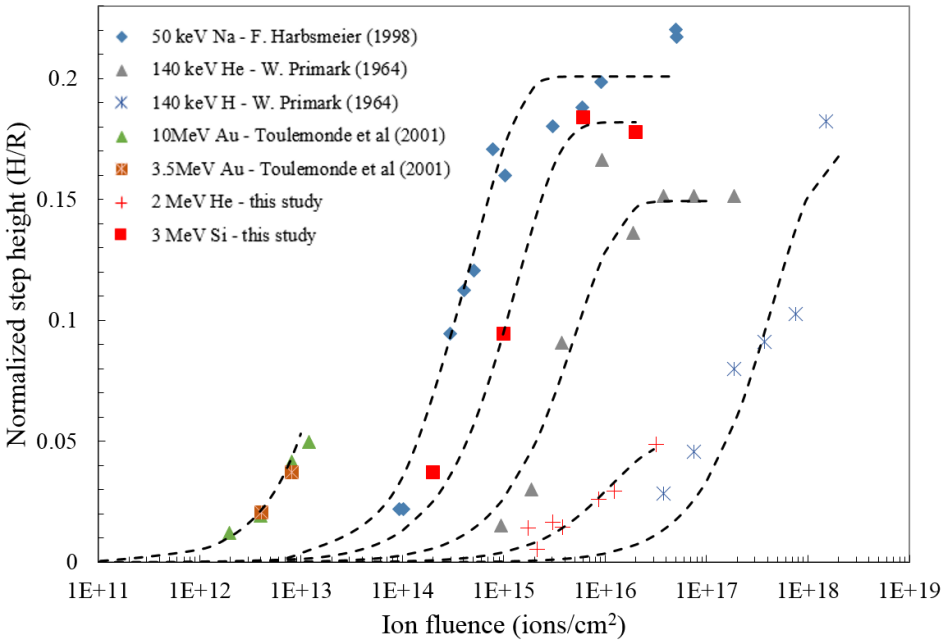

Fig.3- 17. The normalized step height by divided ion range as a function of the ion fluence. Dash lines are the least square fits by Poisson law. All specimens were irradiated at room temperature, except 50keV Na at -196°C.

Though the swelling cross-section σ_s(cm^2) generally increases with the increasing number of displaced atoms in the ion range, N_d/R when the electronic (dE/dx) is not too high in this case, nonlinear relationship between N_d/R and σ_s was found, as shown in Fig.3- 18. In cases of light ion irradiations whose damage is not surpassed along with the entire ion range, σ_s with $N_d/R < 0.16$ nm^{-1} is the order of 10^{17} - 10^{-18} cm^2. If elastic collision is the main cause of amorphization under all irradiations summarized in Fig.3- 17, the relationship between σ_s and N_d/R should be proportional, except for the effect of damage depth distribution. Even in the higher energy cases, however, the nonlinear relation is recognized. In the range of $0.16 < N_d/R < 5.43$, σ_s is approximately 10^{-15} cm^2, and highest for the case of Au 3.5MeV

and 10MeV, beyond N_d/R > 5.43 of around 5 x 10^{-14} cm^2. Based on the several experiments using swift heavy ions [71], the relationship between electronic dE/dx and swelling can be described as

$$\boldsymbol{\sigma_{s,i}}\ [10^{-14}\text{cm}^2] = 0.13\times(\boldsymbol{E_i}/R - 1.6)\ [\text{keV/nm}] \quad \textit{Eq.3- 2}$$

where the $\sigma_{s,i}$ is the normalized initial swelling by ion range, (ΔH/ΔΦ)/R, caused by ionization, E_i is the electronic deposited energy.

By converting swelling data induced by collision to the same unit with $\sigma_{s,i}$, we found that swelling induced by collision can also be described as a linear relationship with N_d,

$$\boldsymbol{\sigma_{s,c}}[10^{-14}\text{cm}^2] = 0.0072\times(N_d/R)\ [\text{displacements/nm}] \quad \textit{Eq.3- 3}$$

Then, the total swelling cross section is expressed as:

$$\boldsymbol{\sigma_s[10^{-14}cm^2]} = \left[\mathbf{0.0072}\left(\frac{\boldsymbol{N_d}}{\boldsymbol{R}}\right)\right] + \left[\mathbf{0.13}\left(\frac{\boldsymbol{E_i}}{\boldsymbol{R}} - \mathbf{1.6}\right)\right] \quad \textit{Eq.3- 4}$$

Fig.3- 19 presents the comparison of experimental and calculated swelling (from equation (2)), considering both collision and ionization effects. The best estimation is found at the low swelling level ≤ 6%, at which the amorphization is formed inside the surrounding crystalline matrix and they show a similar trend until the whole irradiated layer becomes amorphous. Beyond that level, however, some scatters are observed, the swelling of different amorphous layer thickness may be largely affected by external stress from different fixation conditions of specimens. Besides, the temperature variation of different ion experiments as well as the impurity content of quartz from different origins would also be the scattering sources. Assuming the complete amorphization at 6% swelling, the critical dose can be calculated from $\sigma_{s,c}$

as 0.11dpa (as Fig.3- 20). The obtained dose is within the range by [60] and [45], who reported the critical dose for amorphization using different methods. It should be noted that the threshold dose from this study is defined at the dimension change, the dose requires for amorphization may be lower due to delay of relaxation.

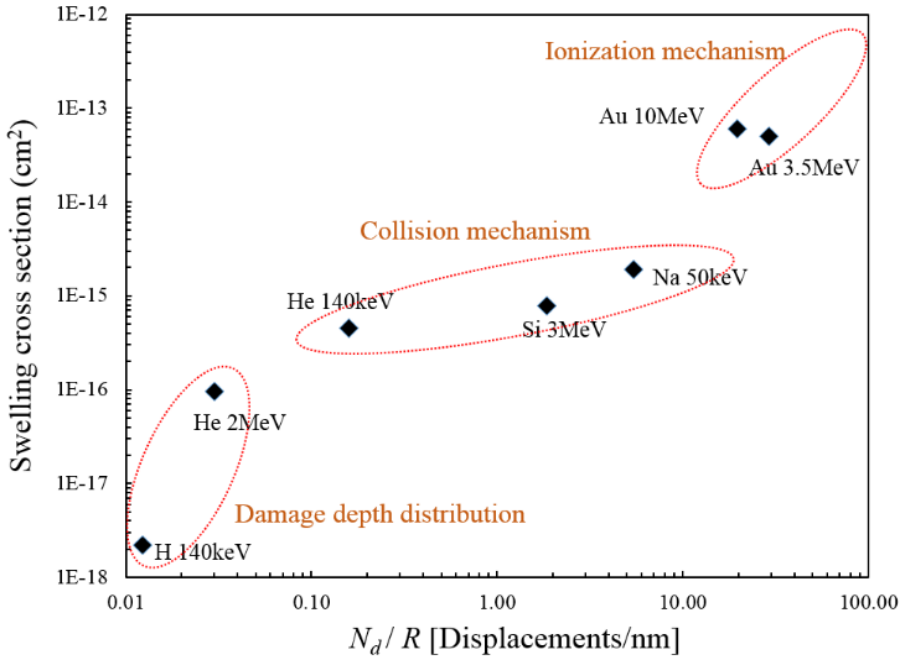

Fig.3- 18. The relationship between the swelling cross-section extracted from the fitting versus the normalized number of displaced atoms by incident ion determined by SRIM simulation.

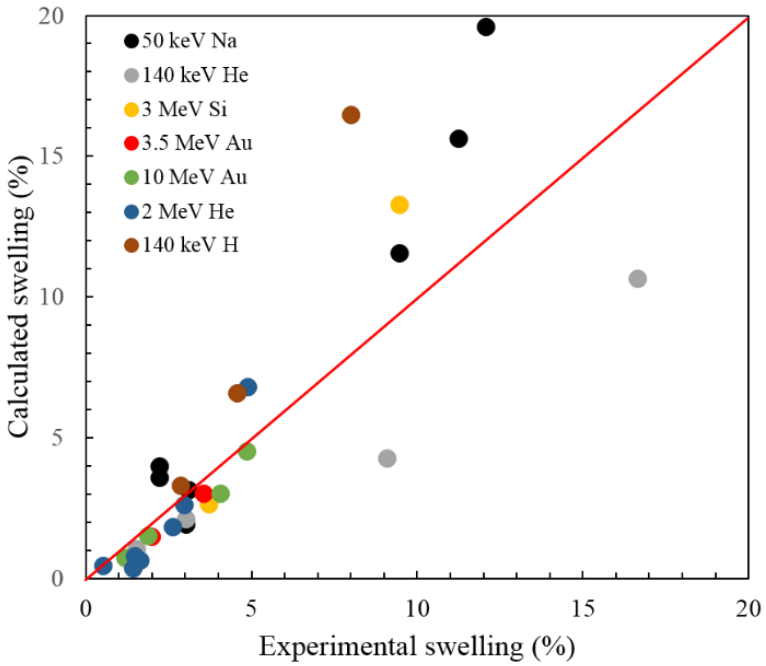

Fig.3- 19. Scatter plot of experimental and calculated swelling, considering both collision and ionization induced swelling cross-section.

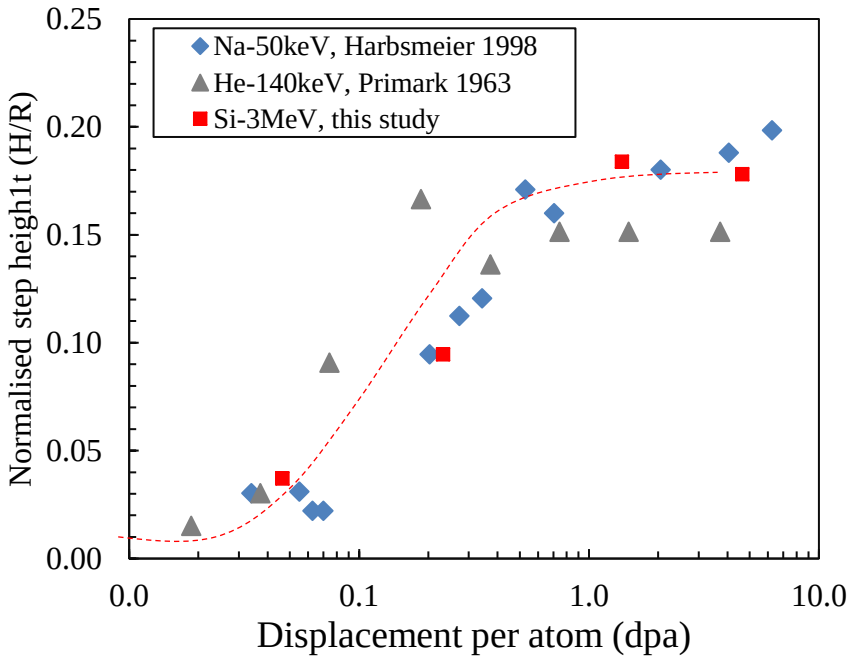

Fig.3- 20. RIVE as a function of knock-on displacements

Similar to the case of quartz, Poisson law was also applied in feldspar and it fitted quite well. The result of amorphization dose and swelling cross section are summarised in Table 3- 2.

Table 3- 2. Summary of amorphization dose and swelling cross-sections

Minerals	Density ρ (g/cm^3)	Amorphization fluence (cm^{-2})	Critical energy density (eV/ atom)	Max. swelling (%)	Swelling $(\Delta H/\Delta \Phi)/R$ (cm^2)
Quartz (SiO_2)	2.65	2.0×10^{14}	3.5	18.1	1.44×10^{-16}
Albite ($NaAlSi_3O_8$)	2.62	1.0×10^{15}	17.3	9.1	1.23×10^{-16}
Microcline ($KAlSi_3O_8$)	2.56	1.0×10^{15}	18.4	5.8	1.61×10^{-16}

In neutron irradiation, the critical dose for amorphization has been reported at $\geq 1 \times 10^{20}$ $n.cm^{-2}$ [13,70,137]. Since the maximum energy of primary knock-on atoms by fission neutron is in the order of 10^5 eV, the electronic energy loss by the knock-on atoms will never cause direct amorphization by excitation. Thus, amorphization by neutron is mainly due to the displacement mechanism. The viscous flow effect is a time-dependent phenomenon; however, the amorphous region induced by neutron irradiation is embedded in the crystalline matrix, and the surface does not exist nearby the region, volume expansion could be restricted due to the compression stress from the matrix. Our study shows that the RIVE in amorphized silica is affected by additional irradiation as well as applied stress.

3.3.2. Activation energy of structural relaxation during RIVE

We have found that stress relaxation plays an important role in controlling the expansion level. Therefore, the temperature dependence of σ_s is mainly caused by the relaxation thought the temperature range is significantly lower enough than the softening temperature of silica glass and can be expressed as

$$\boldsymbol{\sigma_s = \sigma_{so}\,\exp(-E_a/kT)} \quad \textit{Eq.3- 5}$$

where E_a, k and T are the activation energy of swelling, the Boltzmann constant, and temperature (K), respectively)

From Arrhenius plot between the logarithm of σ_s and the reciprocal temperatures, as shown in Fig.3- 21, the activation energy of relaxation, E_a was estimated to about 0.13eV. Such low activation energy supports the idea that plastic flow does not occur through bond breaking but by bond motion [131], this energy is consistent with Brongersma et al (E_a =0.2eV) who suggested the energy is related to radiation-induced viscosity [136]. This suggests that the activation energy may be related to the energy barrier for the rearrangement of the atomic network which causes to release the stress induced by the amorphous phase. This result appears to be in contradiction with neutron-irradiation data (Bykov et al., 1981 [48]) showing that higher irradiation temperature tends to lower expansion rates. Nevertheless, there are two major differences:

(1) the expansion in Bykov data occurs due to the build-up of atoms in channels [49] and density change of amorphous zones that are *progressively* transformed to amorphization, while we observed the tendency of volume change after amorphization under the effect of physical constraint (external stress);
(2) the expansion rate in neutron-irradiation may be inversely proportional to the mobility and recovery of point defects which tend to be enhanced at higher

irradiation temperature, while the *amorphized solid* can easily undergo plastic flow, just as easily at low temperature (-173°C) [131]. In the case of thermal spike, higher irradiation temperature larger the region has been fully relaxed [136]. Therefore, the RIVE is controlled by additional irradiation, as well as both stress and temperature. Radiation-induced viscosity may be the reason why the Poisson's law assumption is apparently valid in many experiments.

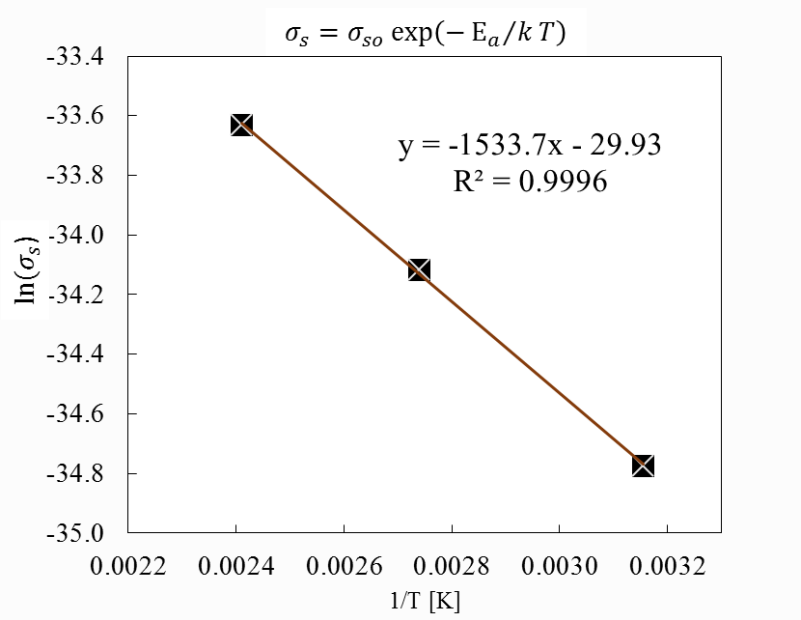

Fig.3- 21. Correlation between the logarithm of swelling cross-section in quartz induced by 3 MeV Si^{2+} irradiation with ion flux 1.5 x 10^{12} ions/cm^2.s and the reciprocal temperature (Arrhenius plot, activation energy: 0.13eV).

In summary, it has been observed that the defect mobility is enhanced at 150°C under in-situ TEM, some defects can be annealed at low temperatures (from 100°C) by ESR experiments, and we have obtained the activation energy for viscous flow is quite low at about 0.13eV. In addition to that, a previous study showed that the viscous flow under irradiation is governed by the flow of defects[135]. Thus, it is important to determine the activation energy for the defect which causes the recovery

of E’ centers (i.e., oxygen vacancies) to confirm whether they have the same order of activation energy.

It is assumed that the change in quantities of oxygen vacancies is proportional to the E’ intensity. In previous studies, the relative change in E’ center quantity has been explained by second-order reaction [127,138]:

$$\frac{\mathbf{1}}{\boldsymbol{N}} = \frac{\mathbf{1}}{\boldsymbol{N_0}} + \boldsymbol{\lambda t} \quad \textit{Eq.3- 6}$$

where, N_0 and N is the quantity of E’ centers; λ is the decay constant, which is a function of temperature $\lambda = A\exp\left(\frac{E_{a2}}{kT}\right)$ (A is the frequency factor, E_{a2} is the activation energy).

Fig.3- 22 shows the reciprocal of the intensity against annealing time, and Fig.3- 23 presents the Arrhenius plot of ln (λ) versus reciprocal temperature for E’ centers. The calculated activation energy for E’ center to be recovered is around 0.11eV. It is known that the recovery of the E’ center can occur when it recombines with oxygen, however, E’ centers can also be converted into other defects such as (≡Si-Si ≡). Thus, the recovery of E’ centers may not be a single process. From the obtained values, the activation energy for the reaction of E’ center is almost similar to that of the required energy for viscous flow in amorphized silica to occur.

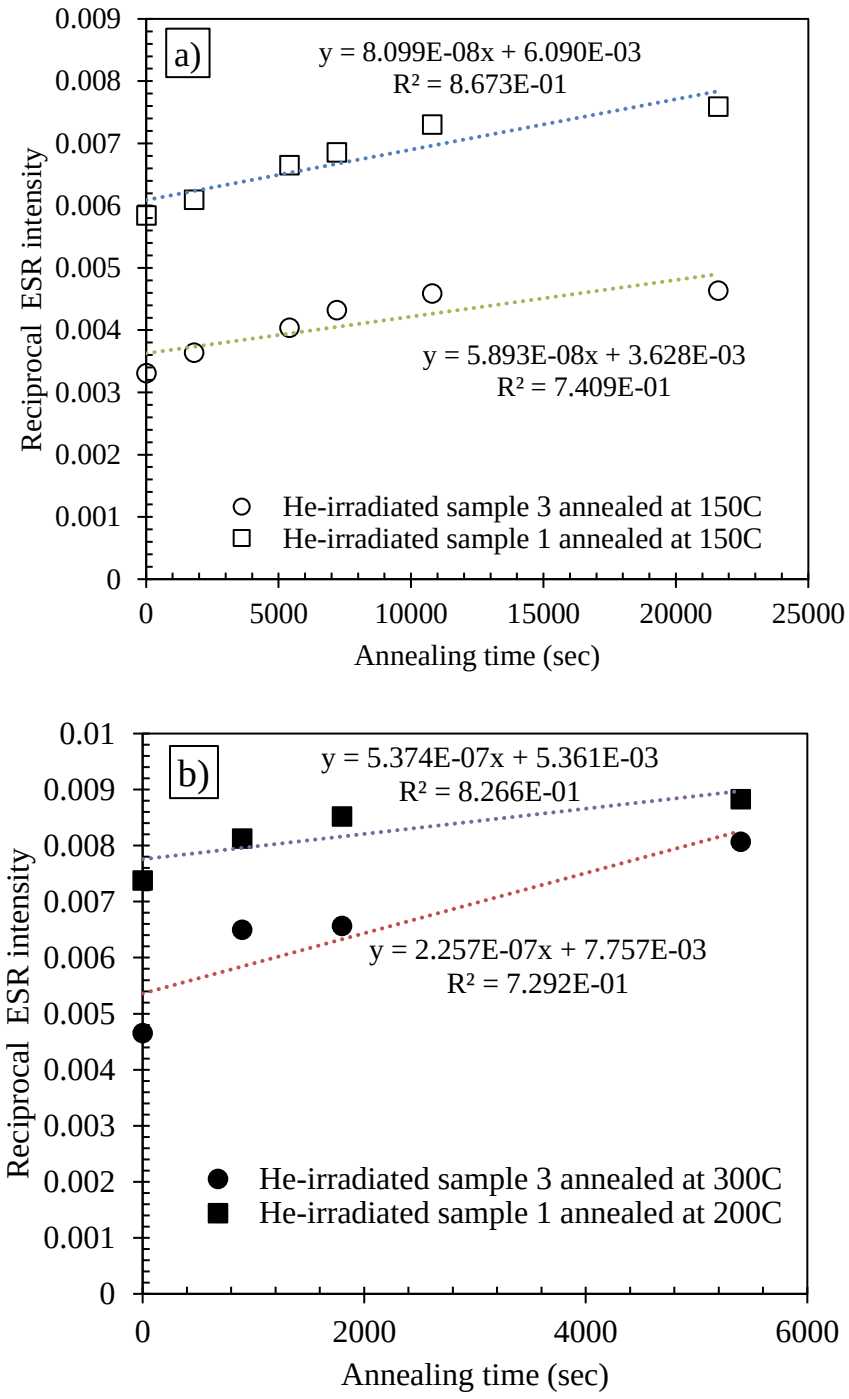

Fig.3- 22. Plots of the reciprocal concentrations versus annealing time showing the decay characteristics of E' centers isothermal annealed at different temperatures

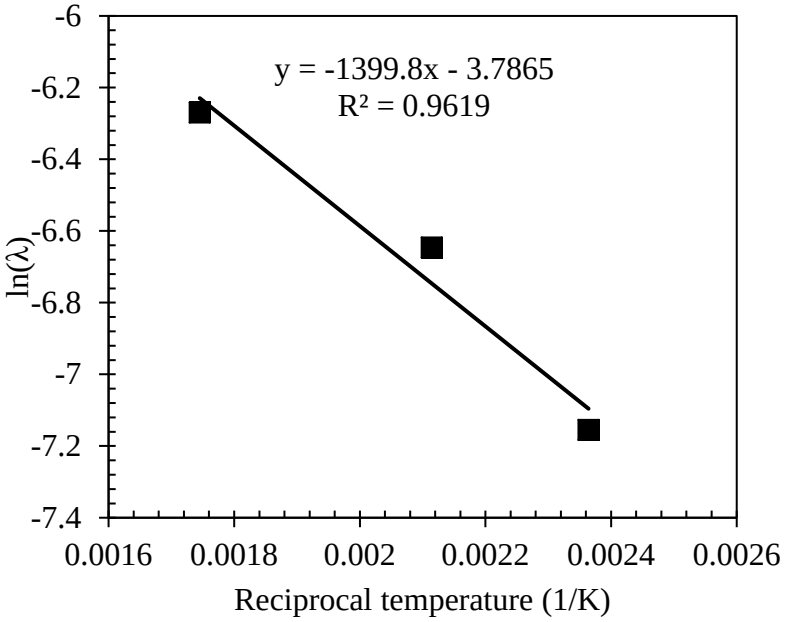

Fig.3- 23. Arrhenius plot of ln (λ) versus reciprocal temperature for E' centers. The calculated activation energy is around 0.11eV

3.3.3. Correlation between RIVE and mechanical properties

The correlation among structural changes (amorphization), RIVE, hardness, and Young's modulus changes due to irradiation can be described briefly as follows. In quartz, the amorphization occurred quickly, which was at the early stage of RIVE, and after amorphization still the RIVE existed. Young's modulus decreased gradually along the amorphization and volume expansion process. The hardness reduced with ion fluence, but almost reached saturation after amorphization. The RIVE of albite was mainly due to amorphization, though a small additional RIVE in albite was observed after amorphization. Young's modulus of albite decreased gradually along the RIVE. However, hardness was significantly reduced and almost saturated before amorphization. The RIVE of microcline was mainly due to amorphization. Despite the amorphization of microcline, Young's modulus remained nearly unchanged, whereas hardness change was similar to that of albite.

Although the fluence dependence of RIVE was similar among the three minerals studied, their expansion mechanisms differed. If we consider the RIVE, there would be a mixture of three processes that contribute to volume change:

(1) homogeneous expansion occurs in long-range scale due to the changing of angle between basic structures (e.g. SiO_4 tetrahedra), which is governed by the stress relaxation of the amorphous region;
(2) heterogeneous expansion by forming long-range structures (such as cavities) within the basic structures; and
(3) the changing of basic structure itself in short-range scale due to a change in the coordination number of atoms, this can be related to accumulation of point defects.

Fig.3- 24 illustrates the short-range and long-range changes that controlling the RIVE. In processes (1) and (2), the short-range structure (i.e., coordination number) is maintained. Though these processes will not be clearly distinguishable, each process will give a different effect on the property changes (i.e., density, hardness, and Young's modulus).

The change in Young's modulus of several glasses has been suggested to be proportional to packing density [139]. Krishnan et al. (2017) found that irradiation- and vitrification-induced disordering resulted in almost the same density and modulus change in several silicate minerals; and authors proposed a modulus–density scaling relationship, which is expressed as $E/E_O = (\rho/\rho_0)^n$, where the subscript "*o*" denotes the pristine state and *n* is the scaling exponent, which is *3* considering the increasing atomic porosity in amorphous silicates [78]. Based on that study, irradiation-induced amorphization will produce a homogenous structure because the vitrificated structure is generally homogenous, and the volume change

is mainly caused by the rearrangement of network on long-range scale while maintaining the basic structures. If the process (1) is the main cause of RIVE, the relationship between density and Young's modulus of minerals should follow the curve proposed by Krishnan [78]. For this purpose, the relative density was approximated from the step height [105–108] using $\rho/\rho_0 \approx \frac{1/(R+\Delta H)}{1/R}$. The comparison between experimental data and Krishnan fitting is presented in Fig.3-25. It showed that data of albite matched well with the scaling law. The data of quartz also matched immediately after amorphization; however, it deviated significantly when the RIVE continued and saturated at a high fluence. The data of microcline highly deviated after amorphization.

In silicate glasses, hardness has been described as a function of coordination number [88,140]. Hence, the reduction in hardness caused by radiation may be due to the changing of the silica tetrahedra (basic structures), which results in a change in the coordination of Si and O atoms. This process mainly occurs on a short-range scale before a full amorphization occurs. The hardness data suggest that the rearrangement of network, which could cause RIVE after the amorphization, has a negligible effect on the hardness of the three minerals. This is consistent with the results of Smedskjaer et al. [141], i.e., changes in the medium-range scale in aluminosilicate glass have a less prominent effect on hardness than those on a short-range scale. Therefore, hardness can be used as an "instant indicator" of basic structure changes in short-range scale, while Young's modulus can capture the change in long-range scale during and after the amorphization process.

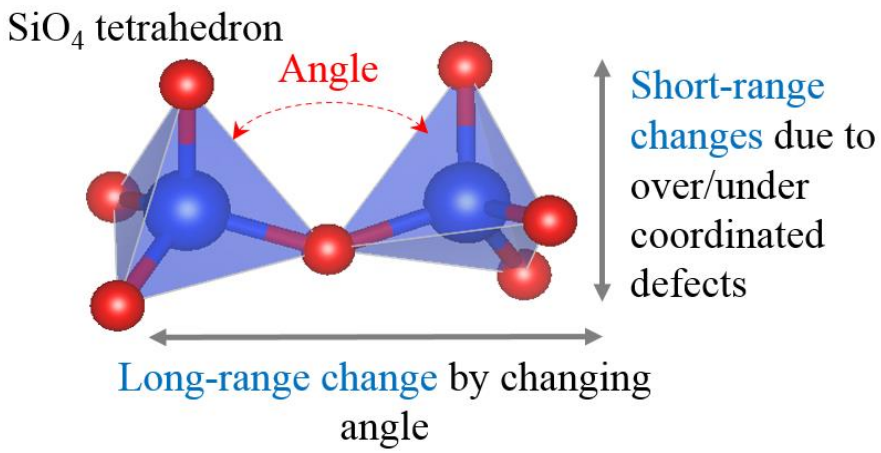

Fig.3- 24. Short-range and long-range changes governing RIVE mechanism in silicate mineral

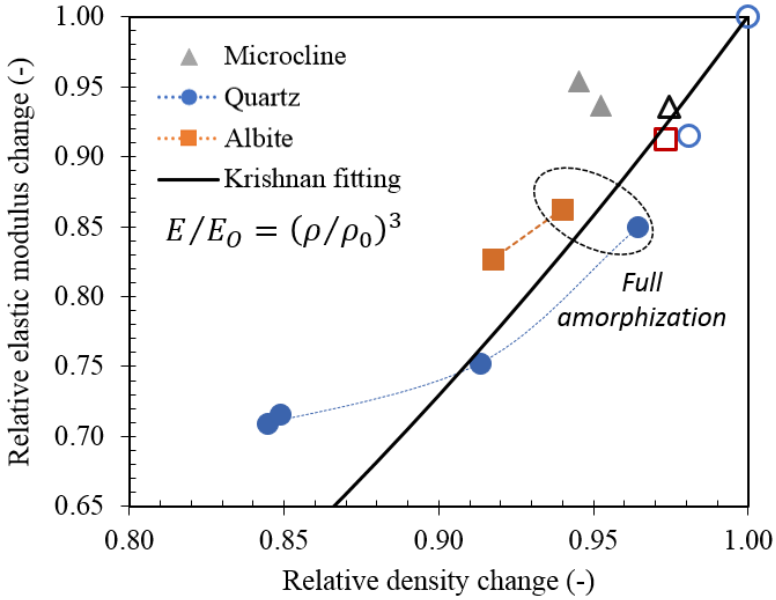

Fig.3- 25. Comparison between obtained experimental data and density–modulus scaling obtained by MD simulation [78]. *The open symbols indicate "before amorphization", whereas filled symbols indicate "after amorphization"*

The comparison suggests that RIVE in albite could follow the process (1); RIVE in quartz could be composed of (1) and (2); for microcline it seems to follow (3). The reason for this consideration is as follows:

- In microcline, the hardness decreased rapidly without full amorphization, which was presumed due to the change of coordination number, during the

accumulation of defects. There could be small rearrangement of network since there was no change in Young's modulus. This means the changing of basic structure itself could be the main cause of RIVE in microcline. This could be related to the large alkali ion K^+ in network would limit the flexibility of the silica network [25].

- In albite, Young's modulus changed along with RIVE and followed the scaling law, though hardness change was similar to that in microcline; this could be due to smaller alkali ionic size (Na^+) that sufficiently allows the flexibility for rearrangement of the network. This is evidenced when additional RIVE occurred after amorphization.
- In the case of quartz, it is obvious that the RIVE is due to the relaxation of amorphous regions since Young's modulus can capture the density change, however, the processes (2) and (3) may also contribute because of the formation of nanocavities. In amorphized minerals, the knock-on atom was far from the vacancy in the knock-on event due to the low density (the atoms did not move significantly by excitation; therefore, they can be recovered), defects such as nonbridging oxygens may attempt to stabilize the network with longer -Si-O- chains and form new rings; consequently, a pore structure will be formed. However, such cavities were not observed in feldspars because many alkali ions exist in them and charge transfer can occur easily; thus, the relaxation or balancing of the charge can prevent network changes, as illustrated in Fig.3-26.

Therefore, the alkali ions included in the silicate mineral can affect both the amorphization kinetics and the final (possibly metastable) amorphous structure.

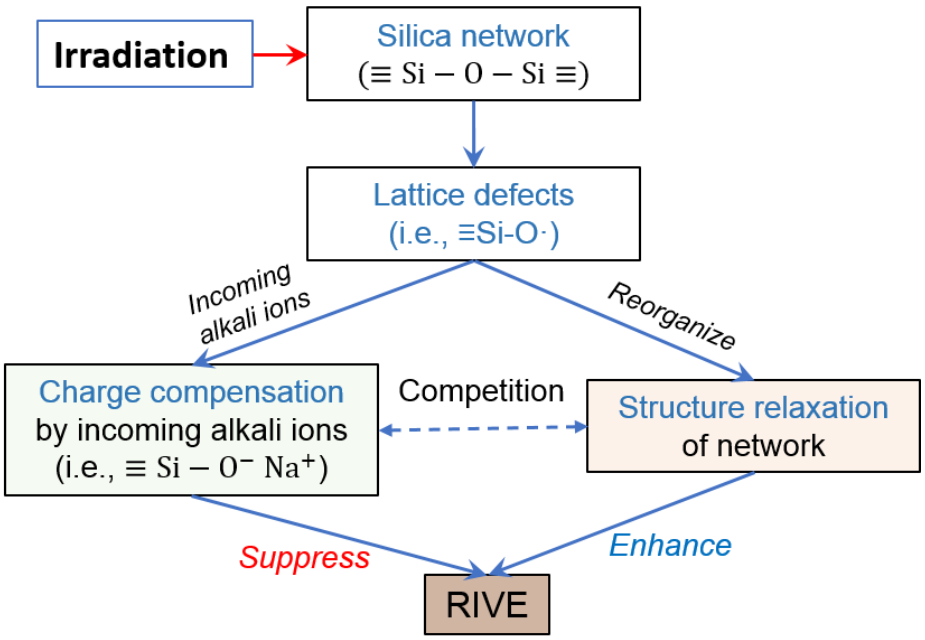

Fig.3- 26. The role of alkali ions on RIVE

3.4. Summary of findings

The volume change and mechanical properties of tectosilicate minerals under ion irradiation were evaluated. The main results obtained were as follows:

(1) By 2 MeV He^{2+} irradiation, swelling initiated at fluence around 1 x 10^{15} cm^{-2}. Increasing ion fluence, the step height linearly increased but did not reach saturation at 3.2 x 10^{16} cm^{-2}. Different ion fluxes (6.5 x 10^{11} - 6.4 x 10^{12} $cm^{-2}.s^{-1}$) did not change the onset of swelling fluence.

(2) Though ionization and knock-on displacement are found to contribute to RIVE, the ionization caused by knock-on atoms is not dominant in LWR's condition. Thus, RIVE can be described as a function of knock-on displacement, i.e., dpa and the amorphization dose can be determined at around 0.11dpa. This corresponds to about 6% of swelling.

(3) The changes in step heights under 3 MeV Si^{2+} irradiation in quartz and feldspars revealed that quartz was quickly amorphized and then exhibited

RIVE, RIVE of microcline and albite was mainly due to amorphization; however, a small additional RIVE in albite was observed after amorphization. After amorphization, cavity formation was observed in amorphized quartz, whereas it was not apparent in feldspar minerals.

(4) The change in hardness in the three minerals appeared to be a function of amorphization since no change occurred after a full amorphization. The Young's modulus decreased gradually with ion fluence and it seemed to correlate with RIVE.

(5) Since the change in hardness is related to changing of basic structure in short-range scale and the change in Young's modulus is associated with changing of angle between silica tetrahedra on a long-range scale, the results suggest a different mechanism of RIVE in three studied minerals: RIVE in albite mainly follows homogenous expansion (i.e., occurring in long-range scale); RIVE in quartz is a combination of homogenous and heterogenous expansion, while in microcline it follows the changing of basic structure (i.e., occurring in short-range scale). The associated change might be significantly related to the alkali ion content, which can affect both the amorphization kinetics and the final amorphous structure.

(6) The RIVE of amorphized silica is found to be governed by the radiation-induced viscous flow which increases with temperature. The activation energy was estimated at about 0.13eV, which may be related to the energy barrier for the rearrangement of the lattice network.

(7) It is found that the main defects measured by ESR are E'centers (i.e., oxygen vacancies). The activation energy for the recovery of E' centers is determined to be 0.11eV, which is found to be similar to that required energy for viscous flow under irradiation.

CHAPTER 4: REDEFINE REFERENCE LEVEL FOR CONCRETE DEGRADATION

4.1. Introduction

The change in mechanical properties of concrete under irradiation has been correlated with neutron fluence, and the threshold value was extracted. A reference level has been proposed as $1x10^{19}$ n/cm^2 by some regulatory body [21,37] based on the works of Hisdorf et al, (1978) [22]. However, the data exists large scatters, which are attributed to several sources such as differences in concrete composition, concrete's age, and test conditions (temperature), which have been previously recognized. Furthermore, the scatter is also due to the diversity of neutron spectrum and different energy cutoff. For instance, some researchers used fast neutrons (E>0.1 MeV), while some included slow/thermal neutrons. For this reason, the reference fluence could shift to lower or higher neutron fluence if the data is plotted by the different energy cutoff. A recent calculation by Igor Remec, 2016 has shown that damage for energy cutoff E>0.1 MeV contributes more than 95% of all atom displacements, thus authors recommended that E>0.1 MeV would be enough [142]; however, lower energy components (E<0.1MeV) may be significantly higher than high energies due to the moderation of neutron.

Since it has been confirmed in Chapter 3 that the main cause of RIVE is knock on displacement, in order to solve the issue of diversity of neutron spectrum, the neutron data can be normalized to the number of displacements. This chapter aims to clarify the damage contribution due to lower energy cutoff and to develop a correlation parameter for converting neutron fluence to dpa in order to redefine a new reference level considering the diversity of neutron spectrum.

4.2. Method for dpa estimation

The method of calculating dpa has been introduced in 1975 [143] and it has been considered as a standard parameter for the determination of radiation damage in metals. The dpa corresponds to the average number of displaced atoms in target material produced by given neutron fluence. Although it is difficult to accurately calculate dpa owing to the recovery of defects, this is a primary indicator of irradiation damage and it roughly estimates the amount of energy deposited by neutron that causes a permanently displaced of an atom from its original site. The dpa rate is generally calculated by the following equation

$$\text{dpa/s} = \int_{E_{min}}^{E_{max}} \boldsymbol{\Phi}(\boldsymbol{E_i}).\boldsymbol{\sigma_D}(\boldsymbol{E_i})\boldsymbol{dE_i} \quad \textit{Eq.4- 1}$$

where E_{max} is the maximum energy of the incoming particle; E_{min} is the minimum energy of the incoming particle; $\Phi(E_i)$ is the energy-dependent particle flux per unit energy; and $\sigma_D(E_i)$ is the energy-dependent displacement cross-section.

In practice, $\sigma_D(E_i)$ is roughly defined by scattering cross-section, $\sigma_s(E_i)$ multiplied by the number of displacements N_D. To calculate the total damage for a given neutron spectrum, neutron energy is discretized into individual energy group j (the method is adapted from [144]), then total damage rate dpa/s is calculated by the summation of damage rate in each energy group by

$$\boldsymbol{dpa/s} \cong \sum_{\boldsymbol{j=1}}^{\boldsymbol{N}} \boldsymbol{\sigma_{sj}}\, \boldsymbol{N_{Dj}} \boldsymbol{\varphi_j} \boldsymbol{\Delta E_j} \quad \textit{Eq.4- 2}$$

where σ_{sj} is the average scattering cross-section of Si and O in the *i* group; N_{Dj} is the average number of displaced defects produced by the neutron energy i group; φ_j is the neutron flux in the *i* group (unit as, $n.cm^{-2}.s^{-1}.eV^{-1}$) with the energy range, $\Delta E_j = E_{j-1} - E_j$ (unit as, eV).

In this calculation, quartz mineral was selected because it is considered an indicator of RIVE in concrete owing to having high susceptibility to RIVE [12] and highest

volume expansion under irradiation at a quite low irradiation dose compared with other silicate minerals [43]. For calculating the N_D, the displacement energy threshold for O and Si was chosen as 25eV, then N_D is calculated by SRIM code assuming different PKAs produced by neutron. The neutron scattering cross-section, σ_s of Si and O is obtained from JENDL-4.0 database (https://www-nds.iaea.org/exfor/).

For comparison, neutron flux spectrum in a test reactor and a simulated inner CBS surface (*data were digitalized from* [142]) are used. For test reactor condition, the flux is estimated at the reflector location. As seen in Fig.4- 1, for E > 0.01 MeV, the neutron flux contributes about 21% and 12% in whole spectrum for the test reactor and inner CBS, respectively. For E > 0.1MeV, these values reduced to 16% and 8%, respectively. Though the flux contribution differs, the reduction magnitude is the same (around 4-5%). The lower high neutron energy components at inner CBS may be due to the moderation of neutron as it passes through the reactor vessel.

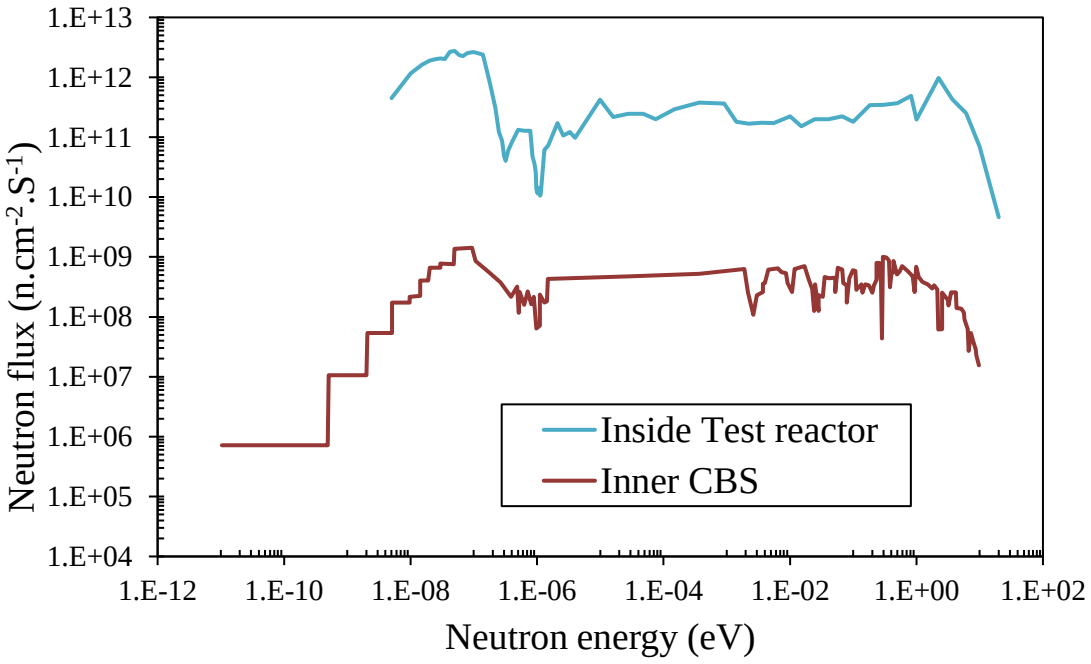

Fig.4- 1. Neutron flux spectrum for LVR-15 test reactor (Czech) and inner surface of CBS [142]

4.3. Results and discussion

4.3.1. Estimation of damage contribution

The results of damage rate estimation are given in Table 4- 1. Though the neutron flux spectrum in a test reactor is roughly three orders higher than that at inner CBS, there is almost no difference in damage contribution in two cases, except for neutron energies beyond 1 MeV. In detail, for E > 1 MeV, the produced damage is less than 50% of total atom displacements, while it is more than 99% for E > 0.01MeV regardless of different reactor types. In the case of E > 0.1MeV, the values are 98% and 95% for a test reactor and inner CBS, respectively. The results are consistent with the current report by Remec 2016 [142], who suggested the energy cutoff is E > 0.1 MeV. However, it is considered that the high energy component is moderated, and this will contribute to lower energy flux, thus we suggest that energy cutoff E > 0.01 MeV would be most appropriate based on the damage contribution >99% and the capability to produce displacement damage based on primary knock-on atom energy.

4.3.2. Correlation parameter

To consider different energy cutoffs produced from different neutron spectrums, we defined a correlation parameter D (dpa.cm^2) for each energy cutoff calculated by damage rate (dpa/s) divided by a neutron flux (cm^{-2}.s^{-1}), as given in Fig.4- 2. Having a correlation parameter, $D_{\mathrm{E}>E_0}$, the neutron fluence, $\phi_{\mathrm{E}>E_0}$ can be simply converted into dpa by the following relationship:

$$\mathbf{dpa} = D_{\mathrm{E}>E_0} \cdot \phi_{\mathrm{E}>E_0} \quad \text{.....Eq.4- 3}$$

Generally, the parameter D has the value between 10^{-22}-10^{-21} (dpa.cm^2) and D for a test reactor is higher than that for inner CBS, except for E > 1 MeV, as seen in Fig.4-

2. For E > 0 MeV, the value D is about 2.5 times higher, but it reduces to 1.5 and 1.2 times for E > 0.01 MeV and E > 0.1 MeV, respectively.

Table 4- 1. The neutron flux and calculated damage rate for LVR-15 test reactor and the inner surface of CBS.

	Test reactor condition			**Inner CBS condition**		
Energy cutoff (MeV)	**Neutron Flux ($n.cm^{-2}s^{-1}$)**	**Damage rate (dpa/s)**	**Correlation parameter D ($dpa.cm^2$)**	**Neutron Flux ($n.cm^{-2}s^{-1}$)**	**Damage rate (dpa/s)**	**Correlation parameter D ($dpa.cm^2$)**
E>0	1.34E+13	4.04E-09	3.01E-22	2.36E+10	2.83E-12	1.20E-22
E>0.01	2.80E+12	4.03E-09	1.44E-21	2.98E+09	2.81E-12	9.42E-22
E>0.1	2.18E+12	3.95E-09	1.81E-21	1.84E+09	2.68E-12	1.45E-21
E>1.0	1.15E+12	2.08E-09	1.81E-21	4.92E+08	9.41E-13	1.91E-21

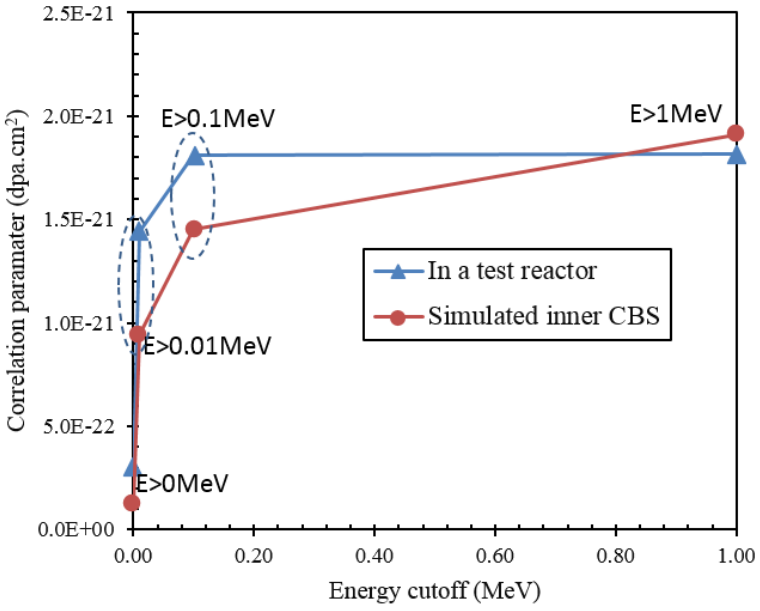

Fig.4- 2. The correlation parameter at different energy cutoffs in a test reactor and simulated inner CBS

Since neutron-irradiated quartz showed the RIVE initiated at around 3 x 10^{19} (n/cm^2) and reached maximum expansion at about 17.8% at 1x10^{20} (n/cm^2) for E > 0.01MeV in case of RT irradiation [48], assuming D = 1.44x10^{-21} due to lack of information about neutron spectrum, the onset of RIVE and critical dose for maximum expansion were determined to be 0.04dpa and 0.14 dpa, respectively. The obtained critical dose is close to that of the amorphization dose produced by ion irradiation, 0.11dpa (as result in Chapter 3).

To apply the correlation parameter to neutron-irradiated data, the concrete and mortar data has been reviewed and updated from comprehensive data compiled by K. G. Field, 2015 and new experimental data by Maruyama 2017, as shown in Fig.4-3. The large scatter makes it difficult to determine the reference level, particularly in the case of including thermal/slow neutrons, thus thermal/slow data was ignored in dpa calculation owing to the lack of information on thermal-to-fast neutron ratio. Fig.4- 4. shows the conversation into dpa for concrete and mortar data for energy cutoff E > 0.1MeV. The compiled data by Field showed large scatter up to 30% in early irradiation dose <0.02dpa, this source of scattering is not clear, but Maruyama 2017 suggested that the concrete strength can reduce by 15% due to drying impacts, thus other sources such as heterogeneity of concrete and test condition may contribute to the scatters. Therefore, it may be not due to the RIVE effect in aggregates at such low dose. As seen in Fig.4- 4, the reduction in concrete's strength starts at around one order lower (at 0.02dpa) than the complete amorphization dose of quartz mineral, this means that a different mechanism may contribute to concrete degradation, which mainly affects hydrated cement phase, such as by the radiation-induced drying before the RIVE will take place. Hence, the reduction of concrete

strength at >0.1dpa from Maruyama's data could be related to the RIVE, which is close to the amorphization dose of quartz mineral.

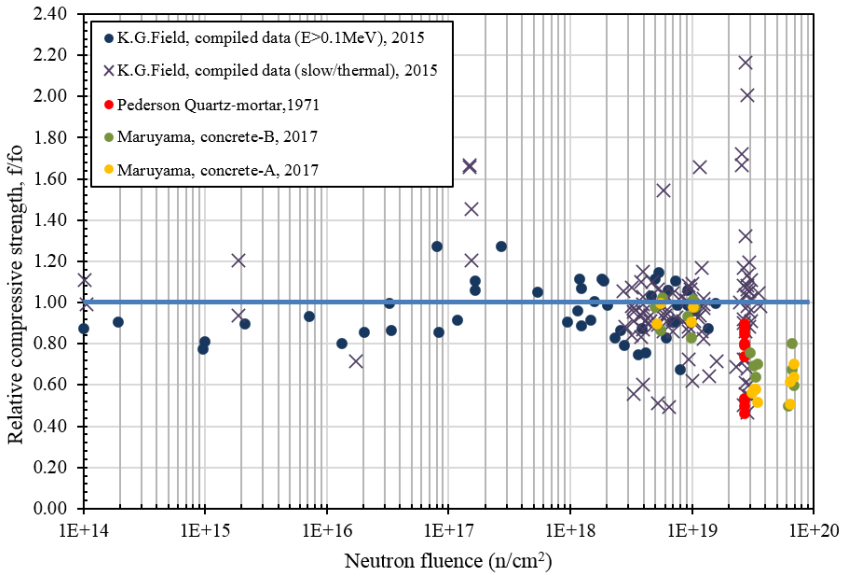

Fig.4- 3. Relative change of compressive strength of irradiated concrete and mortar with neutron fluence. Most of data are reported the fast neutron (E>0.1MeV) as marked by filled circular, except thermal/slow neutron as marked by cross. The irradiation temperature is less than 100°C.

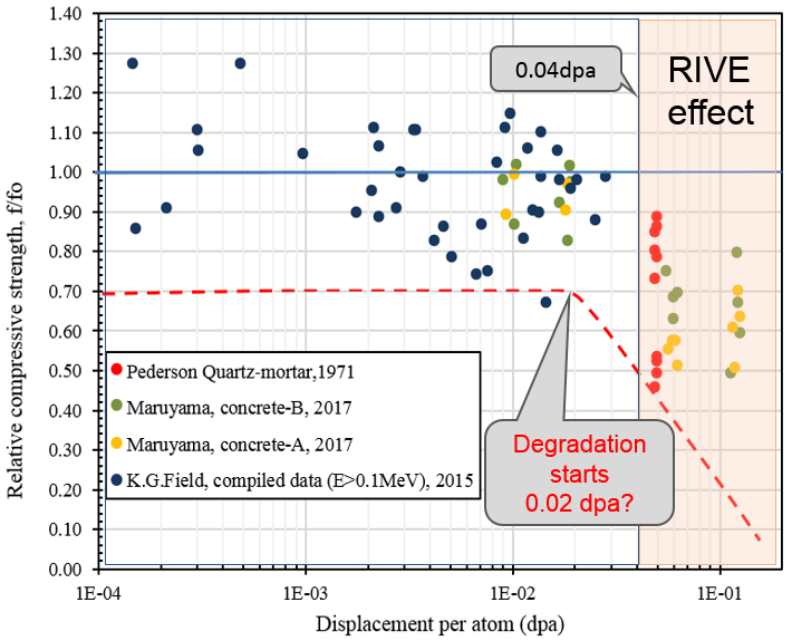

Fig.4- 4. Relative change of compressive strength of irradiated concrete and mortar with dpa. The degradation seems to start at around 0.02dpa.

4.3.3. Estimation of damaged layer after 60 years of operation

By obtaining a reference level at 0.02dpa, the representative neutron fluence profile through CBS wall [142] was digitalized and converted to dpa for the estimation of damage up to 60 years of operation with an effective factor of 0.9, as seen in Fig.4-5. The expected damage thickness is less than 4cm for reference level at 0.02dpa. Though this damaged layer would not significantly affect the functions of large CBS structure (a few meters), surface cracking can occur on the surface due to the effect of radiation-induced drying of cement paste and results in a gradient of humidity from the CBS surface [5]. This estimation indicates a potential degradation during LTO, thus a monitoring program of the existing CBS structure using nondestructive method is necessary.

It can be seen that the RIVE would not occur up to 60 years of operation because the maximum damage is lower than 0.04dpa level. However, this estimation is largely dependent on the input neutron spectrum, thus an accurate neutron fluence profile is required for a more appropriate estimation of damaged layer.

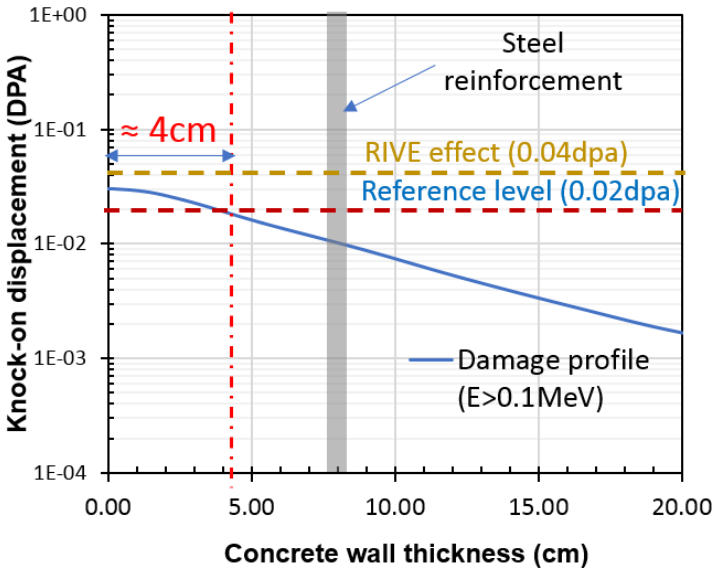

Fig.4- 5. Estimation of damaged layer after 60 years of operation

4.4. Summary of findings

Two cases of neutron flux spectra, a test reactor, and simulated inner CBS, were used to estimate the displacement damage rate and correlation parameter for normalizing different neutron spectrums:

(1) The calculated results showed the energy cutoff E>1MeV only contributes less than 50% of total displacement damage, while the neutron energies above 0.1MeV account for more than 95%, and almost covered all damage (>99%) for E>0.01MeV. This suggests E>0.01MeV would be appropriate because low energy neutron (0.01MeV< E <0.1MeV) also cause displacements and this energy range flux would be high due to neutron moderation.

(2) The correlation parameters extracted from the calculation have the value between 10^{-21} – 10^{-22} (dpa.cm^2) dependent on energy cutoff, which could be used to convert neutron fluence to dpa. The conversion of previous data showed the onset of RIVE and maximum RIVE of quartz under neutron irradiation are at 0.04dpa and 0.14 dpa, respectively. This estimation is close to the obtained critical dose for amorphization under ion irradiation. It is found that the onset of reduction in concrete's compressive strength is around 0.02dpa, this suggests a different mechanism could contribute to concrete degradation such as radiation-induced drying in cement paste before the RIVE in aggregates occurs.

CHAPTER 5: DEGRADATION OF CONCRETE BY HEAT AND EXAMINING THE POSSIBILITY OF ULTRASONIC WAVES FOR MONITORING CONCRETE STRUCTURE

5.1. Introduction

In the construction of nuclear facilities, concrete has been used as a structural material in radiation shielding walls and pedestals that may be exposed to a high temperature due to hot spots and severe accidents for a long duration. Though the studies on the influence of temperature on various types of concrete used in civil construction have been intensively studied in case of fire, concrete is a local product and has a diversity of aggregate types, thus it is difficult to utilize the current knowledge. Therefore, a similar mixture of concrete used in CBS was prepared and specimens were subjected to different temperatures for a long time to simulate the water loss and phase transformation effect on the properties of concrete. This chapter provides the results of physicochemical and mechanical changes, and structural assessment by ultrasonic-wave method using both P-wave and S-wave transducers in order to establish the correlation between the ultrasonic velocities and elastic modulus. This information is helpful for developing a remote nondestructive test method such as laser-induced ultrasonic waves [145] for application in monitoring the condition of CBS during LTO.

5.2. Results and discussion

5.2.1. Weight loss

Fig.5- 1 shows the effects of temperature on weight loss. The weight loss was calculated from the weight before and after heating. In the range of 25 - 105^{o}C, concrete lost weight rapidly due to the releasing of water in the capillary pores. Between 105^{o}C and 400^{o}C, the weight change is negligible because most of the

water was lost at 105ºC, and only physically bound water in fine pores of C-S-H gel may be dehydrated [146]. After 400ºC, the loss continued gradually due to the loss of chemically bound water in water-containing phases, including portlandite and C-S-H gel. The loss was about 4% and 8% after exposed to 400ºC and 800ºC, respectively.

By observing the surface condition in Fig.5- 2, no spalling (surface failure caused by internal pore pressure) occurred after heat treatments, and the concrete remained intact up to 800ºC. However, color changes and the formation of cracks can be observed on the concrete surface. At 105ºC, no visible cracks are observed. At 200ºC, a few visible cracks were detected, and they became pronounced in both size and density from 400ºC up to 800ºC. On the other hand, the color of concrete did not change when being heated to 200ºC. At 400ºC, it turned red and then turned whitish-grey between 600ºC and 800ºC. This phenomenon may be related to the change in chemical composition.

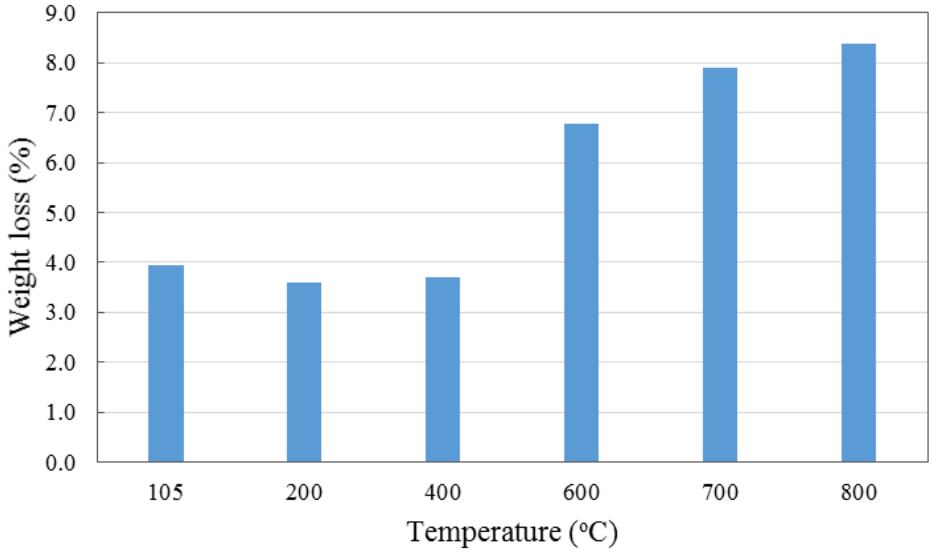

Fig.5- 1. The change of weight at different exposure temperatures

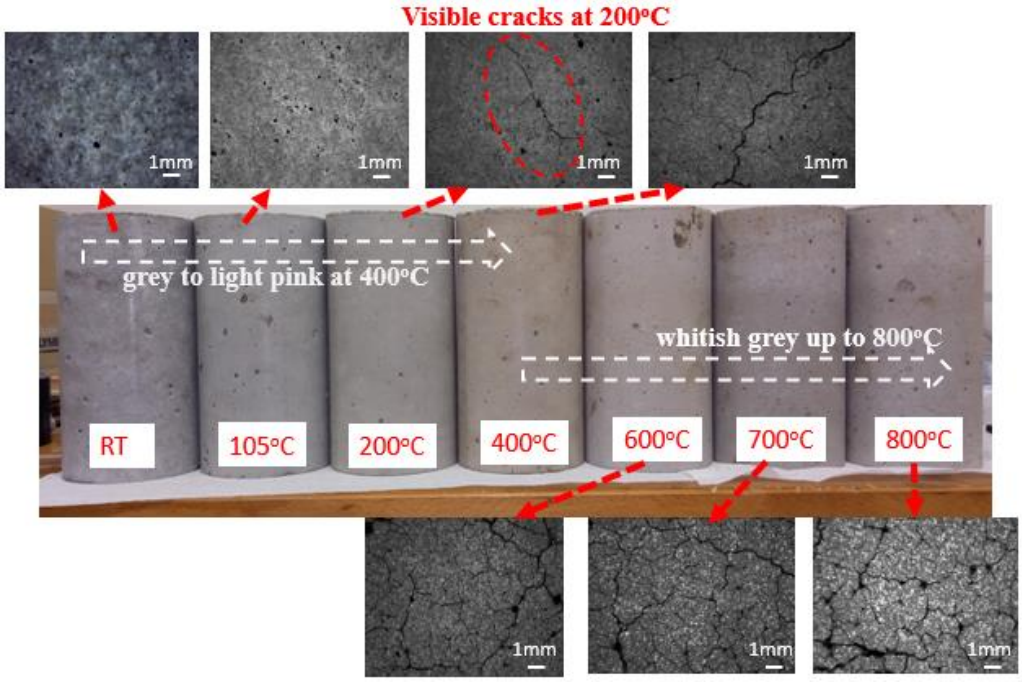

Fig.5- 2. Variation of concrete surface at different exposure temperatures

5.2.2. TG/DTA

Fig.5- 3 presents the TG/DTA curves of the specimen with no heat treatment and heated to 400°C. Similar to the XRD result (Sec. 5.2.3), different peaks of heat flow representing the chemical variations can be indexed in the DTA curve:

- The first peak between 100°C to 200°C can be attributed to the evaporation of water including bound water in some hydration products like C-S-H gel, the dehydration of C-S-H gel continues up to 500°C as reported by Castellote et al, (2004).
- The second peak appears at 400-500°C is associated with the decomposition of $Ca(OH)_2$.
- The small peak at around 570°C is an indicator of phase transformation of α - quartz into β-quartz, this may lead to cause cracking in aggregates containing siliceous (Grattan-Bellew, 1996).

- The last peak between 650°C and 800°C corresponds to the decomposition of C-S-H into β-C_3S + C_2S.

In the TG curve, the sample previously heated to 400°C had a small change of mass up to 400°C, this is probably caused by the reabsorbed moisture from the environment after the cooling process. Subsequently, the mass decreased suddenly at about 450°C. This confirmed that the concrete having a temperature history of 400°C still maintains $Ca(OH)_2$ in the cement paste. Thus the decomposition temperature of $Ca(OH)_2$ is at about 450°C.

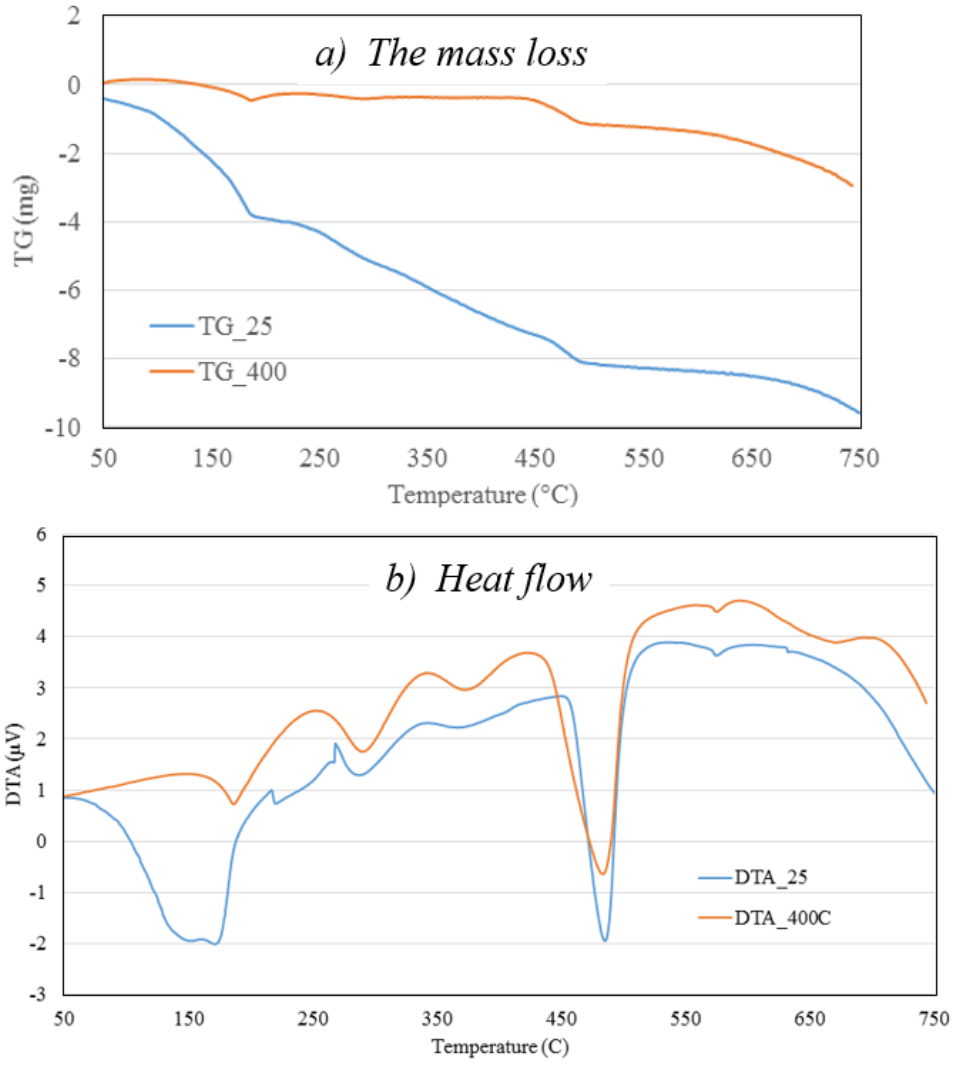

Fig.5- 3. DTA and TGA results for concrete samples without heating and heated to 400°C

5.2.3. Chemical changes

Fig.5- 4 presents the XRD diagram for the samples with various temperature exposures. At the initial stage, four crystalline phases can be identified (as Table 5-1.), including quartz (SiO_2), albite (coming from aggregates), portlandite ($Ca(OH)_2$ with d = 2.4 Å), and unhydrated <C_3S (tricalcium silicate) and β-C_2S> (with d = 2.6 - 2.8 Å corresponding to 2θ angles between 32 and 33°). It should be noted that it is difficult to distinguish between the peaks of β - C_2S and C_3S because their peaks have similar structures and diffraction angles [30]. In addition, the main hydrated phase, C-S-H gel cannot be indexed due to its amorphous nature, although C–S–H gel occupied about 60% of the cement paste [8]. It can be seen that almost no chemical decomposition of cement paste phases occurred below 400°C, while the peak of $Ca(OH)_2$ was reduced after 400°C. Between 700°C to 800°C, the peak intensity of < β-C_2S + C_3S > was intensified obviously. This is probably due to the transformation of the amorphous C-S-H phase into β-C_2S phase (i.e., crystalline phase), this is consistent with previous reports [9,146]. However, the peak of α-quartz was persistent up to 800°C, and we could not detect the β-quartz in the XRD patterns beyond 600°C even though there is an α - β transition in quartz at 573°C [28,146].

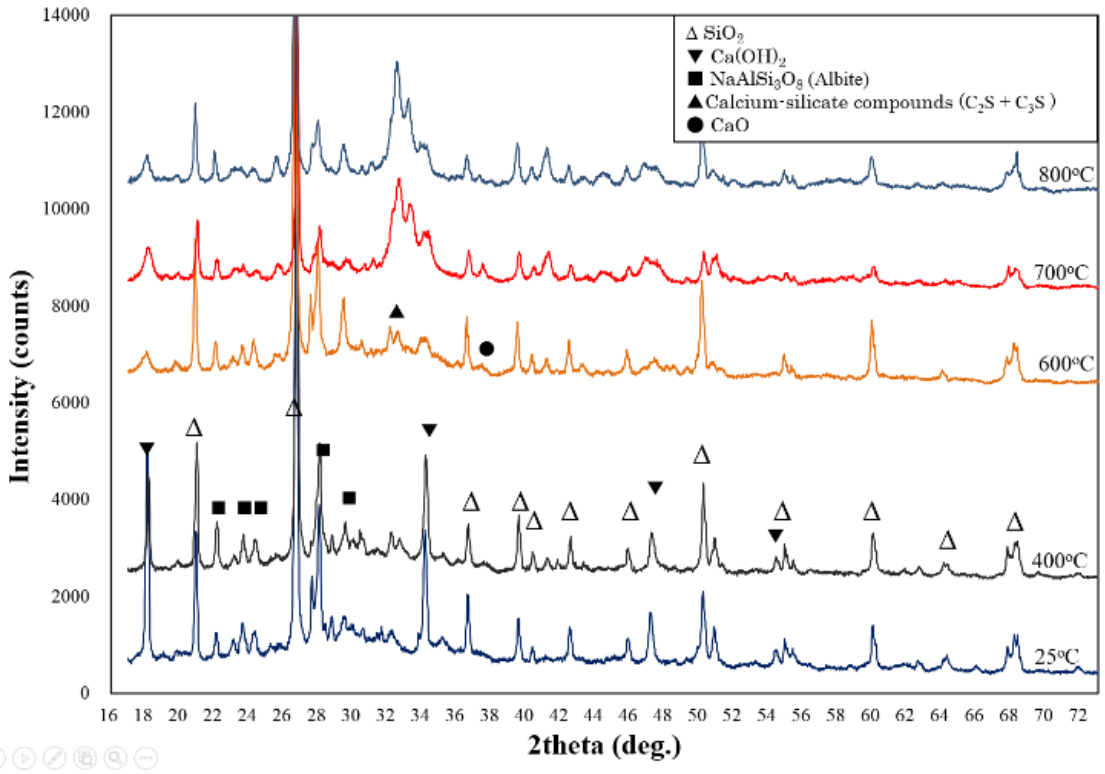

Fig.5- 4. Variation of chemical composition by using XRD

Table 5- 1. The variation of identified phases with temperatures

Exposed Temp.	**Identified Phases**			
	SiO_2 *(Quartz)*	$Ca_2(OH)_2$ *(Portlandite)*	$NaAlSi_3O_8$ *(Albite)*	C_3S and β-C_2S *(Unhydrated product)*
25°C	○	○	○	○
105°C	○	○	○	○
200°C	○	○	○	○
400°C	○	○	○	○
600°C	○	∀	○	○
700°C	○	∀	∀	Δ
800°C	○	∀	∀	Δ

○: *appeared*
∀: *decreased due to decomposition or recrystallization*
Δ: *increased*

5.2.4. Pore structures by MIP

The microstructure of heated concrete determined using mercury instruction porosimetry (MIP) is presented in Fig.5- 5. It should be noted that MIP enables access to pore diameters ranging from 3 nm to 360 µm, therefore MIP is a good technique for measuring the variations of the micro-pore structure. As seen in Fig.5-5a, as the temperature increased, the pore structure became coarser, which is consistent with the previous findings [30]. The coarsening of pore structure can be attributed to the releasing free water in capillary pores and microcracks that initiated as a result of incompatible deformation between cement paste and aggregates during heat treatment process [28,147].

Regarding pore size distribution, multiple peaks can be observed for temperatures between 25°C and 800°C, as shown in Fig.5- 5b. The pore size distribution curves can be divided into 3 types: (i) macropore (>0.3µm) represent the air voids and microcracks, (ii) capillary pores (0.3-0.02µm), and (iii) micropores (<0.02µm) corresponding to gel pores [147]. As seen in Fig.5- 5c, the variation of each pore type is different:

i. Macropore (>0.3µm): the macroporosity including microcracks porosity increased only slightly at 105°C, then significantly increased at 200°C (+29%), particularly after 400°C (+44%), this phenomenon could be related to the dehydration and the decomposition of portlandite (XRD and TG/DTA results).
ii. Capillary pore (0.3-0.02µm): the capillary porosity greatly increased as temperature raised. It increased by 155.8% at 105°C and then fluctuated between 107% and 163.2% until 600°C. Interestingly, beyond 700°C, the porosity increased more than 200%. This phenomenon could be associated with the decomposition of C-S-H into β-C_3S and C_2S, as seen in XRD and TG/DTA results.

iii. Micropore (<0.02μm): the porosity of the gel pore decreased at 105°C (-84.5%) and this decrease remained almost stable up to 800°C. This could be related to the collapse of C-S-H structure that expands the gel pore size at elevated temperature [147].

In summary, the total porosity of heated concrete samples was increased by 18% for temperatures ranging from 25 to 105°C. Subsequently, the total porosity remained stable up to 400°C and followed by a rapid increase from 400 to 800°C. Compared to that at the initial stage, the porosity was increased by 56% after exposure to 800°C. This phenomenon generally agrees with the density variation with temperature (Fig.5- 1).

5.2.5. Mechanical properties

Fig.5- 6 illustrates the change in mechanical properties of concrete that was exposed to different temperatures. The strength and modulus of elasticity had similar behaviors, which decreased continuously as temperature increased. The compressive strength of the unheated sample was about 41.8 MPa but suffered a significant reduction after thermal exposures. The residual strength remained about 75% of its original strength at 105°C, 43% at 400°C and 22.8% at 600°C. When concrete was heated to 800°C, only 13.3% of strength remained. Regarding the structural integrity, although after 336 hours heated to 200°C, the residual strength remained at about 25 MPa. This suggests that below 200°C, concrete still retains integrity in terms of the design strength (about 22 MPa [148]).

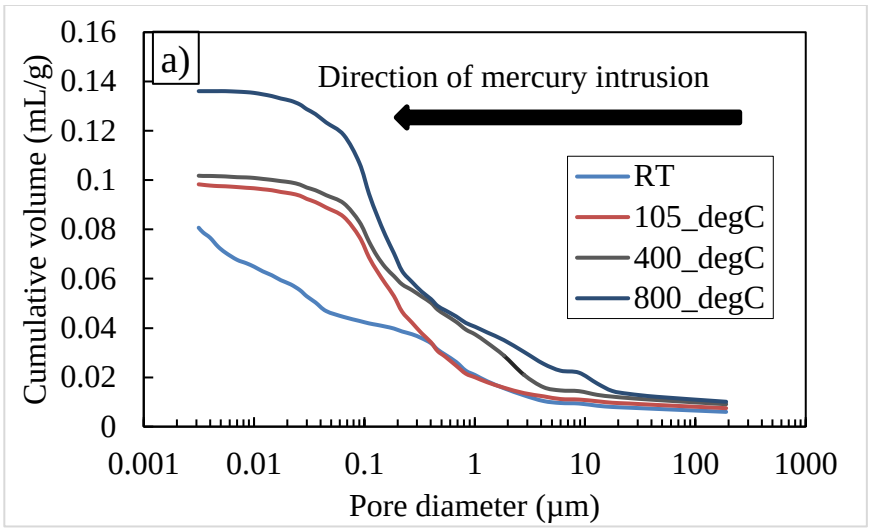

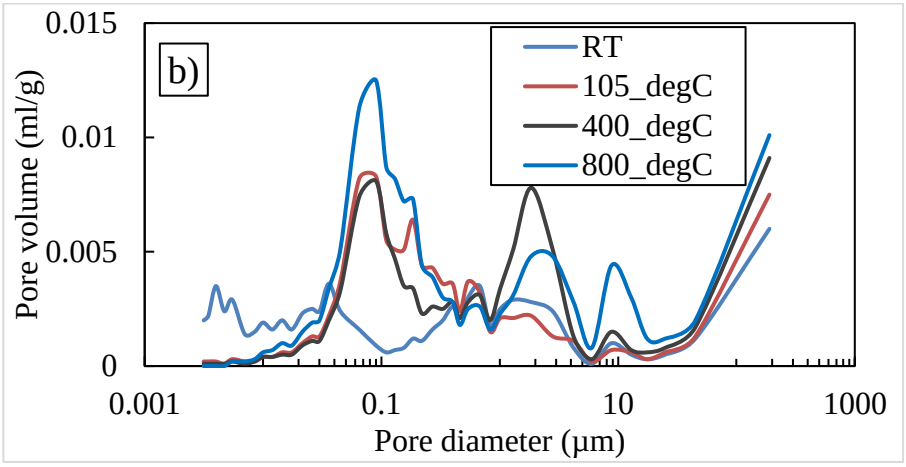

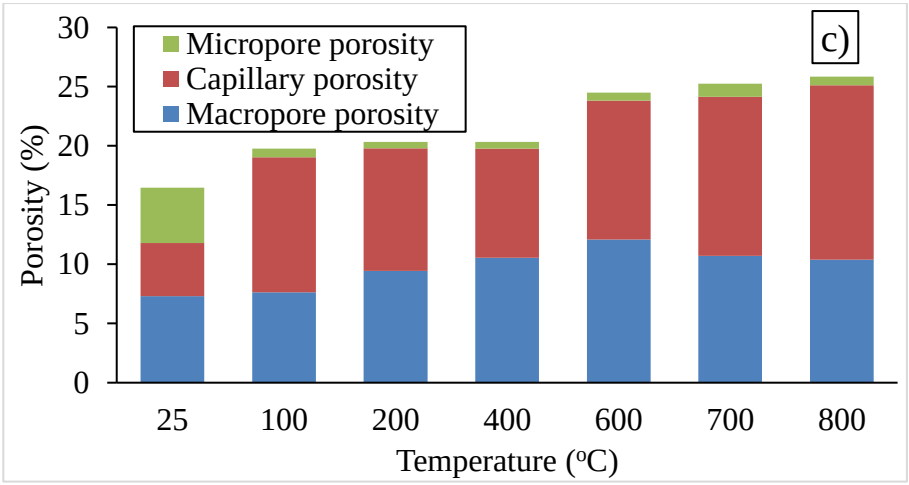

Fig.5- 5. Pore size distribution and porosity of concrete after exposure to elevated temperatures (a) cumulative pore volume (b) pore size distribution; and (c) porosity

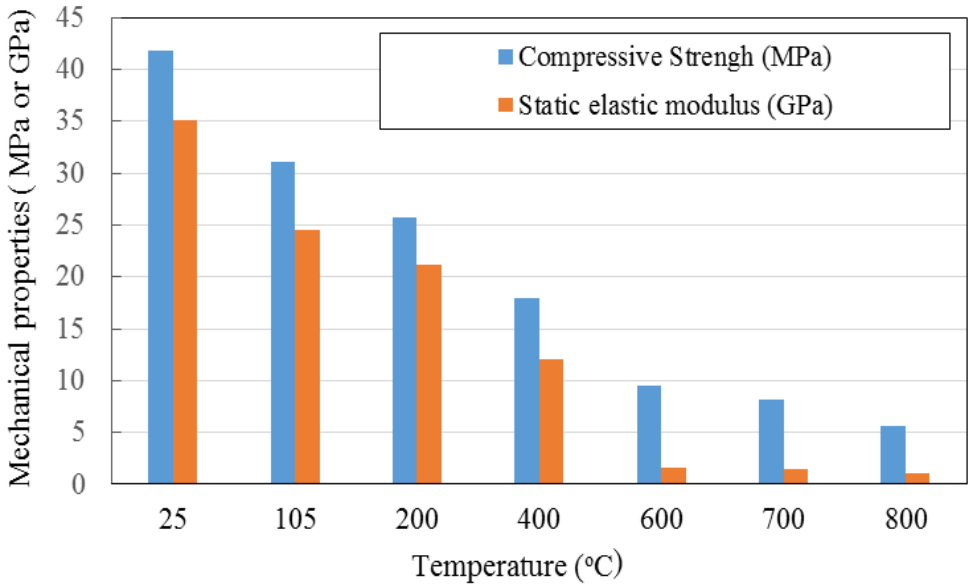

Fig.5- 6. The mechanical properties of concrete at different exposure temperatures

5.2.6. Variations of ultrasonic parameters

Fig.5- 7 gives the Hilbert transformation of the raw signals. The obtained envelope of the waveforms can distinguish the onset of S-wave and P-wave propagation. The first interruption indicates the onset of P-waves, as P-waves are the fastest among ultrasonic velocity components, while the second interruption indicates the onset of S-wave propagation. The onset times for S-waves were then used to calculate the S-wave velocities.

Fig.5- 8 shows the time-dependent signals obtained for thermal damage in concrete. Generally, the amplitudes of the waveforms decayed as exposure temperature increased. It can be seen that S-waves showed higher attenuation than P-waves at the temperature range of 25 – 200°C. This suggests S-waves are a better indicator of thermal damage due to capillary water loss than P-waves since they are more sensitive to matrix connectivity [149]. Beyond 200°C, amplitudes of both S- and P-waves decreased rapidly and became saturated between 600 and 800°C. In this temperature range, the signals can only be observed if magnified to 40dB, which

indicates significant damage in the concrete structure. Since the energy of the ultrasonic waves can be represented as the amplitude of the signal, as the level of damage increases, lower amplitude resulting from energy absorbed by the damaged concrete due to scattering and dispersion on scatterers (cracks or pores). This process redistributes the energy of the incident wave in all directions, and only a small amount of energy can remain in the forward direction that can reach the receiving transducer [150].

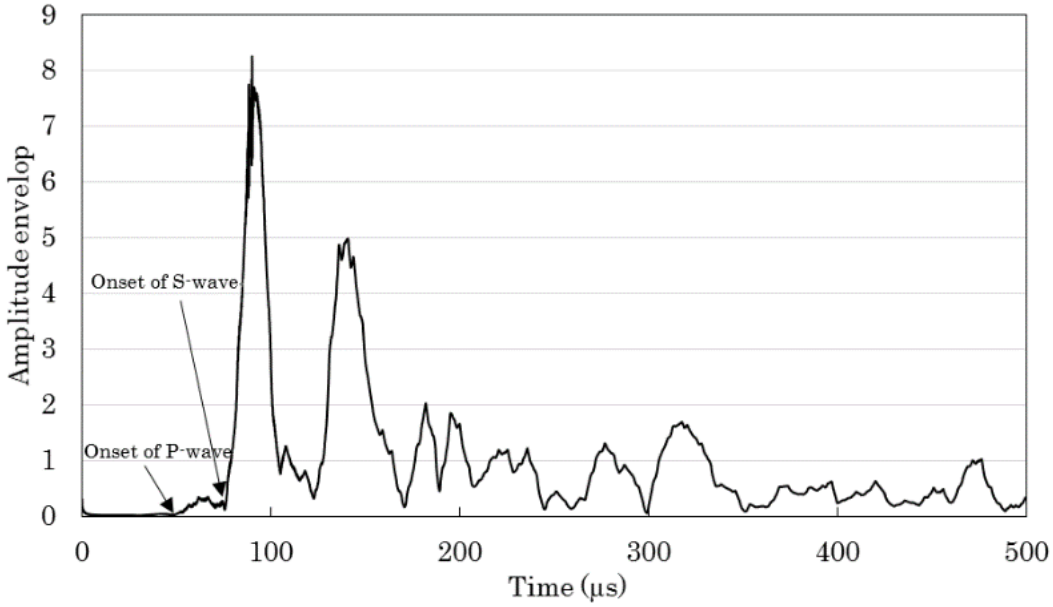

Fig.5- 7. Representative transformed signals of raw S-wave for unheated concrete

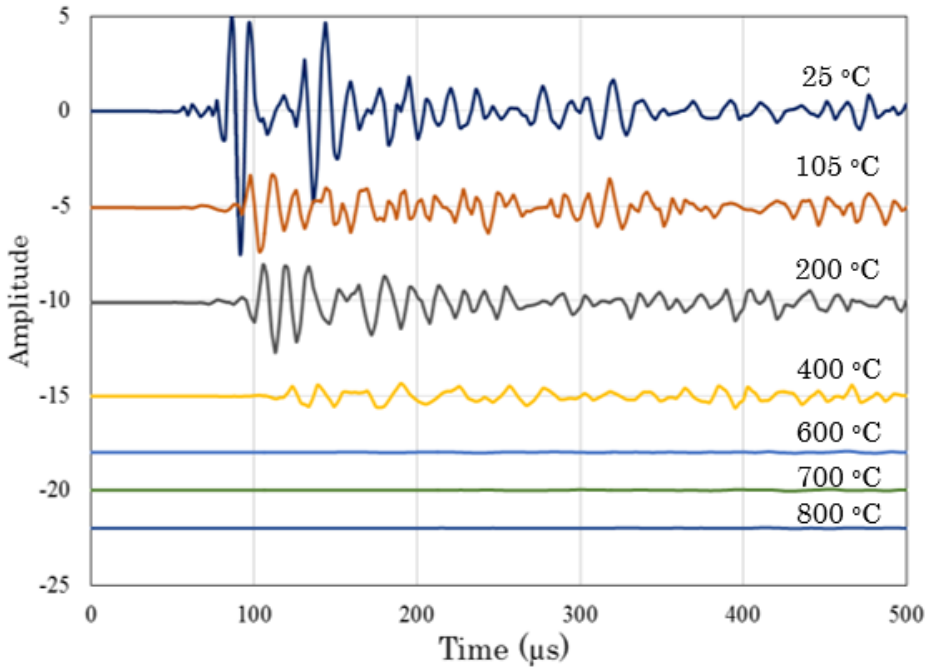

a) **S-waves**

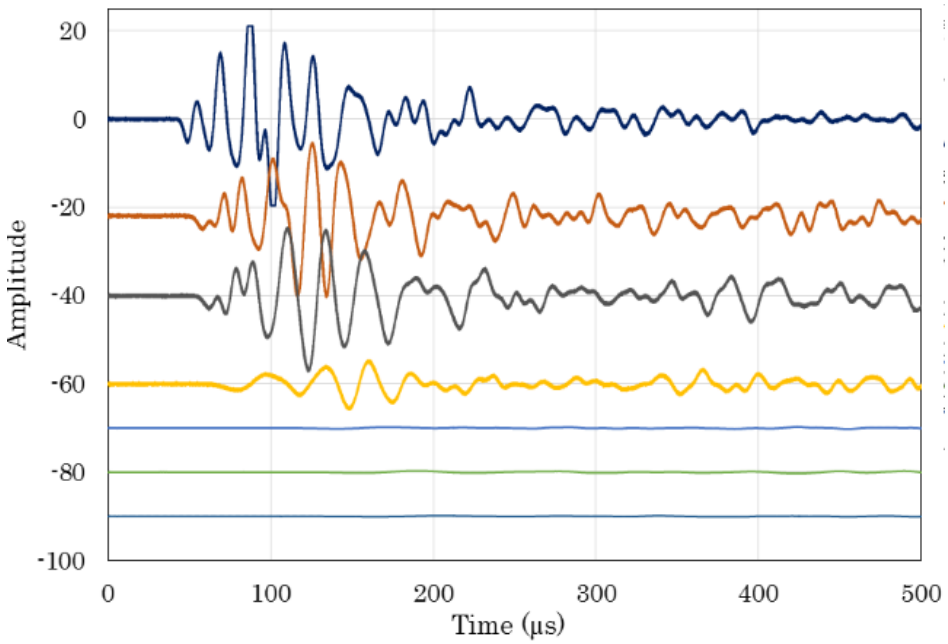

b) **P-waves**

Fig.5- 8. Time-dependent signals at different exposure temperatures

Fig.5- 9 presents the result of velocities of concrete before and after heating at high temperatures. For S-waves, it was possible to determine the rising instance when

concrete was exposed up to 400^{o}C. Beyond this, the signal is not stable due to high attenuation of the wave energy, with a reduction by > 98% of amplitude compared to that in unheated concrete. Since the vibration of particles in S-waves is perpendicular to the direction of propagation, it is very sensitive to cracks when the crack faces are perpendicular to the propagation direction. In this case, a high density of surface cracks above 400^{o}C could be associated with the reduction of S-wave velocity. In contrast, the rising time of P-waves was measurable up to 800^{o}C. As seen in Fig.5- 9, the velocities decreased continuously with the increasing temperatures. A rapid decrease was observed at 105^{o}C (-15.5%) and between 400 - 600^{o}C (-31.2% at 400^{o}C and -61.5% at 600^{o}C), this could be associated with the release of capillary water and decomposition of portlandite, respectively. Particularly, between 600^{o}C and 800^{o}C, the variation of pulse velocities was negligible; this is similar to the evolution of static elastic modulus.

The propagation of ultrasonic waves depends on the physical state of concrete. When concrete maintains integrity, the travel time required for the wave to reach the receiving transducer is shorter compared to that after subjected to high temperatures. Though numerous variables influence the ultrasonic velocity in ordinary concrete [151], microcracks and water content would contribute dominantly in this case. As a consequence of thermal damage, the porosity increases due to water loss, and formation of microcracks due to the deformation caused by the mismatch between the shrinkage of cement paste and expansion of aggregates [9,152], and this may contribute to reducing the incident wave energy and extending the traveling time, thus resulting in a reduction of velocity.

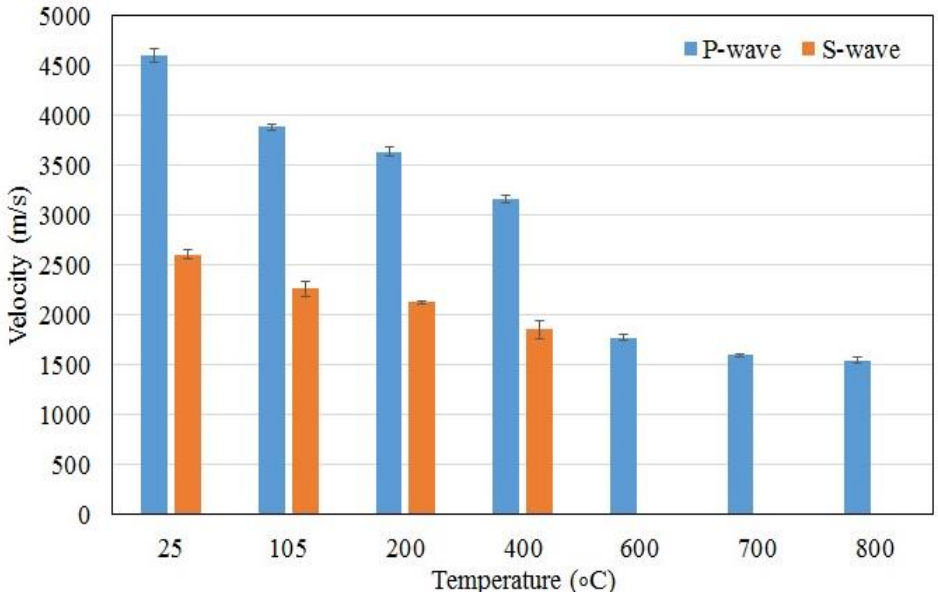

Fig.5- 9. The variations of velocities in concrete at different exposure temperatures

5.2.7. Correlation between ultrasonic velocity and static elastic modulus

As seen in Fig.5- 9, beyond 600°C both P-waves and S-waves significantly decayed due to heavily thermal damage, thus their velocities were difficult to be determined. This highlights the limitation of ultrasonic wave measurement techniques for monitoring concrete heavily damaged by heat, though it can be used to locate the most damaged area based on the loss of ultrasonic wave energy, which is in the form of amplitude. Fig.5- 10 presents the obtained relationship between the static elastic modulus (E_s) calculated from the stress-strain curve obtained by compression test using JIS A 1149-2001 and P-wave velocity calculated from transit time of P-waves. This correlation has the coefficient of determination R^2 near 1 (R^2 = 0.99) for concrete samples after heat treatment up to 400°C, corresponds to E_s which varies from about 12 to 35 GPa, as given by the Eq. 5-1:

$$\boldsymbol{V_P = 62.46\, E_s - 2366} \quad \text{.....Eq.5- 1}$$

Based on the velocity-elastic correlation, ultrasonic wave-based methods can be used to monitor the condition of the existing concrete structure during long-term operation.

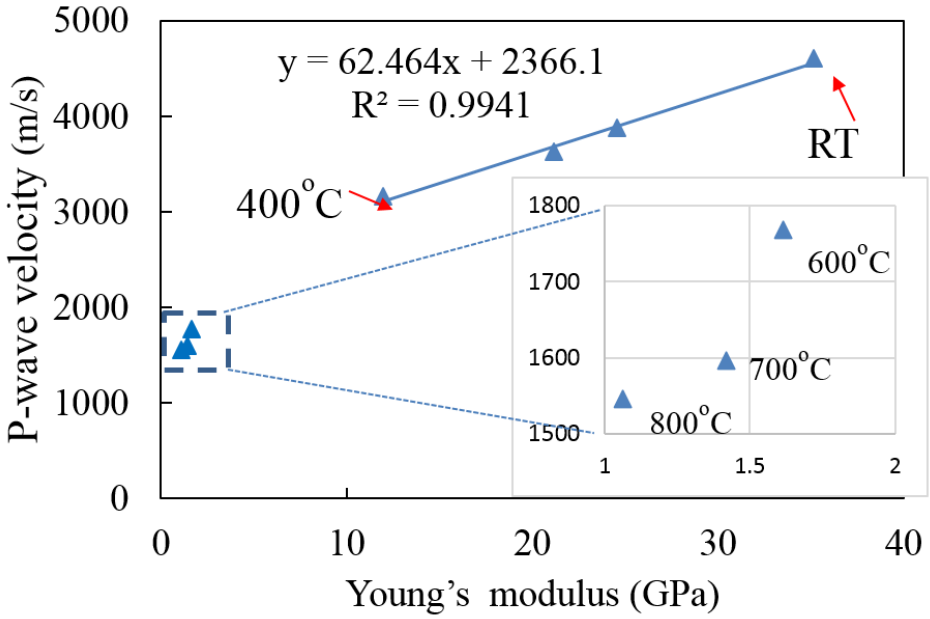

Fig.5- 10. Correlation between static and P-wave velocity (a) and with dynamic elastic modulus (b).

5.3. Summary of findings

- When concrete is subjected up to 800°C, the degradation can be clarified into two types: water loss-dominated degradation below 400°C and decomposition-dominated degradation beyond 400°C:

  (1) At 105°C, due to long time exposure, the strength, modulus of elasticity, and velocity reduced significantly. The mechanism is associated with the evaporation of capillary water. Between 105 and 400°C, the weight was almost not changed, but strength and elasticity continued to degrade. During this temperature exposure, the bound water in hydrated products is released, but due to the very fine structure change, it has a negligible effect on the weight.

In contrast, the water release had a great impact on mechanical properties and velocity.

(2) The surface cracks are very pronounced after 400°C, the loss of strength and ultrasonic velocity was gradual. Between 600°C to 800°C the concrete lost over 80% of its original strength, and the change in strength and ultrasonic velocity became saturated. The C-S-H structure may be dramatically decomposed due to the phase transformation into β-C_2S.

- The ultrasonic wave measurement method is sensitive to thermal degradation especially for damage caused by water content loss and the decomposition of portlandite at 105°C and between 400 to 600°C, respectively. S-wave is more sensitive to thermal damage than P-wave, resulting from water loss below 200°C.
- A linear correlation between ultrasonic velocity and static elastic modulus was obtained for concrete exposed to a temperature range of 25 to 400°C, corresponding to elastic modulus ranging from 12 - 35 GPa. Within this range, ultrasonic waves can be utilized to monitor the damage caused by water loss. After 400°C, concrete is severely damaged due to the formation of crack and the decomposition of cement paste phases, which cause the significant decay of the ultrasonic wave.

CHAPTER 6: CONCLUSION AND PERSPECTIVES

6.1. General conclusion

6.1.1. RIVE mechanism in model materials of aggregate

To clarify the degradation mechanism that contributes to the aging countermeasure against the degradation by neutron irradiation, ion irradiations in model materials of aggregate were carried out to identify the amorphization and extract the RIVE mechanism. The principal conclusions are as follow:

(1) Main cause of RIVE

Since RIVE is considered to be saturated at amorphization in current modeling codes, it is found that RIVE may continue after amorphization and the RIVE in concrete aggregate can be mainly indicated by the number of knock-on displacements in the Light Water Reactor's condition.

(2) RIVE mechanism

By studying the RIVE behavior in three minerals, the fluence dependence of RIVE was similar; however, the RIVE mechanisms of three minerals differed:

- Quartz was quickly amorphized and then exhibited RIVE. It is suggested that RIVE is a combination of homogenous expansion, heterogenous expansion, and basic structure changes.
- In albite, a small additional RIVE in albite was observed after amorphization; the RIVE mechanism is mainly through homogenous expansion.
- In microcline, no additional RIVE; the RIVE may be due to changing of the basic structure during accumulation of defects.

That different RIVE mechanism is related to alkali ions and ionic sizes.

Temperature is found to enhance the rate of RIVE with an activation energy of

structural relaxation of 0.13eV, this could be explained by the enhanced mobility of some defects that support the structural relaxation.

6.1.2. Redefine reference level based on the obtained results

Since quartz mineral is most common, easy to be amorphized, and has the highest RIVE, this mineral can be used as an indicator of the RIVE effect. To solve the issue of the diversity of neutron spectrum, correlation parameter was estimated and neutron-irradiated data can be normalized into the dpa.

(1) It is found that the RIVE in quartz due to neutron occurs at around 0.04dpa and reached maximum RIVE after 0.1dpa, thus it suggests the RIVE effect in concrete is beyond 0.04dpa.

(2) By normalizing the current neutron-irradiated data to dpa revealed that the compressive strength of concrete starts to decrease at around 0.02dpa, which is earlier than the onset of RIVE, this indicates radiation-induced drying could contribute before RIVE dominates. Thus, it suggests a new reference level at 0.02dpa for concrete degradation (this corresponds to neutron fluence of 1.0 x 10^{19} n/cm^2 with a correlation parameter 1.81 x 10^{-21} (dpa.cm^{-2})).

(3) The estimated damage for 60 years of operation in terms of knock-on displacements is less than 4cm from the inner CBS surface if the reference level is 0.02dpa; however, the RIVE will not occur during this period.

6.1.3. Degradation of concrete by heat and examining the possibility of ultrasonic wave for monitoring existing concrete structure

(1) Both physical-bound and chemical-bound water in concrete play important role in concrete. With approximately 4% physical-bound water loss (at 105^{o}C), compressive strength, and Young's modulus reduced by 30% of initial values. When chemical-bound water lost (up to 400^{o}C), mechanical properties

continued to reduce up to 60%. The reduction is not only due to water loss but also by the formation of microcracks, which is a result of cement paste shrinkage. The water-loss causes the pore structure coarsening and formation of cracks which may be a primary cause of strength's reduction.

(2) Ultrasonic wave method was demonstrated as a good tool to monitor the condition of concrete due to water loss with a linear correlation between velocity and Young's modulus in the range of 12GPa and 35GPa.

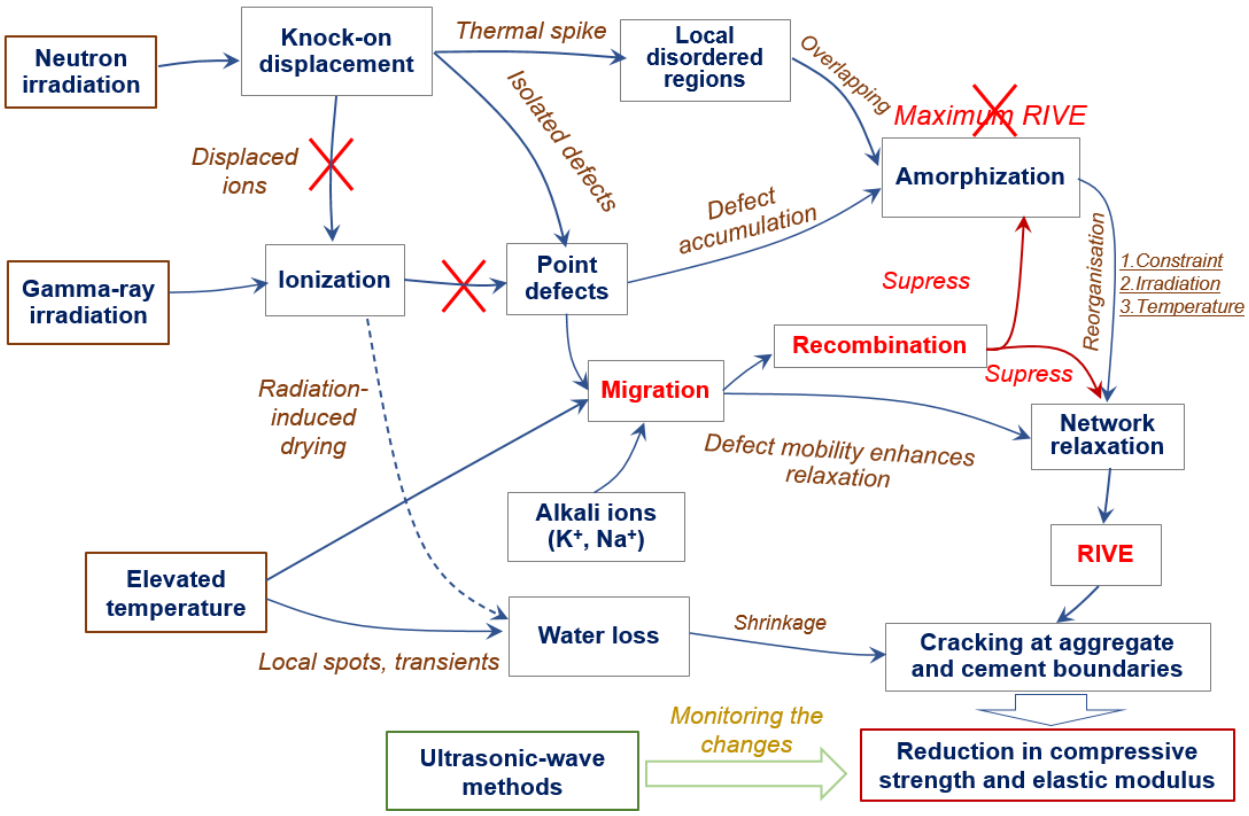

Fig.6- 1. Proposed degradation mechanism of concrete in nuclear facilities

6.2. Perspectives

Further studies are needed to develop a rate-theory-based model for describing the RIVE in concrete aggregate, though it is a difficult task due to the complexity of defect structure in silicate minerals as well as the effect of stress relaxation under physical constraint, which depends on the external stress, temperature, and additional irradiation.

Since the RIVE is an integrated swelling of a single mineral as a function of knock-on displacement, it is also important to evaluate the contribution of integrated RIVE on the reduction of concrete's strength and seismic resistance. As it has been found the viscous flow plays important role in stress relaxation during RIVE, this point is needed to be clarified in the case of polycrystalline aggregate in mesoscale modeling code.

It has been identified that the radiation-induced drying is important before the RIVE dominates, thus it is necessary to clarify the change in concrete's properties due to the long-term drying in more detail. In addition to that, the potential corrosion of steel reinforcement due to surface damage during LTO is also an important issue to be solved.

Further studies are needed to apply the ultrasonic-based method on monitoring existing structures such as Laser-ultrasonic.

REFERENCES

[1] Https://www.neimagazine.com/news/newsiaea-reports-on-nuclear-plant-operation-and-safeguards-7999314, IAEA reports on nuclear plant operation and safeguards, (n.d.).

[2] Https://www.eia.gov/todayinenergy/detail.php?id=18591, Nuclear Regulatory Commission resumes license renewals for nuclear power plants, (n.d.).

[3] T. Rosseel, J. Wall, G. Field, Y. Le~Pape, D. Naus, I. Remec, J. Busby, P. Bruck, Radiation Damage In Reactor Cavity Concrete, Fontevraud 8 - Contrib. Mater. Investig. Oper. Exp. to LWRs' Safety, Perform. Reliab. (2014).

[4] B. Barker, Nuclear Plant Life Extension: a strategic bridge, EPRIjournal. (2017). https://eprijournal.com/nuclear-plant-life-extension-a-strategic-bridge/#:~:text=The nuclear fleet in the,enabling operation to 60 years.

[5] T.M. Rosseel, I. Maruyama, Y. Le Pape, O. Kontani, A.B. Giorla, I. Remec, J.J. Wall, M. Sircar, C. Andrade, M. Ordonez, Review of the Current State of Knowledge on the Effects of Radiation on Concrete, J. Adv. Concr. Technol. 14 (2016) 368–383. https://doi.org/10.3151/jact.14.368.

[6] M. Suzuki, N. Nakagawa, S. Ito, T. Matsufuji, M. Uesaka, T. Hojo, I. Tamura, N. Sekimura, Toward Effective Nuclear Power Plant Ageing Management - On the Second Revision of the AESJ Code -, E-Journal Adv. Maint. 9 (2017) 168–172.

[7] H. Zhao, Q. Xiao, D. Huang, S. Zhang, Influence of Pore Structure on Compressive Strength of Cement Mortar, 2014 (2014).

[8] P.K. Mehta, P.J.M. Monteiro, Concrete: microstructure, properties, and materials, New York: McGraw-Hill, 2006.

[9] I. Hager, Behaviour of cement concrete at high temperature, Bull. Polish Acad. Sci. Tech. Sci. 61 (2013). https://doi.org/10.2478/bpasts-2013-0013.

[10] NUREG/CR-7171 ORNL/TM-2013/263, A Review of the Effects of Radiation on Microstructure and Properties of Concretes Used in Nuclear Power Plants, 2013.

[11] Y. Le Pape, J. Sanahuja, M.H.F. Alsaid, Irradiation-induced damage in concrete-forming aggregates: revisiting literature data through micromechanics, Springer Netherlands, 2020. https://doi.org/10.1617/s11527-020-01489-6.

[12] Y. Le Pape, M.H.F. Alsaid, A.B. Giorla, Rock-Forming Minerals Radiation-Induced Volumetric Expansion-Revisiting Literature Data, J. Adv. Concr. Technol. 16 (2018) 191–209. https://doi.org/10.3151/jact.16.191.

[13] K.G. Field, I. Remec, Y. Le Pape, Radiation effects in concrete for nuclear power plants - Part I: Quantification of radiation exposure and radiation effects, Nucl. Eng. Des. 282 (2015) 126–143. https://doi.org/10.1016/j.nucengdes.2014.10.003.

[14] Y. Le Pape, Light Water Reactor Sustainability Program IMAC Database v.0.3.-Concrete,

2017. http://www.osti.gov/scitech/.

[15] G. Igarashi, I. Maruyama, Y. Nishioka, H. Yoshida, Influence of mineral composition of siliceous rock on its volume change, Constr. Build. Mater. 94 (2015) 701–709. https://doi.org/10.1016/J.CONBUILDMAT.2015.07.071.

[16] I. Maruyama, O. Kontani, M. Takizawa, S. Sawada, S. Ishikawao, J. Yasukouchi, O. Sato, J. Etoh, T. Igari, Development of Soundness Assessment Procedure for Concrete Members Affected by Neutron and Gamma-Ray Irradiation, J. Adv. Concr. Technol. 15 (2017) 440–523. https://doi.org/10.3151/jact.15.440.

[17] M.J. Do, A.D. Chockie, Aging degradation of concrete structures in nuclear power plants, Ski Rep. 94 15. (1994).

[18] D.L. Fillmore, Literature Review of the Effects of Radiation and Temperature on the Aging of Concrete, 2004.

[19] V. Kodur, Properties of concrete at elevated temperatures, ISRN Civ. Eng. 2014 (2014). https://doi.org/10.1155/2014/468510.

[20] ANSI/ANS-6.4-1985, Guidelines on the Nuclear Analysis and Design of Concrete Radiation Shielding for Nuclear Power Plants, 1985.

[21] International Atomic Energy Agency, Assessment and nuclear power plant components management of ageing of major important to safety: Concrete containment buildings, 1998.

[22] H.K. Hilsdorf, J. Kropp, H.J. Koch, The Effects of Nuclear Radiation on the Mechanical Properties of Concrete, Spec. Publ. Am. Concr. Inst. 55 (1978) 223–254.

[23] B. Pomaro, A Review on Radiation Damage in Concrete for Nuclear Facilities: From Experiments to Modeling, Model. Simul. Eng. (2016). https://doi.org/10.1155/2016/4165746.

[24] D.J. Naus, NUREG/CR-6900 “The Effect of Elevated Temperature on Concrete Materials and Structures - A Literature Review, Oak Ridge National Laboratory.,” 2006.

[25] Q. Ma, R. Guo, Z. Zhao, Z. Lin, K. He, Mechanical properties of concrete at high temperature-A review, Constr. Build. Mater. (2015). https://doi.org/10.1016/j.conbuildmat.2015.05.131.

[26] M. Castellote, C. Alonso, C. Andrade, X. Turrillas, J. Campo, Composition and microstructural changes of cement pastes upon heating, as studied by neutron diffraction, Cem. Concr. Res. 34 (2004) 1633–1644. https://doi.org/10.1016/S0008-8846(03)00229-1.

[27] C.J. Fordham, I.J. Smalley, A simple thermogravimetric study of hydrated cement, Cem. Concr. Res. 15 (1985) 141–144. https://doi.org/10.1016/0008-8846(85)90019-5.

[28] P.E. Grattan-Bellew, Microstructural investigation of deteriorated Portland cement, Constr. Build. Mater. 10 (1995) 3–16.

[29] Y.N. Chan, G.F. Peng, M. Anson, Residual strength and pore structure of high-strength concrete and normal strength concrete after exposure to high temperatures, Cem. Concr. Compos. 21 (1999) 23–27. https://doi.org/10.1016/S0958-9465(98)00034-1.

[30] G.F. Peng, Z.S. Huang, Change in microstructure of hardened cement paste subjected to elevated temperatures, Constr. Build. Mater. (2008). https://doi.org/10.1016/j.conbuildmat.2006.11.002.

[31] S.K. Handoo, S. Agarwal, S.K. Agarwal, Physicochemical, mineralogical, and morphological characteristics of concrete exposed to elevated temperatures, n.d.

[32] O. Kontani, Y. Ichikawa, A. Ishizawa, M. Takizawa, O. Sato, Irradiation Effects on Concrete Structures, 2013. https://doi.org/10.1002/9781118536254.ch27.

[33] L. Douillard, J.P. Duraud, Amorphization of α-Quartz under Irradiation, J. Phys. III. 6 (1996) 1677–1687. https://doi.org/10.1051/jp3:1996206.

[34] P. Bouniol, A. Aspart, Disappearance of oxygen in concrete under irradiation: the role of peroxides in radiolysis, Cem. Concr. Res. 28 (1998) 1669–1681.

[35] T. Ichikawa, H. Koizumi, Possibility of radiation-induced degradation of concrete by alkali-silica reaction of aggregates, J. Nucl. Sci. Technol. (2002). https://doi.org/10.1080/18811248.2002.9715272.

[36] I. Pignatelli, A. Kumar, K.G. Field, B. Wang, Y. Yu, Y. Le Pape, M. Bauchy, G. Sant, Direct Experimental Evidence for Differing Reactivity Alterations of Minerals following Irradiation: The Case of Calcite and Quartz, Sci. Rep. 6 (2016) 20155. https://doi.org/10.1038/srep20155.

[37] U.S.NRC, Standard review plan for review of license renewal applications for nuclear power plants, 2017.

[38] V.G. Papadakis, Effect of composition , environmental factors and cement-lime mortar coating on concrete carbonation, Mater. Struct. 25 (1992) 293–304.

[39] F. Vodák, K. Trtík, V. Sopko, O. Kapičková, P. Demo, Effect of γ-irradiation on strength of concrete for nuclear-safety structures, Cem. Concr. Res. 35 (2005) 1447–1451. https://doi.org/10.1016/j.cemconres.2004.10.016.

[40] F. Vodak, V. Vydra, K. Trtik, O. Kapickova, Effect of gamma irradiation on properties of hardened cement paste, Mater. Struct. 44 (2011) 101–107. https://doi.org/10.1617/s11527-010-9612-x.

[41] I. Maruyama, S. Ishikawa, J. Yasukouchi, S. Sawada, R. Kurihara, M. Takizawa, O. Kontani, Impact of gamma-ray irradiation on hardened white Portland cement pastes exposed to atmosphere, Cem. Concr. Res. 108 (2018) 59–71. https://doi.org/10.1016/j.cemconres.2018.03.005.

[42] L. Skuja, N. Ollier, K. Kajihara, K. Smits, Creation of glass-characteristic point defects in crystalline SiO 2 by 2.5 MeV electrons and by fast neutrons, J. Non. Cryst. Solids. 505

(2019) 252–259. https://doi.org/10.1016/j.jnoncrysol.2018.11.014.

[43] R.K. Eby, R.C. Ewing, R.C. Birtcher, The amorphization of complex silicates by ion-beam irradiation, J. Mater. Res. 7 (1992) 3080–3102. https://doi.org/10.1557/JMR.1992.3080.

[44] A. Meldrum, S.J. Zinkle, L.A. Boatner, R.C. Ewing, Heavy-ion irradiation effects in the AB O4 orthosilicates : Decomposition , amorphization , and recrystallization, Phys. Rev. B. 59 (1999) 3981–3992.

[45] S.X. Wang, L.M. Wang, R.C. Ewing, R.H. Doremus, Ion beam-induced amorphization in MgO±Al2O3±SiO2. I. Experimental and theoretical basis, J. Non. Cryst. Solids. 238 (1998) 198–213. https://doi.org/10.1016/S0022-3093(98)00694-2.

[46] N.M.A. Krishnan, Y. Le Pape, G. Sant, M. Bauchy, Effect of irradiation on silicate aggregates' density and stiffness, J. Nucl. Mater. 512 (2018) 126–136. https://doi.org/10.1016/j.jnucmat.2018.10.009.

[47] L.W. Hobbs, F.W. Clinard, S.J. Zinkle, R.C. Ewing, Radiation effects in ceramics, J. Nucl. Mater. 216 (1994) 291–321. https://doi.org/10.1016/0022-3115(94)90017-5.

[48] V.N. Bykov, A. V. Denisov, V.B. Dubrovskii, V. V. Korenevskii, G.K. Krivokoneva, L.P. Muzalevskii, Effect of irradiation temperature on the radiation expansion of quartz, At. Energiya. 51 (1981) 593–595. https://doi.org/10.1007/BF01135758.

[49] S. Weissmann, K. Nakajima, Defect structure and density decrease in neutron-irradiated quartz, J. Appl. Phys. 34 (1963) 611–618. https://doi.org/10.1063/1.1729317.

[50] G. Mayer, J. Gigon, Effets des neutrons rapides sur quelques constantes physiques du quartz cristallin et de la silice vitreuse, J. Phys. Le Radium. 18 (1957) 109–114. https://doi.org/10.1051/jphysrad:01957001802010900.

[51] M.G. Jani, L.E. Halliburton, Point defects in neutron-irradiated quartz, J. Appl. Phys. 56 (1984) 942–946. https://doi.org/10.1063/1.334032.

[52] M.C. Wittels, The Lattice Expansion of Quartz Due to Fast Neutron Bombardment, 1952.

[53] M.C. Wittels, Structural behaviou of neutron irradiated quartz, Philos. Mag. 2 (1957) 1445–1461. https://doi.org/10.1080/14786435708241190.

[54] U. Katenkamp, H. Karge, R. Prager, Radiation Effects Radiation defects and optical properties of ion implanted silicon dioxide, Radiat. Eff. 48 (1980) 31–34. https://doi.org/10.1080/00337578008209224.

[55] C. Trautmann, M. Boccanfuso, A. Benyagoub, S. Klaumünzer, K. Schwartz, M. Toulemonde, Swelling of insulators induced by swift heavy ions, Nucl. Instruments Methods Phys. Res. Sect. B. 191 (2002) 144–148. https://doi.org/10.1016/S0168-583X(02)00533-5.

[56] S. Klaumünzer, Ion tracks in quartz and vitreous silica, in: Nucl. Instruments Methods

Phys. Res. Sect. B Beam Interact. with Mater. Atoms, 2004. https://doi.org/10.1016/j.nimb.2004.05.014.

[57] A. Meftah, F. Brisard, J.M. Costantini, E. Dooryhee, M. Hage-Ali, M. Hervieu, J.P. Stoquert, F. Studer, M. Toulemonde, Track formation in SiO2 quartz and the thermal-spike mechanism, Phys. Rev. B. 49 (1994) 12457–12463. https://doi.org/10.1103/PhysRevB.49.12457.

[58] H. Fischer, G. Götz, H. Karge, Radiation Damage in Ion-Implanted Quartz Crystals Part I: Nuclear and Electronic Energy Deposition, Phys. Status Solidi. 76 (1983) 249–256.

[59] R.A.B. Devine, E. Dooryhee, J.P. Duraud, L. Douillard, F. Jollet, Radiation damage produced in quartz by energetic ions, Radiat. Eff. Defects Solids. (2007). https://doi.org/10.1080/10420159208228862.

[60] F. Harbsmeier, W. Bolse, Ion beam induced amorphization in α quartz, J. Appl. Phys. 83 (1998) 4049–4054. https://doi.org/10.1063/1.367224.

[61] C.B. Carter, D.L. Kohlstedt, Electron irradiation damage in natural quartz grains, Phys. Chem. Miner. 7 (1981) 110–116. https://doi.org/10.1007/BF00308226.

[62] I. Maruyama, S. Muto, Change in Relative Density of Natural Rock Minerals Due to Electron Irradiation, J. Adv. Concr. Technol. 14 (2016) 706–716. https://doi.org/10.3151/jact.14.706.

[63] D.G. Howitt, H.W. Chan, E.R. Vance, J.F. Denatale, P.J. Hood, D.A. Thompson, A comparison between electron and ion damage in quartz, Radiat. Eff. Defects Solids. 112 (1990) 39–45. https://doi.org/10.1080/10420159008213028.

[64] M.A. Stevens Kalceff, M.R. Phillips, Electron irradiation induced outgrowths from quartz, J. Appl. Phys. (1995). https://doi.org/10.1063/1.359499.

[65] N.M.A. Krishnan, B. Wang, Y. Le Pape, G. Sant, M. Bauchy, Irradiation- vs. vitrification-induced disordering: The case of α -quartz and glassy silica, J. Chem. Phys. 146 (2017) 204502. https://doi.org/10.1063/1.4982944.

[66] S. Zhang, O.H. Pakarinen, M. Backholm, F. Djurabekova, K. Nordlund, J. Keinonen, T.S. Wang, Absence of single critical dose for the amorphization of quartz under ion irradiation, J. Phys. Condens. Matter. 30 (2018) 015403. https://doi.org/10.1088/1361-648X/aa9868.

[67] B. Wang, Y. Yu, I. Pignatelli, G. Sant, M. Bauchy, Nature of radiation-induced defects in quartz, J. Chem. Phys. 143 (2015) 024505. https://doi.org/10.1063/1.4926527.

[68] B.J. Cowen, M.S. El-Genk, Estimates of point defect production in α-quartz using molecular dynamics simulations, Model. Simul. Mater. Sci. Eng. 25 (2017). https://doi.org/10.1088/1361-651X/aa6f4f.

[69] N.M.A. Krishnan, B. Wang, Y. Yu, Y. Le Pape, G. Sant, M. Bauchy, Enthalpy landscape dictates the irradiation-induced disordering of quartz, Phys. Rev. X. (2017).

https://doi.org/10.1103/PhysRevX.7.031019.

[70] L. Douillard, J.P. Duraud, Swift heavy ion amorphization of quartz -a comparative study of the particle amorphization mechanism of quartz, Nucl. Instruments Methods Phys. Res. B. 107 (1996) 212–217.

[71] C. Trautmann, J.M. Costantini, A. Meftah, K. Schwartz, J.P. Stoquert, M. Toulemonde, Swelling of SiO2 quartz induced by energetic heavy ions, Mat. Res. Soc. Symp. Proc. 504 (1998) 123–128.

[72] M. Toulemonde, S.M.M. Ramos, H. Bernas, C. Clerc, B. Canut, J. Chaumont, C. Trautmann, MeV gold irradiation induced damage in α-quartz: Competition between nuclear and electronic stopping, Nucl. Instruments Methods Phys. Res. B. 178 (2001) 331–336. https://doi.org/10.1016/S0168-583X(00)00496-1.

[73] W. Primak, Fast-neutron-induced changes in quartz and vitreous silica, Phys. Rev. 110 (1958) 1240–1254. https://doi.org/10.1103/PhysRev.110.1240.

[74] M. Avrami, Granulation, phase change, and microstructure kinetics of phase change. III, J. Chem. Phys. 9 (1941) 177–184. https://doi.org/10.1063/1.1750872.

[75] Y. Le Pape, A. Giorla, J. Sanahuja, Combined Effects of Temperature and Irradiation on Concrete Damage, J. Adv. Concr. Technol. 14 (2016) 70–86. https://doi.org/10.3151/jact.14.70.

[76] H. Scholze, Glass, 1990.

[77] W.H. Zachariasen, The atomic arrangement in glass, J. Am. Chem. Soc. (1932). https://doi.org/10.1021/ja01349a006.

[78] N.M.A. Krishnan, R. Ravinder, R. Kumar, Y. Le Pape, G. Sant, M. Bauchy, Density–stiffness scaling in minerals upon disordering: Irradiation vs. vitrification, Acta Mater. 166 (2019) 611–617. https://doi.org/10.1016/j.actamat.2019.01.015.

[79] G.R. Lumpkin, R.C. Ewing, Hardness and elastic modulus of zircon as a function of heavy-particle irradiation dose: I. In situ α-decay event damage, Radiat. Eff. Defects Solids. 118 (1991) 393–403. https://doi.org/10.1080/10420159108220764.

[80] W.J. Weber, R.C. Ewing, C.R.A. Catlow, T. Diaz De La Rubia, L.W. Hobbs, C. Kinoshita, H. Matzke, A.T. Motta, M. Nastasi, E.K.H. Salje, E.R. Vance, S.J. Zinkle, Radiation effects in crystalline ceramics for the immobilization of high-level nuclear waste and plutonium, J. Mater. Res. 13 (1998) 1434–1484. https://doi.org/10.1557/JMR.1998.0205.

[81] S.J. Bull, T.F. Page, Effects of ion implantation on the hardness and friction behaviour of soda-lime silica glass, J. Mater. Sci. 27 (1992) 3605–3616. https://doi.org/10.1007/BF00351545.

[82] O. Gedeon, K. Jurek, I. Drbohlav, Changes in surface morphology of silicate glass induced by fast electron irradiation, J. Non. Cryst. Solids. 353 (2007) 1946–1950.

https://doi.org/10.1016/j.jnoncrysol.2007.01.058.

[83] T. Gavenda, O. Gedeon, K. Jurek, Structural and volume changes and their correlation in electron irradiated alkali silicate glasses, Nucl. Instruments Methods Phys. Res. B. 397 (2017) 15–26. https://doi.org/10.1016/j.nimb.2017.02.026.

[84] J. Zemek, P. Jiricek, O. Gedeon, B. Lesiak, A. Jozwik, Electron irradiated potassium-silicate glass surfaces investigated by XPS, J. Non. Cryst. Solids. 351 (2005) 1665–1674. https://doi.org/10.1016/j.jnoncrysol.2005.04.059.

[85] D. V. McCaughan, R.A. Kushner, V.T. Murphy, Ion Neutralization Processes at Insulator Surfaces and Consequent Impurity Migration Effects in SiO2 films, Phys. Rev. Lett. 30 (1973) 614–617. https://doi.org/10.1103/PhysRevLett.30.614.

[86] G. Battaglin, A. Boscoletto, G. Della Mea, G. De Marchi, P. Mazzoldi, A. Miotello, B. Tiveron, Heavy ion irradiation of glasses: Enhanced diffusion and preferential sputtering of alkali elements, Radiat. Eff. 98 (1986) 101–108. https://doi.org/10.1080/00337578608206102.

[87] X. Guo, C. Zhai, R. Kang, Z. Jin, The mechanical properties of the scratched surface for silica glass by molecular dynamics simulation, J. Non. Cryst. Solids. 420 (2015) 1–6. https://doi.org/10.1016/j.jnoncrysol.2015.04.001.

[88] M.M. Smedskjaer, J.C. Mauro, Y. Yue, Prediction of glass hardness using temperature-dependent constraint theory, Phys. Rev. Lett. 105 (2010) 10–13. https://doi.org/10.1103/PhysRevLett.105.115503.

[89] M. Wang, Y. Le Pape, N.M.A. Krishnan, M. Bauchy, G. Sant, Y. Yu, B. Wang, Irradiation-induced topological transition in SiO2: Structural signature of networks' rigidity, J. Non. Cryst. Solids. 463 (2017) 25–30. https://doi.org/10.1016/j.jnoncrysol.2017.02.017.

[90] S.M. and T.T. Shinsuke Nakano, Change in Mechanical Properties of Ion-Irradiated Ceramics Studied by Nanoindentation, Am. Nat. 106 (2006) 581–588. https://doi.org/10.2320/jinstmet.69.815.

[91] U.S. DOE: Office of Nuclear Energy, Light Water Reactor Sustainability Program: expected condition of concrete exposed to radiation at age 80 years of reactor operation, 2015. http://www.energy.gov/sites/prod/files/FY-15_LWRS_IPP_Final_0.pdf.

[92] I. Maruyama, K. Haba, O. Sato, S. Ishikawa, O. Kontani, M. Takizawa, A Numerical Model for Concrete Strength Change under Neutron and Gamma-ray Irradiation, J. Adv. Concr. Technol. (2016). https://doi.org/10.3151/jact.14.144.

[93] J. Lian, L.M. Wang, K. Sun, R.C. Ewing, In situ TEM of radiation effects in complex ceramics, Microsc. Res. Tech. (2009). https://doi.org/10.1002/jemt.20669.

[94] R.C. Ewing, W.J. Webert, F.W. Clinard, Radiation effects in nuclear waste forms for high-level radioactive waste, Prog. Nucl. Energy. 29 (1995) 63–127.

[95] J.S. McCloy, A. Goel, Glass-ceramics for nuclear-waste immobilization, MRS Bull. 42 (2017) 233–240. https://doi.org/10.1557/mrs.2017.8.

[96] A.B. Giorla, Y. Le Pape, C.F. Dunant, Computing creep-damage interactions in irradiated concrete, J. Nanomechanics Micromechanics. 7 (2017) 1–13. https://doi.org/10.1061/(ASCE)NM.2153-5477.0000118.

[97] D. Naus, H. Wiggenhauser, A. Taffe, Non-destructive Testing of Nuclear Power Plant Concrete Structures: State of the Art, 2013.

[98] E. Ohdaira, N. Masuzawa, Water content and its effect on ultrasound propagation in concrete - the possibility of NDE, Ultrasonics. 38 (2000) 546–552. https://doi.org/10.1016/S0041-624X(99)00158-4.

[99] H. Güneyli, S. Karahan, A. Güneyli, N. Yapıcı, Water content and temperature effect on ultrasonic pulse velocity of concrete, Russ. J. Nondestruct. Test. 53 (2017) 159–166. https://doi.org/10.1134/S1061830917020024.

[100] R. Demirboğa, I. Türkmen, M.B. Karakoç, Relationship between ultrasonic velocity and compressive strength for high-volume mineral-admixtured concrete, Cem. Concr. Res. 34 (2004) 2329–2336. https://doi.org/10.1016/j.cemconres.2004.04.017.

[101] J.A. Bogas, M.G. Gomes, A. Gomes, Compressive strength evaluation of structural lightweight concrete by non-destructive ultrasonic pulse velocity method, Ultrasonics. 53 (2013) 962–972. https://doi.org/10.1016/j.ultras.2012.12.012.

[102] K. Momma, F. Izumi, VESTA: A three-dimensional visualization system for electronic and structural analysis, J. Appl. Crystallogr. 41 (2008) 653. https://doi.org/10.1107/S0021889808012016.

[103] J.F. Ziegler, M.D. Ziegler, J.P. Biersack, SRIM - The stopping and range of ions in matter (2010), Nucl. Instruments Methods Phys. Res. B. 268 (2010) 1818–1823. https://doi.org/10.1016/j.nimb.2010.02.091.

[104] William Primak, Threshold for Radiation Effects in Silica, Phys. Rev. B. 6 (1972) 4846–4851. https://doi.org/10.1103/PhysRevB.6.4846.

[105] V. Heera, J. Stoemenos, R. Kögler, W. Skorupa, Amorphization and recrystallization of 6H-SiC by ion-beam irradiation, J. Appl. Phys. 77 (1995) 2999–3009. https://doi.org/10.1063/1.358649.

[106] F. Harbsmeier, J. Conrad, Generation and relief of mechanical stresses in ion irradiated SIC and Si02, Nucl. Inst. Methods Phys. Res. B. 138 (1998) 505–510.

[107] M. Boccanfuso, A. Benyagoub, K. Schwartz, M. Toulemonde, C. Trautmann, C.E.A.C. Ismra, C. Cedex, Study of ion beam induced swelling in fluorite as an inert matrix model, Prog. Nucl. Energy. 38 (2001) 271–274.

[108] A. Meftah, H. Benhacine, A. Benyagoub, J.J. Grob, M. Izerrouken, S. Kadid, N. Khalfaoui, J.P. Stoquert, M. Toulemonde, C. Trautmann, Data consistencies of swift

heavy ion induced damage creation in yttrium iron garnet analyzed by different techniques, Nucl. Instruments Methods Phys. Res. Sect. B. 366 (2016) 155–160. https://doi.org/10.1016/j.nimb.2015.10.030.

[109] W. C. Oliver, G.M. Pharr, An improved technique for determining hardness and elastic modulus using load and displacement sensing indentation experiments, J. Mater. Res. 7 (1992) 1654–1583. https://doi.org/10.1177/003591571901200704.

[110] A.B. Abell, K.L. Willis, D.A. Lange, Mercury intrusion porosimetry and image analysis of cement-based materials, J. Colloid Interface Sci. 211 (1999) 39–44. https://doi.org/10.1006/jcis.1998.5986.

[111] D. Sporea, A. Sporea, Radiation Effects in Optical Materials and Photonic Devices, in: Radiat. Eff. Mater. IntechOpen, 2016: pp. 37–67. https://doi.org/10.1016/j.colsurfa.2011.12.014.

[112] L. Cartz, F.G. Karioris, R.A. Fournelle, Heavy Ion Bombardment of Silicates and Nitrides., Radiat. Eff. 54 (1981) 57–64. https://doi.org/10.1080/00337578108207127.

[113] V. Zubov, A. Ivanov, Expansion of quartz caused by irradiation with fast neutrons, Sov. Phys. Crystallogr. 11 (1966) 372–374.

[114] A Denisov, V. Dubrovskii, V. Solovyov, Radiation resistance of mineral and polymer construction materials, 2012.

[115] S.C. Chowdhury, B.Z. (Gama. Haque, J.W. Gillespie, Molecular dynamics simulations of the structure and mechanical properties of silica glass using ReaxFF, J. Mater. Sci. 51 (2016) 10139–10159. https://doi.org/10.1007/s10853-016-0242-8.

[116] P. Heyliger, H. Ledbetter, S. Kim, Elastic constants of natural quartz, J. Acoust. Soc. Am. 114 (2003) 644–650. https://doi.org/10.1121/1.1593063.

[117] J.M. Brown, R.J. Angel, N.L. Ross, Elasticity of plagioclase fledpsars, J. Geophys. Res. Solid Earth. (2016) 663–675. https://doi.org/10.1002/2015JB012736.Received.

[118] N. Waeselmann, J.M. Brown, R.J. Angel, N. Ross, J. Zhao, W. Kaminsky, The elastic tensor of monoclinic alkali feldspars, Am. Mineral. 101 (2016) 1228–1231. https://doi.org/10.2138/am-2016-5583.

[119] Z.H. Huang, M. Gandais, R.J. Gaboriaud, Microhardness of feldspar single crystals (Or98 and An58) as a function of temperature., Bull. Mineral. 108 (1985) 835–841. https://doi.org/10.3406/bulmi.1985.7902.

[120] M.G. Jani, R.B. Bossoli, L.E. Halliburton, Further characterization of the E1′ center in crystalline SiO2, Phys. Rev. B. 27 (1983) 2285–2293. https://doi.org/10.1103/PhysRevB.27.2285.

[121] R.A. Weeks, The many varieties of E’ centers: a review, J. Non. Cryst. Solids. 179 (1994) 1–9. https://doi.org/10.1016/0022-3093(94)90680-7.

[122] S. Toyoda, The e1' center in natural quartz: Its formation and applications to dating and provenance researches, Geochronometria. 38 (2011) 242–248. https://doi.org/10.2478/s13386-011-0035-4.

[123] M. Guzzit, F. Piots, G. Spinolot, A. Veddat, C.B. Azzonit, A. Palearif, Neutron irradiation effects in quartz: optical absorption and electron paramagnetic resonance, 1992. http://iopscience.iop.org/0953-8984/4/44/025.

[124] K. Moritani, I. Takagi, H. Moriyama, Electron spin resonance measurement of irradiation defects in vitreous silica irradiated with neutrons, J. Nucl. Mater. 325 (2004) 169–173. https://doi.org/10.1016/j.jnucmat.2003.11.011.

[125] K. Moritani, Y. Teraoka, I. Takagi, H. Moriyama, Electron spin resonance measurement of irradiation defects produced in quartz crystal, Nucl. Inst. Methods Phys. Res. B. 232 (2005) 317–321. https://doi.org/10.1016/j.nimb.2005.03.065.

[126] K. Moritani, Y. Teraoka, I. Takagi, H. Moriyama, Electron spin resonance measurement of irradiation defects in vitreous silica irradiated with neutrons and ion beams, J. Nucl. Mater. 333 (2004) 988–992. https://doi.org/10.1016/j.jnucmat.2004.04.311.

[127] Y. Pan, B. Hu, Radiation-induced defects in quartz. IV. Thermal properties and implications, Phys. Chem. Miner. (2009). https://doi.org/10.1007/s00269-009-0288-0.

[128] J.M. Costantini, C. Trautmann, L. Thomé, J. Jagielski, F. Beuneu, Swift heavy ion-induced swelling and damage in yttria-stabilized zirconia, J. Appl. Phys. 101 (2007) 073501. https://doi.org/10.1063/1.2714651.

[129] W. Bolse, Amorphization and recrystallization of covalent tetrahedral networks, Nucl. Instruments Methods Phys. Res. Sect. B Beam Interact. with Mater. Atoms. 148 (1999) 83–92. https://doi.org/10.1016/S0168-583X(98)00855-6.

[130] W.J. Weber, Models and mechanisms of irradiation-induced amorphization in ceramics, Nucl. Inst. Methods Phys. Res. B. 166–167 (2000) 98–106. www.elsevier.nl/locate/nimb.

[131] C.A. Volkert, Stress and plastic flow in silicon during amorphization by ion bombardment, J. Appl. Phys. 70 (1991) 3521. https://doi.org/10.1063/1.349247.

[132] C.A. Volkert, Radiation enhanced plastic flow of covalent materials during ionirradiation, in: Mat. Res. Soc. Symp. Proc., 1992: pp. 3–14.

[133] E. Snoeks, T. Weber, A. Cacciato, A. Polman, MeV ion irradiation-induced creation and relaxation of mechanical stress in silica, J. Appl. Phys. (1995). https://doi.org/10.1063/1.359820.

[134] H. Trinkaus, Local stress relaxation in thermal spikes as a possible cause for creep and macroscopic stress relaxation of amorphous solids under irradiation, J. Nucl. Mater. 223 (1995) 196–201. https://doi.org/10.1016/0022-3115(95)00013-5.

[135] S.G. Mayr, Y. Ashkenazy, K. Albe, R.S. Averback, Mechanisms of Radiation-Induced Viscous Flow : Role of Point Defects, Phys. Rev. Lett. 90 (2003) 055505.

https://doi.org/10.1103/PhysRevLett.90.055505.

[136] M.L. Brongersma, E. Snoeks, A. Polman, Temperature dependence of MeV heavy ion irradiation-induced viscous flow in SiO2, Appl. Phys. Lett. 71 (1997) 1628–1630. https://doi.org/10.1063/1.119999.

[137] M. Hasegawa, M. Saneyasu, M. Tabata, Z. Tang, Y. Nagai, T. Chiba, Y. Ito, Positron and positronium studies of irradiation-induced defects and microvoids in vitreous metamict silica, Nucl. Inst. Methods Phys. Res. B. 167 (2000) 431–439.

[138] S. Toyoda, M. Ikeya, Thermal stabilities of paramagnetic defect and impurity centers in quartz: for ESR dating of thermal history, Geochemical Journal,. 25 (1991) 437.

[139] A. Makishima, J.D. Mackenzie, Direct calculation of Young's moidulus of glass, J. Non. Cryst. Solids. 12 (1973) 35–45. https://doi.org/10.1016/0022-3093(73)90053-7.

[140] M.M. Smedskjaer, Topological model for boroaluminosilicate glass hardness, Front. Mater. 1 (2014) 23. https://doi.org/10.3389/fmats.2014.00023.

[141] M.M. Smedskjaer, M. Bauchy, J.C. Mauro, S.J. Rzoska, M. Bockowski, Unique effects of thermal and pressure histories on glass hardness: Structural and topological origin, J. Chem. Phys. 143 (2015) 164505. https://doi.org/10.1063/1.4934540.

[142] I. Remec, T.M. Rosseel, K.G. Field, Y. Le Pape, Characterization of Radiation Fields for Assessing Concrete Degradation in Biological Shields of NPPs, EPJ Web Conf. 153 (2016) 05009. https://doi.org/10.1051/epjconf/201715305009.

[143] M.J. Norgett, M.T. Robinson, I.M. Torrens, A proposed method of calculating displacement dose rates, Nucl. Eng. Des. 33 (1975) 50–54. https://doi.org/10.1016/0029-5493(75)90035-7.

[144] J.A. Mascitti, M. Madariaga, Method for the calculation of DPA in the reactor pressure vessel of Atucha II, Sci. Technol. Nucl. Install. 2011 (2011). https://doi.org/10.1155/2011/534689.

[145] T. Yamada, H. Suzuki, T. Hanari, T. Shibata, A. Nishimura, S. Koyama, H. Daido, Y. Shimada, O.. Kotyaev, S. Kurahashi, Evaluation of concrete strength by laser induced ultrasonic waves, in: Japan At. Energy Soc. Fall 2016, 2016.

[146] D. Naus, The Effect of Elevated Temperature on Concrete Materials and Structures — A Literature, 2005. https://doi.org/10.6088/ijcser.00202010079.

[147] C. Gallé, J. Sercombe, Permeability and pore structure evolution of silico-calcareous and hematite high-strength concretes submitted to high temperatures, Mater. Struct. Constr. 34 (2001) 619–628. https://doi.org/10.1617/13695.

[148] TEPCO, Technical Strategic Plan 2017 for Decommissioning of the Fukushima Daiichi Nuclear Power Station of Tokyo Electric Power Company Holdings, Inc., (2017).

[149] J. Carette, S. Staquet, Monitoring the setting process of mortars by ultrasonic P and S-

wave transmission velocity measurement, Constr. Build. Mater. 94 (2015) 196–208. https://doi.org/10.1016/j.conbuildmat.2015.06.054.

[150] T. Shiotani, D.G. Aggelis, Wave propagation in cementitious material containing artificial distributed damage, (2009) 377–384. https://doi.org/10.1617/s11527-008-9388-4.

[151] V.M. Malhotra, N.J. Carino, Handbook on Nondestructive Testing of Concrete, 2004. http://www.crcpress.com/product/isbn/9780849314858.

[152] E. Annerel, L. Taerwe, Revealing the temperature history in concrete after fire exposure by microscopic analysis, Cem. Concr. Res. 39 (2009) 1239–1249. https://doi.org/10.1016/j.cemconres.2009.08.017.

LIST OF PUBLICATIONS AND AWARDS

Journal papers

1. **Luu Vu Nhut**, Kenta Murakami, et al., *Swelling of alpha-quartz induced by MeV ions irradiation: Critical dose and swelling mechanism*, Journal of Nuclear Materials, Vol. 539 (2020) 152266
   https://doi.org/10.1016/j.jnucmat.2020.152266
2. **Luu Vu Nhut**, Kenta Murakami, et al., *Changes in properties of alpha-quartz and feldspars under 3 MeV Si-ion irradiation*, Journal of Nuclear Materials, Vol. 545 (2021) 152734.
   https://doi.org/10.1016/j.jnucmat.2020.152734
3. **Luu Vu Nhut**, Kenta Murakami, et al., *Applicability of ultrasonic-wave based method for integrity assessment of concrete severely damaged by heat,* E-Journal of Advanced Maintenance Vol.11 No. 4 (2020) 163-171
4. Phongsakorn Prak Tom, Kenta Murakami, **Luu Vu Nhut**, *Ion irradiation-induced the radiation hardening in Fe and Fe-0.3 Si alloys*, IOP Conference Series: Materials Science and Engineering, Vol. 785,012027
   doi:10.1088/1757-899X/785/1/012027

Awards

1. 2020 Atomic Energy Society of Japan Materials Subcommittee Young Excellence Award for "*The effect of ion irradiation on amorphization and volume change in model materials of concrete aggregates*"
2. *Poster Award for "Swelling behavior of SiO2 mineral under ion irradiation"*, January 2020, 材料照射研究会－Irradiation 3.0

Presentations

1. Nhut L.V, Kenta Murakami, et al., *The effects of ion irradiation on amorphization and volume change of alpha-quartz and feldspar minerals,* October 2020, NUMAT2020 (poster)

2. Nhut L.V, Kenta Murakami, et al., *Ion irradiation-induced changes in the properties of rock-forming minerals of concrete aggregates at high fluences*, September 2020, AESJ fall meeting (*oral presentation*)

3. Nhut L.V, Kenta Murakami, et al., *In-situ Transmission Electron Microscopy on amorphization in alpha-quartz at 300K and 423K*, September 2020, JIM meeting (*oral presentation*)

4. Nhut L.V, Kenta Murakami, Hamza Samouh, Ippei Maruyama, Kiyoteru Suzuki, Hiroaki Abe, *Swelling behavior of SiO2 mineral under ion irradiation*, January 2020, 材料照射研究会－Irradiation 3.0, Japan (Poster).

5. Nhut L.V, Kenta Murakami, Ippei Maruyama, *Swelling of alpha-SiO2 induced by MeV ions irradiation: Critical dose for swelling*, The Vietnam Conference on Nuclear Science and Technology, 07nd -09th August 2019, Ha Long, Viet Nam *(oral presentation).*

6. Nhut L.V, Kenta Murakami, Do Thi-Mai-Dung, Masahide Suzuki, *Applicability of ultrasonic-wave based method for integrity assessment of concrete severely damaged by heat*, The 4th International Conference on Maintenance Science and Technology (ICMST-Tohoku 2018), Japan *(oral presentation).*

7. Nhut L.V, Do Thi-Mai-Dung, Kenta Murakami, Masahide Suzuki, *Physicochemical and mechanical characteristics of concrete exposed to high temperature*, The Vietnam Conference on Nuclear Science and Technology, 02nd -04th August 2017, Nha Trang City, Viet Nam (*oral presentation*).

8. Nhut L.V, Do Thi-Mai-Dung, Kenta Murakami, Masahide Suzuki, *The characteristics of concrete after heating to high temperatures*, 2017 AESJ Fall Meeting September 13-15, 2017 Hokkaido University, Japan (*Poster*).

9. Nhut L.V, Do Thi-Mai-Dung, Kenta Murakami, Masahide Suzuki, *Physicochemical and mechanical characteristics of concrete exposed to high temperature*: *Damage characterization*, the 6th International GIGAKU Conference in Nagaoka (IGCN 2017), 5th - 6th, October, 2017, Nagaoka, Japan (*Poster*).